Energy & Environmental Science

Accepted Manuscript

This article can be cited before page numbers have been issued, to do this please use: L. Jiang, X. Liu, J. Lv, G. Li, P. Yang, Y. Ma, H. Zou and Z. L. Wang, *Energy Environ. Sci.*, 2024, DOI: 10.1039/D4EE00482E.

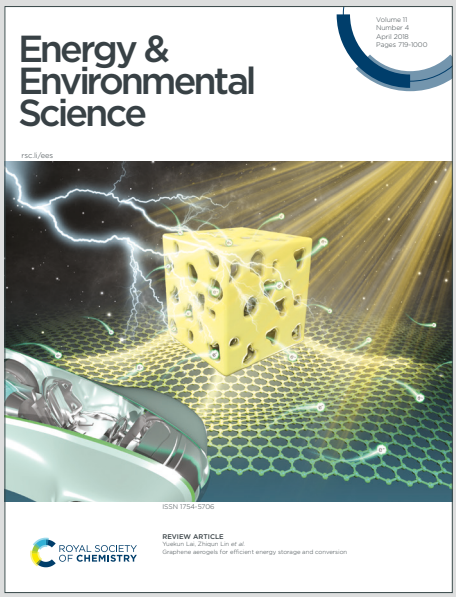

ROYAL SOCIETY OF CHEMISTRY

rsc.li/ees

View Article Online
DOI: 10.1039/D4EE00482E

Covering approximately 71% of the Earth's surface, and gases pervading the atmosphere, fluids hold immense potential for renewable energy. The conversion of fluid motion energy into electricity is pivotal, positioning it as a widely employed renewable source. Fluidic Triboelectric Nanogenerators (F-TENGs) exemplify sustainable technology, harvesting green energy by transforming fluid's inherent energy into electricity. Beyond power generation, F-TENGs offer an innovative and eco-friendly approach, potentially reshaping the renewable energy landscape. Advancing this technology aligns with broader goals of achieving sustainable energy practices in our evolving society. Our systematic exploration establishes a theoretical framework, understanding F-TENGs' capabilities and limitations, optimization strategies, design principles, and diverse applications. This positions F-TENGs as a transformative force in the renewable energy sector.

View Article Online
DOI: 10.1039/D4EE00482E

Fluid-Based Triboelectric Nanogenerators: Unveiling the Prolific Landscape of Renewable Energy Harvesting and Beyond

Lihong Jiang[1], Xinlin Liu[1], Junling Lv[1], Gaojie Li[1], Peiyuan Yang[1], Yumeng Ma[1], Haiyang Zou[1,*], Zhong Lin Wang[2,3,*]

[1]College of Materials Science and Engineering, Sichuan University, Chengdu 610065, China

[2]Beijing Institute of Nanoenergy and Nanosystems, Chinese Academy of Sciences, Beijing 100083, China.

[3]School of Nanoscience and Engineering, University of Chinese Academy of Sciences, Beijing 100049, P. R. China

* Corresponding authors. E-mail addresses: Haiyang Zou. (zhy@scu.edu.cn), Zhong Lin Wang. (zlwang@gatech.edu).

Abstract

Fluid-based triboelectric nanogenerators (F-TENGs) is a cutting-edge technology that leverages fluids as a contact medium to harness renewable energy through contact electrification (CE) and electrostatic induction. Noteworthy is its remarkable capacity to convert continuous mechanical energy into electricity from environmental sources such as natural wind, river flow, and raindrops. The review delves into the prominent characteristics of F-TENGs, providing a retrospective analysis of its developmental journey and foundational structure. It critically examines key factors influencing power generation capability and output performance, offering insights into the typical structures of F-TENGs in practical applications. The paper highlights the significant achievements of F-TENGs across diverse domains including agriculture, the Internet of Things, environment, transportation, industry, microfluidics, and life science. Furthermore, it discusses the future development directions of F-TENGs, shedding light on the current challenges it faces. This review serves as a valuable resource for researchers, engineers, and practitioners, offering a comprehensive understanding of F-TENG's capabilities, applications, and avenues for future exploration in the realm of renewable energy and self-sustained sensor technologies.

View Article Online
DOI: 10.1039/D4EE00482E

1. Introduction

On Earth, fluids, encompassing both gases and liquids, are omnipresent and extensively distributed. The continuous flow of these fluids carries inherent mechanical energy, making them abundant sources of renewable energy. Harnessing this fluid energy is pivotal for sustainable power generation, as it taps into the natural movements of the environment. Understanding and developing fluid energy harvesting technologies are essential steps toward utilizing these ubiquitous resources, offering a key pathway to address our energy needs in an eco-friendly and efficient manner. However, most types of renewable clean energy are high-entropy energy[1–3] which are widely distributed, irregular, and have various limitations, such as ocean,[3–8] wind,[9–12] hydro[13,14] and ambient mechanical energy[15–17] with those are difficult to make full use of renewable clean energy. Integrated the two physical effects of contact electrification (CE) and electrostatic induction, the groundbreaking concept of triboelectric nanogenerator (TENG) was introduced in 2012,[7,18] developing an efficient means to harness the generated electrical energy. This marked a pioneering step towards unlocking the potential of triboelectricity, which holds indispensable significance in advancing the cause of sustainable development.

Significant strides have been made in the in-depth theoretical research and extensive applications of Fluid-based TENG (F-TENG), a type of TENG that harvest mechnical energy from fluids.[5,8] F-TENG can be divided into two categories: one propelled by fluid motion, which captures the kinetic energy of the fluid and converts it into electrical energy, and the other directly utilizes fluid as the friction material, boasting versatility in harnessing wind or wave energy and reducing material wear for sustainable energy harvesting solutions. This captivating field of study seamlessly integrates the principles of fluid dynamics, nanotechnology, and electricity, aiming to harness energy from various liquids and gases. Notably, water and wind energy, which are abundantly distributed on Earth's surface, serve as key sources for F-TENG. With approximately 71% of the Earth's surface covered by water and gases pervading the atmosphere, extending outward from the surface, there exists immense potential. Consequently, the conversion of fluid motion energy into electricity positions it as one of the most pivotal and extensively employed renewable energy sources.[19–21] As research progresses in this field, advancements in the efficiency and scalability of F-TENG have been observed, further enhancing its impact on energy harvesting. The limitations in weight, size, and cost of conventional electromagnetic generators (EMGs) pose challenges in fully harnessing renewable energy sources.[22] Therefore, F-TENG have been shown as sustainable technology in green energy harvesting.[23] The importance lies not only in the generation of power but also in the innovative and eco-friendly approach it brings to the table. It's a promising avenue that could reshape the landscape of renewable energy technologies. One of the key advantages of F-TENG is its versatility. It can utilize a wide range of fluids, including water, oil, and even biological fluids, and gases as well. This adaptability makes it applicable in diverse settings, from industrial processes to biomedical applications. Imagine the potential for harvesting energy from flowing water in rivers or the movement of bodily fluids for medical devices which is a breakthrough

in energy harvesting. Understanding and advancing this technology contributes to the broader goal of achieving sustainable energy practices and addressing the growing demand for clean and efficient power sources in our evolving society.

In delving into the intricacies of F-TENG, it is imperative to elucidate the distinctive characteristics that set it apart from its solid-solid counterpart, serving as a comprehensive introduction to the nuanced facets of F-TENG. Fig. 1 visually highlights how these features interplay to enable a range of practical uses for F-TENG. The versatile features of F-TENG pave the way for diverse applications. These applications are a direct result of the five distinct features, each contributing to the technology's adaptability and functionality. The following enumeration encapsulates five salient features:

1. Energetical independence: A defining characteristic of F-TENG is its capacity to harness kinetic energy directly from the fluid medium, eliminating the necessity for external mechanical energy to facilitate contact and separation of its components. For instance, the perpetual motion of ocean waves and consistent winds across plains can propel the operation of TENG. This independence from external power sources distinguishes F-TENG as a self-sustaining entity—a trait lacking in the conventional solid-solid based TENG (S-TENG), which relies on external mechanical energy. This intrinsic quality underscores its self-sufficiency in energy generation.

2. Structural Diversity: The adaptability of F-TENG stems from the innate versatility of fluids to conform to diverse environmental conditions, facilitated by their shape adaptability. For example, within various pipelines or containers of different geometries, fluids effortlessly adjust to their surroundings, ensuring optimal contact with the pipeline walls or container surfaces. This intrinsic flexibility facilitates the design of F-TENG with a wide range of structural configurations. In open outdoor environments, abundant wind energy can be effectively harnessed through innovative techniques such as wind cups or devices that exploit flow-induced vibration. This serves as a stark contrast to the inherent limitations imposed on S-TENG, which are constrained both in terms of structural design and material adaptability.

3. Fluid properties: The inherent mechanism of S-TENG relies on mechanical interactions between solids and is susceptible to environmental changes such as humidity, climate, and external forces upon material exposure. While F-TENG can operate within a closed tube or container environment, it is not limited to such settings. In this configuration, variations in environmental conditions do not affect its output, as F-TENG derives energy directly from fluid motion. The efficacy of F-TENG hinges on intrinsic fluid properties such as pressure, flow velocity, viscosity, and ionic concentration, highlighting the crucial role of fluid dynamics in optimizing its performance.

4. Environmental extensiveness: F-TENG showcases its effectiveness across diverse environments, spanning natural landscapes like marine, river, and gas flow scenarios, as well as built environments such as greenhouses, highways, and factories. This extensive environmental adaptability positions F-TENG as a versatile tool for a wide array of applications, particularly in fields like environmental monitoring and energy harvesting, where S-TENG might encounter

View Article Online
DOI: 10.1039/D4EE00482E

limitations. Fluids inherently harbor energy from an array of sources, including wind energy, blue energy, and gravitational potential energy. This wealth of available energy sources underscores the environmental extensiveness of F-TENG, enabling it to tap into diverse energy reservoirs for sustainable power generation.

5. Mechanical durability*: When fluids are utilized as tribo-materials and/or lubricant (Note: the asterisk superscript* denotes these particular circumstances), F-TENGs exhibit remarkable resistance to mechanical wear, contrasting with the wear-prone nature of S-TENG, which experience substantial friction forces and material abrasion during operation. This resilience is crucial for ensuring prolonged and stable operation, particularly in dynamic environments characterized by continuous friction. However, it is important to emphasize that while F-TENG offer this advantage, their design must also prioritize the generation of a discernibly modest signal. Therefore, achieving a delicate balance between wear resistance and signal output is paramount in the development of efficient F-TENG systems for various applications.

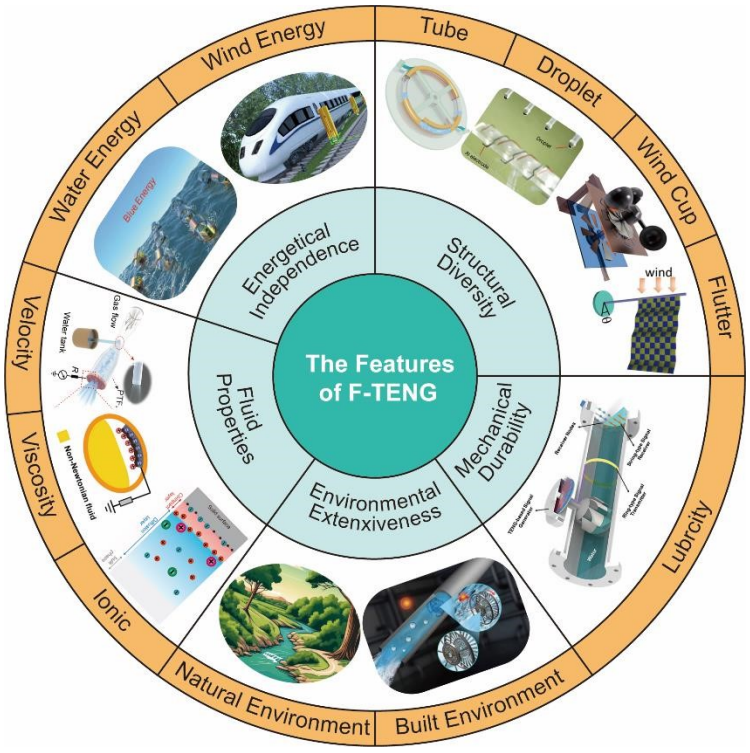

Fig. 1 Schematic overview of features, structures and applications for F-TENG.

In this review, we focus on the fluid materials as the direct tribo-layers involved in the contact electrification process and we commence with a comprehensive discussion on the developmental trajectory of F-TENG based on two primary categories-gas and liquid. The discussion unfolds to encompass recent progress in understanding the fundamental principles and operational mechanisms of contact electrification for fluid materials. Subsequently, we meticulously dissect the factors that impact the output performance of F-TENG, systematically categorizing them based on the nature of the media. A concise examination of common F-TENG structures follows, distinguishing between those utilizing liquid and gas, accompanied by a discussion of their

respective output performance, advantages, and drawbacks. Furthermore, we explore the applications of F-TENG in agriculture, the Internet of Things (IoT), transportation, environmental protection, and fluid control. Concluding the review, we provide a summary of current accomplishments in the field of F-TENG and outline prospects for future directions.

2. Fundamental theories and working modes

Contact electrification is an exceedingly prevalent phenomenon, manifesting itself in various facets of daily life. Despite the passage of 2600 years since the initial documentation of this phenomenon, its scientific mechanism has remained elusive over the course of many years, enthusiasm for studying CE has been recently renewed due to the emergence of TENGs. and quantitative characterization of triboelectric charges under various conditions.[24–26]

This section initiates with a brief overview of the fundamental principle that underlies TENG power generation for fluid materials. Building upon this foundation, we delve into the intricate mechanism propelling the power generation of F-TENG, primarily governed by interactions at liquid-solid and gas-solid interfaces. Following this, a concise exploration of the four fundamental operational modes inherent to F-TENG technology is presented.

2.1 Theory of contact-electrification of fluids

Contact electrification occurs after physical contact between materials and is the macroscopic manifestation of charge transfer.[27,28] Due to the extensive selection of materials in the categories of metals, dielectrics, glasses, ceramics, and semiconductors that exhibit a Triboelectrification (TE) effect, there is scarcely any consensus in scientific comprehension regarding the essence of TE.[29] With the development of CE-related theories, the electron-cloud-potential-well model, electric double layer, and electron transfer model have also been proposed.[25,30–34]

2.1.1 Surface state model

Contact electrification is a ubiquitous phenomenon occurring across diverse materials, posing a challenge in developing a unified explanation. The surface state model has been instrumental in elucidating CE mechanisms, especially in materials with electronic structures represented by energy bands.[27,29,35] In the context of mutual contact and CE occurring between fluid and solid, the presence of a solid surface implies periodic interruptions in the crystal lattice, resulting in the creation of energy states within the band gap. Surface defects may influence the occupancy of these states by electrons. As shown in Fig. 2a, Due to the different materials having distinct valence bands, the energy of surface states occupied by different materials also varies.[29] When these two materials come into mutual contact, driven by the energy difference of these surface states, electron transfer occurs, resulting in CE. The surface state model emphasizes that the electrostatic charges generated during the CE process are bound to surface states and may not move freely, especially in materials with low conductivity. These charges are expected to remain permanently on the surface, but thermal energy fluctuations can release bound electrons from surface states, as described by the thermal

View Article Online
DOI: 10.1039/D4EE00482E

electron emission model.[31,36,37] In summary, the surface state model provides a theoretical framework for understanding CE between fluids and solids, considering the energy band diagrams of each material. The occupation and transfer of electrons play a vital role in the generation of electrostatic charges during contact electrification.

2.1.2 Overlapped electron cloud model

Usually, the surface state model can only explain dielectrics with surface defects that can be interpreted by energy band diagrams. However, for materials whose electronic structure is represented by molecular orbitals, typically referring to polymers, rubber materials, and some natural materials without well-defined molecular structures, the surface state model becomes ineffective. In such cases, the overlapped electron cloud model is required for explanation. In the case of solids, the model suggests that when two materials make contact, their respective electron clouds overlap due to the external force applied. This overlap leads to the formation of an ionic or covalent bond between the materials, causing electrons to transfer, resulting in contact electrification.[38] The experimental observations from Kelvin Probe Force Microscopy (KPFM) by Wang *et al.*[29] studies support the concept that the gap between the tip and sample for electron transfer to take place should be less than the interatomic distance at equilibrium. Specifically, the increased overlap of local electron clouds leads to electron transfer from one material to another. This model further explains the reason for the increased transfer of charges when external force is applied to one material, causing friction with another material.

As shown in Fig. 2b, A and B represent distinct atoms from two materials, each composed of positively charged protons and neutral neutrons surrounded by a cloud of negatively charged electrons which can appear anywhere contained in the electron cloud.[27] The arrangement of electrons is closely related to the potential well that forms around the atom. After the two materials approach each other, the electron clouds overlap and begin to interact, the initial single potential well transforms into an asymmetric double-well potential[25] leading to a lowering of the barriers. An energy gradient is created, where electrons can move from higher to lower energy regions, resulting in contact electrification.

In the context of liquid-solid interactions, the model emphasizes that molecules in the liquid phase exhibit an overlap of electron clouds with atoms on the solid surface during the initial contact phase. This interaction is crucial for understanding charge transfer at the liquid-solid interface. The increased repulsive force due to electron cloud overlap plays a vital role in the context of CE, where externally applied forces contribute to generating localized high pressure at the contact point, thereby initiating the electron transfer process. Furthermore, quantum mechanical calculations support the overlapping electron cloud model, indicating that, under stress, the delocalization of the electron wave function is the primary driving force for electron transfer.[29] The model provides a comprehensive explanation of the atomic-scale charge transfer mechanism involved in contact electrification, emphasizing the crucial role of electron cloud interaction at the molecular level.

View Article Online
DOI: 10.1039/D4EE00482E

2.1.3 Electric double-layer model

The CE between liquid-solid has both electron and ion transfers.[29] Suggesting that charges may transfer between surfaces through H^+ and OH^- ions from absorbed water in the ambient atmosphere, first-principle simulations on alumina and silica surfaces corroborate the influence of adsorbed water in surface charging, where OH^- is considered a dominant charge carrier, accumulating at interfaces and contributing to observed electrification.[39–41]

With the in-depth study of liquid-solid CE, Wang's group reported the formation of an electric double layer (EDL) based on liquid-solid contact electrochemistry, then deepened to the "two-step" process in 2018.[30] The two-step model is proposed to amend the conventional mechanism of electric double-layer formation. Building upon this model, Lin *et al.*[31] discovered the coexistence of both electron and ion transfers in liquid-solid CE. Usually, ion transfer may dominate between hydrophilic materials and aqueous solution, while electron transfer may dominate between hydrophobic materials and aqueous solution. This is further supported by the study of Nie *et al.*[33], who concluded that the CE process between PTEF, and an aqueous solution is dominated by electron transfer. As shown in Fig. 2c, the water molecules and PTFE molecules are separated by an interfacial potential barrier before contacting each other due to the presence of potential energies for electrons to escape. When two molecules come into contact with each other, electrons leap from the oxygen atoms of the water molecule to the PTFE. Electrons can be retained in PTFE if their energy fluctuates below the energy barrier. When two substances are separated, a new equilibrium is established. The positively charged water molecules cause polarization of the surrounding water molecules, thus reducing the electrostatic energy generated by the separation.

Connecting these findings to the broader context of electric double layers, it is crucial to understand that an electric double layer is a phenomenon occurring at the interface between a charged surface and an electrolyte solution. An electric double layer is a phenomenon that occurs at the interface between a charged surface (usually a solid or liquid) and an adjacent electrolyte solution (a solution containing ions).[42] As shown in Fig. 2e, it can be simply divided into two steps. The first step is that when solid and liquid materials are in contact with each other, their electron clouds overlap each other due to thermal movement, and liquid pressure, electron transfer occurs on the solid surface and neutral atoms become ions. In the second step, owing to electrostatic interactions, freely moving ions in the liquid are drawn toward the charged surface, resulting in the formation of a double electric layer.

In addition to exploring the CE between solid-solid and liquid-solid, the gas–solid model remains to be exploited. Sun *et al.*[43] did part of the work to explore gas-solid CE, they hypothesize that the electrification in gas-solid contact primarily relies on electron transfer. As shown in Fig. 2d, Sun *et al.*[43] designed a single-electrode triboelectric nanogenerator with induced electrodes in a cylinder made of copper foil slightly larger than solid particles. When a charged solid traverses an induction electrode, electrons are transferred between the electrode and the ground as a result of electrostatic induction. The larger solid surface area, movement distance, and initial charge are, the

stronger the CE between gas and solid is.[43] In comparison to CE between solid-solid and solid-liquid interfaces, the fundamental theory of CE of gas materials is still scarce, and requires further in-depth exploration.

In summary, the general conclusion of CE mechanism between solid-solid CE is that the electron transfer is dominant. Electron transfer occurs at a short-range contact when the interatomic separation between two atoms/molecules/materials is compressed to a distance shorter than the typical bonding length through the action of rubbing one material against another and applying an external force to achieve close contact.[27,29] Consequently, CE is redefined as a macroscopic quantum transition phenomenon that manifests in any material, under any state, and in any application environment. This effect is universal and fundamentally distinctive. The prevalent mode of charge transfer in CE at interfaces—whether between liquid and solid, liquid and liquid, or even gas and solid—is highly likely to be electron transfer.[44]

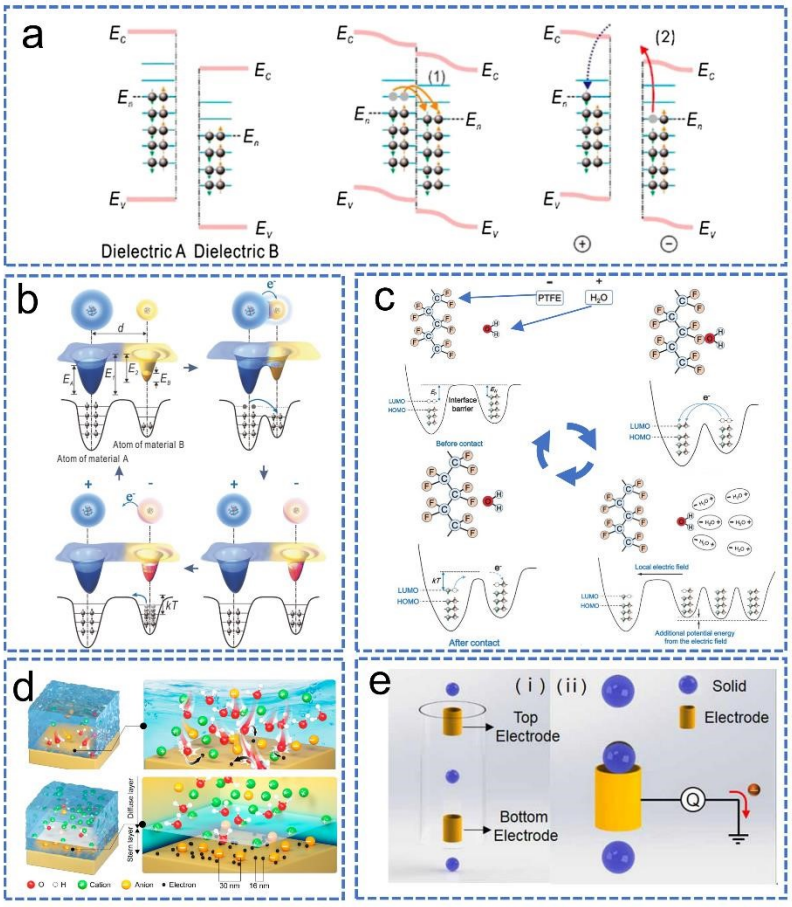

Fig. 2 Fundamentals of electrical energy generation by TENG under different contact medium conditions. (a) Schematic diagram of surface state model.[35] (b) An electron-cloud-potential well model for explaining CE and charge transfer.[25] (c) Schematic diagram of electron transfer between the water molecule and PTFE molecule.[33] (d) The testing principle of gas-solid contact electrification.[43] (e) Wang's hybrid EDL model and the "two-step" process on its formation.[30]

View Article Online
DOI: 10.1039/D4EE00482E

2.2 Basic modes of operation

The versatility of operating modes allows F-TENG to adapt effectively to various tasks related to collecting energy and sensing in fluid environments. Its multifunctionality positions it as a valuable asset in the field. Similar to the S-TENG, the F-TENG can be categorized into four basic modes based on the electrode position and the friction layer movement pattern, including contact-separation mode,[45,46] sliding mode,[47,48] single-electrode mode,[49] freestanding triboelectric-layer mode,[50] as shown in Fig. 3. However, there are some major differences in the forms as one of the tribo-layers flows through the counterpart. The details are illustrated in the following sections.

The mechanism of the liquid-TENG which employs liquid as energy source is suggested due to the dynamic electric double layer. First, besides ion adsorption, electron transfers occur at liquid-solid interface, which is a source of varying of surface charge density. Secondly, the contact area between the liquid and solid may vary due to the structure of the materials such as high porous materials. Both factors add together result in a variation in the total charge density on the solid surface once the liquid flows on the solid surface. The charges in an electrod located below the solid surface to balance the total electropotential drop results in an output current.

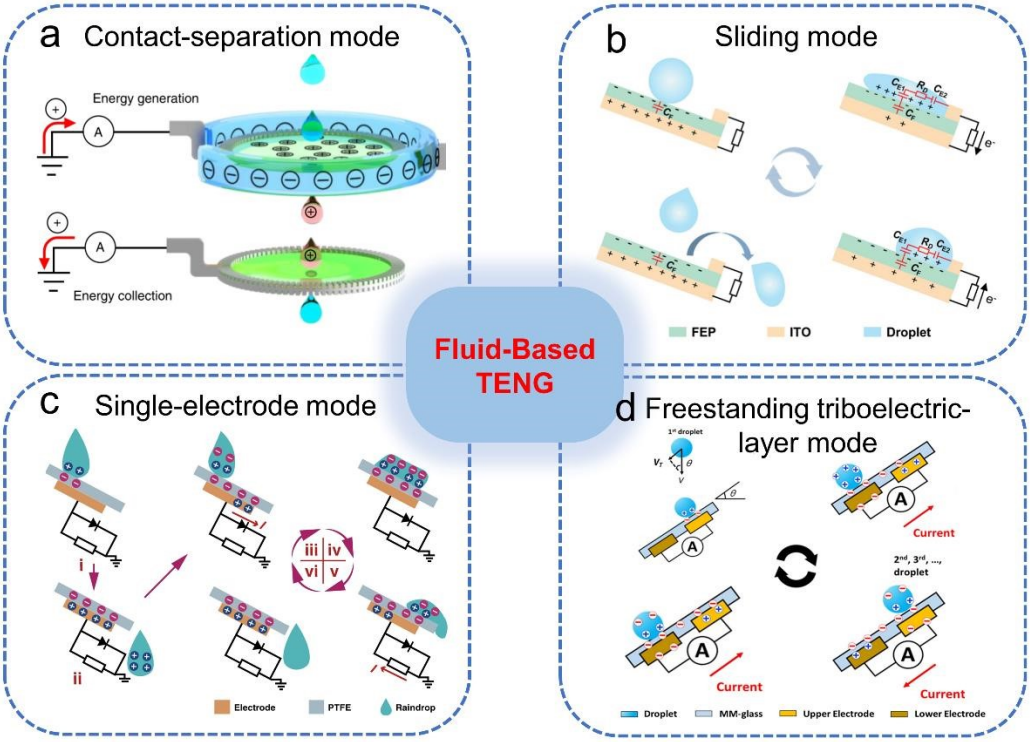

Fig. 3 Basic modes of operation of F-TENG. (a) The contact-separation mode.[46] (b) The sliding mode.[47] (c) The single-electrode mode.[49] (d) The freestanding triboelectric-layer mode.[50]

2.2.1 Contact-separation mode

The contact-separation mode is one of the most fundamental and commonly employed operational modes in TENGs. The significant characteristics of this mode include simple design,

View Article Online
DOI: 10.1039/D4EE00482E

high instantaneous power output, and ease of integration. When two distinct materials make contact and then separate, a potential difference arises between two electrodes, propelling the unrestricted movement of electrons from one electrode to the other. This process results in the generation of electrical energy. In 2013, Lin *et al.*[45] proposed the TENG based on contact electrification between water and PDMS, demonstrating the feasibility of F-TENG. Specifically, the PDMS film surface features a patterned pyramid array, acting as a stable gap between the two contact materials under no strain conditions, significantly increasing the contact area with water. Controlled by a linear motor, the PDMS film can periodically contact and separate from water, generating a maximum peak power density of nearly 0.13 W m^{-2}.

In addition to the most common solid-solid and solid-liquid contact separation, we can also consider liquid-liquid contact separation. As shown in Fig. 3a, Nie *et al.*[46] investigated an F-TENG based on the interaction of liquid droplets and liquid film. This device consists of two parts: the upper section with a charged liquid film responsible for energy generation, and the lower part with a pure grounded membrane designed for energy collection. When an uncharged water droplet comes into contact with the charged liquid film, charge redistribution occurs, leading the water droplet to carry away a certain amount of positive charge. In order to balance the potential difference, current is conducted from the ground to the liquid membrane, resulting in an electric current. When a positively charged water droplet comes into contact with a pure grounded membrane, the charge is redistributed between the droplet and the liquid membrane, and the charge needs to flow from the ground to the membrane to compensate for the charge carried by the droplet.

2.2.2 Sliding mode

Sliding mode refers to the friction between two contact surfaces under the action of an external force that causes them to slide relative to each other, and the change in the contact area leads to the separation of charges resulting in a potential difference that drives the electrons to flow in the external circuit to counteract the potential difference.[51] The basic structure of this mode of operation is not much different from the contact-separation mode, but the sliding mode is easier to package and has a high charge transfer efficiency, which makes it more widely used in scenarios that require large-scale applications.[27,52] Lee *et al.*[48] examined the impact of micro/nano roughness on water-solid contact charging by developing a sliding water-driven TENG. This TENG utilizes an aluminum plate subjected to anodization and fluorination as the dielectric and friction layers. By repeatedly immersing it into water at a frequency of 2 Hz and a soaking depth of 1 cm, the device can achieve a maximum instantaneous peak output of 38.32 mW m^{-2}. Experimental findings indicate that surfaces with low roughness exhibited approximately 14 times higher output current and 9 times higher output voltage compared to those with high roughness. Ye *et al.*[47] proposed a highly transparent, large-area, and high-efficiency raindrop-TENG based on sliding mode, as shown in Fig. 3b, which can efficiently harvest irregular raindrop energy and provide important applications for smart agriculture and weather monitoring. The raindrop-TENG utilizes a FEP film with hydrophobicity and strong electronegativity as the electrification layer on both the surface and back, and deposits ITO electrodes to enhance the output. By systematically optimizing the array

structure of the raindrop-TENG, it effectively prevents signal cancellation caused by overlapping raindrops, resulting in an impressive average power density of up to 40.80 mW m^{-2}.

2.2.3 Single-electrode mode

In the single-electrode mode, only one electrode is connected to the electric starting surface of the TENG, and the other electrode is used as a reference electrode (eg. ground) for the electric potential. As shown in Fig. 3c, Xu *et al.*[49] reported a raindrop-TENG array for harvesting raindrop energy, which can be used as a raindrop energy harvester and a rainfall sensor at the same time, a typical single-electrode mode. The copper electrode array was fabricated using printed circuit board (PCB) technology, and a highly hydrophobic PTFE was attached to the copper electrodes to ensure the smooth rolling of droplets. Under a rainfall intensity of 71 mm min^{-1}, the raindrop-TENG was capable of providing an average short-circuit current of 15 μA, an open-circuit voltage of 1800 V, and a maximum output power of 325 μW. Besides, Wang *et al.*[53] reported a flexible TENG for human motion detection and collection of human kinetic energy, the basic principle lies in the flow-induced vibration of fluid, which can also be regarded as a single electrode mode. Due to its excellent mechanical deformability and biocompatibility, the PVA-based film is prone to electron loss, making it suitable to be used as tribo-layers in conjunction with FEP, which has a stronger electron affinity. Leveraging the characteristics of flow-induced vibration, an output voltage of 7 V can be achieved at a wind speed of 8 m s^{-1}.

The single-electrode TENGs can be connected to any position, and the flexibility of this structural construction is also an advantage of its characteristics. The efficiency of the single-electrode TENGs, however, is lower than that of the TENGs with two electrodes as it used the reference electrode rather than the potential of the other tribo-layer.

2.2.4 Freestanding triboelectric-layer mode

The freestanding triboelectric-layer mode is distinguished by both high efficiency and a high level of wear. The main principle is that the independent movement of the friction layer in the two electrodes to move between the potential changes periodically, driving the flow of electrons at both ends of the electrode to generate electrical energy. Generally, freestanding triboelectric-layer mode can be categorized according to the structure into sliding, contact, disc, and grid structure. Among them, the disc type and sliding type exhibit elevated energy conversion efficiency along with material loss rates. Effectively mitigating material wear is a key focus for enhancing TENGs performance. With its mechanical durability, F-TENG effectively mitigates abrasion, addressing the limitations inherent in the freestanding triboelectric-layer mode. As shown in Fig. 3d, Yoo *et al.*[50] reported a TENG that mimics the eyes of moths (MM-TENG) and collects both solar and raindrop energy. Unlike other TENGs that collect raindrop energy, the two electrodes of the MM-TENG are positioned beneath the MM-glass (moth's eye-mimicking quartz glass) serving as the friction layer. This configuration allows for the complete and efficient harvesting of the kinetic energy generated by falling raindrops and can be regarded as a typical freestanding triboelectric-layer mode. Overall, This model possesses the benefits of extracting energy from an in-motion entity, while maintaining

View Article Online
DOI: 10.1039/D4EE00482E

the entirety of the system in a state of mobility without the need for grounding.

3. Typical structures of F-TENG

The absence of specific shapes in fluids presents a considerable challenge, complicating the establishment of discontinuous contact between materials and making it difficult to capture the output. The intricacies in designing structures for F-TENG arise from the amorphous nature of fluids, where factors like device geometry, flow paths, and electrode positioning exert significant influence on the transfer of charges between the fluid and solid materials. Consequently, the design of structures for energy harvesting and sensing becomes intricate. Despite these challenges, fluids exhibit distinctive characteristics such as adaptability, inherent energy, and favorable interface flow with minimal friction. Continuous design innovations and structural optimizations have paved the way for the development of highly efficient TENG devices. Four fundamental operating modes exist for F-TENG, and through ongoing design enhancements and structural optimizations, achieving highly efficient TENG devices is feasible.[25,27]

To comprehensively address the structural considerations, we categorize them based on the distinct contact media and mechanisms associated with liquid-TENG and gas-TENG in this section. In general, three primary structures have been developed for liquid-TENG (droplet, wave, and flow), and three for gas-TENG (rotation, vibration, and press). Table 1 summarizes F-TENG studies reported thus far, based on the aforementioned structures.

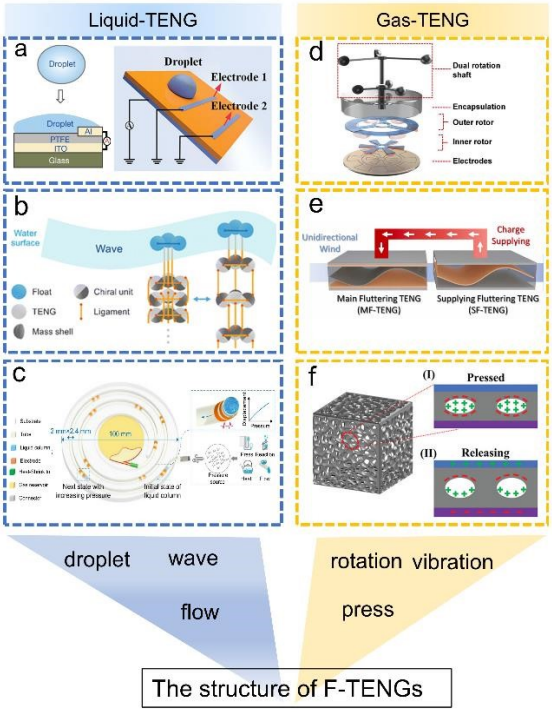

Fig. 4 The structures of F-TENGs. The F-TENGs based on (a) droplet,[54,55] (b) wave,[56] (c) flow,[57] (d) rotation,[58] (e) vibration,[59] (f) press.[60]

Table 1 A list of the performance and characteristics comparison of F-TENGs based on various working structures.

Structures	Triboelectric material	Working modes	Output performance	Characteristics	Ref.
Droplet	Water/PTFE	Single electrode	34.04 V, 5.87 μA	Corrosion resistance, water friction	54
			143.5 V, 270 μA	High performance, water friction	55
Wave	PTFE/Al	Freestanding	7.88 mW (peak power)	Widely distribute, wave-driven	56
	PTFE/Nylon	Contact separation	381 mW (peak power)	High efficiency, wave-driven	61
Flow	Water/PTFE	Single electrode	3.43 V	Pressure sensor, high accuracy, water friction	57
	Gas-liquid two-phase flow/PTFE	Single electrode	344 V, 24 μA	High performance, fast response time, water/gas friction	62
Rotation	FEP/Cu	Freestanding	306V, 32 μA	Dual-rotation shaft, preferable aerodynamics, wind-driven	58
	FEP/rabbit fur	Freestanding	87.5V, 2.57 μA	Hot wind, tunable contact areas, wind-driven	63
Vibration	Polystyrene and graphene oxide/Al	Contact separation	39 mW m^{-2} (average power density)	Low wind speed, wind-driven	64
	Polyimide/Ni/Cu fabric sheet	Contact separation	38.16 mW (peak power)	Charge excitation, wind driven	59
Press	Air/aerogel	Contact separation	98.4 V, 2.89 μA	Gas–solid coupling energy	60
	Air/elastomer	Contact separation	50 nA cm^{-2} (current density)	Gas–solid coupling energy	65

3.1 Droplet

As depicted in Fig. 4a, Xu *et al.*[55] have developed a structure capable of harnessing energy from falling water droplets. This design transcends the constraints of interfacial effects, emphasizing bulk effects and substantially boosting the instantaneous power density by several orders of magnitude. When four 100 μL droplets are released from a height of 15 cm and make contact with the PTFE surface, it instantaneously illuminates 400 commercial light-emitting diodes (LEDs). The

View Article Online
DOI: 10.1039/D4EE00482E

output voltage and open-circuit current of a single droplet-based electricity generator (DEG) are 143.5 V and 270 μA, respectively. The optimization of this structure involves the addition of an Al electrode to the PTFE surface, effectively forming a switch model within the circuit. When there is no contact between the droplet and the Al electrode, the equivalent circuit is open, resulting in no current flow. A capacitor is established at the water-aluminum interface, completing the circuit and generating current, solely when the droplet makes contact with the Al electrode. To address the vulnerability of exposed electrodes to corrosion by water, Yang *et al.*[54] introduced an electrode-grounded droplet-based electricity generator (EG-DEG) based on graphene sheet-embedded carbo electrodes. This innovative structure modifies the material of the surface-exposed electrodes, imparting them with low surface energy, high surface roughness, and excellent hydrophobic properties, and is capable of generating an average current and voltage of 5.87 μA and 34.04 V.

Due to contact and friction with air, raindrops usually carry some static charge. Wang *et al.*[66] proposed using the acoustic levitation method to suspend droplets in different gases. The droplets rotate at very high speeds within the sound waves, maintaining stable friction, resulting in a gradual accumulation of charge on the suspended droplets until saturation, followed by discharging the charge through the bottom Faraday cup. The experiment demonstrated that the suspended DI water droplet carries a positive charge after friction with air. Additionally, different suspended particles in deionized water droplets (PTFE, $BaTiO_3$, nylon) can increase the amount of charge transfer, while an ionic solution (NaCl solution, 0.1 mol/L) has an inhibitory effect on charge transfer due to the screen effect.

Traditional liquid-liquid interfaces have relatively high viscosity, making it difficult for liquids to achieve effective contact and separation. Lu *et al.*[67] utilized liquid–liquid phase separation control technology, gradually adding dextran (DEX) in batches to a polyethylene glycol (PEG) solution. After standing, distinct layering occurred, successfully creating a recoverable immiscible aqueous–aqueous interface (IAAI), which facilitated the droplet-droplet CE process, and established a liquid-liquid TENG. The significant advantage of liquid-liquid TENG is its ability to achieve a full interface for charge transfer. Charge transfer in solid-solid and solid-liquid interfaces occurs only at protrusions with uneven surfaces, where only a small portion of the interface area is close enough to facilitate charge transfer.[68] Liquid-liquid interface CE achieves thorough contact and separation, making it suitable for powering small smart devices and implantable electronic devices.

This F-TENG, designed to collect droplet energy by coupling triboelectrification and electrostatic induction effects, undergoes a gradual transition in electrode structure from a single-electrode design to an optimized structure with surface-attached metal electrodes. In comparison to the single-electrode structure, the design with surface electrodes exhibits significantly higher output voltage, current, and power. This is attributed to the success of the surface electrode structure in breaking the traditional limitations of TENG in collecting energy at friction interfaces, transforming the energy conversion from interfacial effects to bulk effects. This enables a more efficient conversion of the kinetic and potential energy of droplets falling from a height into electrical energy. However, frequent contact between the upper surface's metal electrodes and droplets can lead to

electrode corrosion, causing losses in energy conversion. Developing a new corrosion-resistant conductive material[54] for the surface electrodes to enhance device lifespan or designing an alternative structure to enhance bulk effects may be avenues to advance F-TENG technology.

3.2 Wave

Wave energy is a renewable energy that can be generated at any time in the ocean.[4,69,70] In order to better convert wave energy into electrical energy, as shown in Fig. 4b, Li *et al.*[56] have introduced an innovative three-dimensional chiral network of triboelectric nanogenerators designed to effectively harvest energy from water wave motion. This 3D TENG network demonstrates remarkable characteristics, including network flexibility, hyper-elasticity in aquatic environments, and the capability to absorb wave energy, resembling mechanical chiral metamaterials. The maximum peak power and average power output reached 7.88 mW and 2.18 mW, respectively. Besides, Gonçalves *et al.*[61] consciously regulate the movement speed of the body to collect specific characteristics of wave energy. To better collect wave energy, a unidirectional-lateral triboelectric nanogenerator (UL-TENG) specifically designed for capturing energy during the pitching rotation of buoys is employed. UL-TENG consists of a linear track fixed on the buoy, a metal sphere freely moving on the track, and a small TENG with a contact-separation model on both sides of the track. When there are waves, the track tilts, the small ball rolls along one side of the track, collides with the TENG, and converts wave energy into electricity. In addition to the oscillating structure with the waves, Zhang *et al.*[71] introduced a self-adjusting rotational TENG featuring a compound pendulum and a specialized gear mechanism designed for harnessing wave energy. In contrast to previous structures employing one-way swinging, this system, utilizing the engineered gear set, captures kinetic energy from the pendulum's two-way swinging, thereby improving the effectiveness of wave energy harvesting. When subjected to the driving force of low-frequency waves, the average mass power density can achieve 45.18 mW kg^{-1}.

Overall, F-TENG used for wave energy harvesting generally adopt structures resembling the up-and-down motion of a buoy in waves to convert mechanical energy into electrical energy. To enhance output power, perhaps combining EMG and novel methods for converting wave energy could improve efficiency.

3.3 Flow

Flow-driven systems harness the kinetic energy of fluids to generate power or propel F-TENG, whether in the form of liquids coursing through pipelines or the motion of water in rivers and oceans. In the dynamic environment of the ocean, vortex-induced vibration and wake-induced vibrations are commonly utilized by F-TENGs to collect the kinetic energy of fluids.[72] Moreover, within pipelines, the flow of liquid can induce charge transfer to generate current via the induction electrification processes. Thus, the kinetic energy generated by gravity or pump action can be harnessed through triboelectric nanogenerators.[73–75] Illustrated in Fig. 4c, Zhan *et al.*[57] proposed a liquid-piston-based pressure sensor and investigated its output performance with different electrode array configurations. By designating the electrode connected to the positive terminal of the

View Article Online
DOI: 10.1039/D4EE00482E

measuring device as "positive" (P) and the one connected to the negative terminal as "negative" (N), it was observed that using a PNP+NPN electrode array yielded the most stable output voltage. The maximum and minimum voltages recorded were 1.58 V and -0.78 V, respectively, allowing for precise determination of the direction and displacement of the liquid column's movement. Dong *et al.*[62] developed a circular single-electrode triboelectric nanogenerator (RSE-TENG) intended for both energy harvesting and parameter monitoring within gas-liquid two-phase flow. Controlling the flow rates of liquid and high-pressure gas using a peristaltic pump to regulate the gas-liquid two-phase flow within the pipeline. The pipeline is constructed with PTFE, and a conductive copper strip is wound around the outside of the polytetrafluoroethylene tube as the electrode. When the gas-liquid two-phase flow passes through the PTFE tube section with the conductive copper strip, an electric double layer forms at the interface. Due to contact electrification and electrostatic induction, water loses electrons, acquiring a positive charge, while the PTFE surface gains electrons, carrying a negative charge. The output of this structure depends positively on the solid-liquid CE area and the relative separation speed, being directly proportional to them. Focusing on an individual device, the maximum peak short-circuit output current and the maximum peak open-circuit output voltage can reach 344 V and 24 μA, respectively, significantly higher than the structure controlling the water column. To enhance the output of this flow in pipe structure, considerations can be directed towards liquid flow rate, pipe/liquid material, and liquid ion concentration, among other factors.

3.4 Rotation

Wind energy is a prevalent form of mechanical energy found abundantly in the natural world. Efficiently harnessing wind energy holds significant promise and practical importance, as it can contribute to mitigating greenhouse gas emissions, reducing energy expenses, and mitigating energy crises.[76] This potential has far-reaching implications and practical significance. As depicted in Fig. 4d, Yong *et al.*[58] have introduced a dual-rotation shaft triboelectric nanogenerator capable of efficiently harnessing wind energy over a broad range of wind speeds. This design incorporates two distinct wind cup structures with varying arm lengths and dimensions that can function independently. Each wind cup has an independent rotating axis and contacts a different TENG. Choosing FEP film with strong triboelectric capabilities as the triboelectric surface and copper as both the electrode and another triboelectric surface. The overall structure belongs to the freestanding triboelectric-layer mode, demonstrating excellent output performance. By optimizing structural parameters such as arm lengths, radii, and pole pairs, a maximum open-circuit voltage of 306V and a maximum short-circuit current of 32 μA can be obtained. For the rotation structure of TENGs, wind cups[77] or windmills[78] are commonly employed to collect wind energy, converting it into mechanical energy that rotates the disc. To enhance the output performance of the rotation structure, on one hand, improving the structure for better conversion of wind energy, and on the other hand, adopting methods such as ion injection[79,80] and charge excitation[81] to enhance the output of the rotating disc.[82] Additionally, lubricants,[83] soft contact[84] and non-contact[85] can be used to increase durability.

View Article Online
DOI: 10.1039/D4EE00482E

3.5 Vibration

In the field of engineering, flow-induced vibration is an aspect that is typically sought to be avoided as it can lead to wear and diminished performance. However, in the realm of TENGs, this characteristic can be effectively harnessed to maximize contact electrification possibilities.[86] Typically, vibration structures can be categorized into four types: vortex-induced vibrations (VIV), galloping, flutter, and wake-induced vibrations (WIV).[87] Among them, VIV refers to vibrations formed by vortices in the fluid. When fluid flows past a structure, vortices form around the structure, resulting in structural vibrations, typically observed in applications such as pipelines, bridges, and marine structures. Galloping is a low-frequency, large-amplitude vibration that typically occurs when a structure is exposed to wind or fluid flow at a certain angle, resulting in an asymmetric pressure distribution and causing periodic oscillation. Galloping is commonly observed in scenarios such as tall buildings, bridges, and power transmission lines. Flutter refers to self-excited oscillations of structures in fluid flow, typically occurring when a structure is subjected to aerodynamic or hydrodynamic forces, resulting in unstable vibrations, commonly observed in high-altitude aircraft and taller bridges. WIV refers to vibrations caused by the interaction between a structure and the wake of another object in fluid flow. This characteristic makes it common in scenarios such as ships, offshore platforms, and underwater pipelines. It is noteworthy that VIV and WIV typically occur in F-TENGs designed to collect mechanical energy from water flow, while flutter and galloping are often designed to collect mechanical energy from gas flow in F-TENGs.

In F-TENG design, flutter structures based on self-excited oscillations are more common. As illustrated in Fig. 4e, Chung *et al.*[59] have introduced a wind-based multi-utilization F-TENG, consisting of two flutter-TENG units, which can recover previously wasted wind energy for the purpose of enhancing the performance of the main flutter-TENG. This structure consists of three parts: aluminum electrodes covered with polyimide film at the top and bottom, an acrylic board framework, and a Ni/Cu-plated conductive sheet with a PVC-wrapped wire flagpole placed between the electrodes. When the airflow passes through the flutter-TENG, the conductive sheet continuously makes contact and separation with the polyimide film at the top and bottom, inducing corresponding charges on the electrodes. At a wind speed of 6 m s^{-1}, this configuration achieves a peak output power of 38.16 mW. Similarly, Son *et al.*[88] proposed a flutter-TENG with an ambient air ionizing channel (AAIC). When linked to the electrodes, it efficiently segregates the opposing charges of the flutter-TENG, resulting in the accumulation of positive and negative charges at both ends of the AAIC. This potential difference establishes an ionization channel, amplifying the output efficiency of the flutter-TENG through electrostatic discharge, leading to a high current output of up to 4 A and a root mean square (RMS) power density of up to 42.5 mW cm^{-2}. Despite the simplicity and high flexibility of flutter-TENG design, compared to rotation structures, flutter structures exhibit lower stability and efficiency, limiting them to drive only simple electronic devices. To enhance vibration structures, researchers can explore more durable and efficient materials to further improve flexibility and lifespan. Equally important is the integration of F-TENG with gas energy harvesting systems to enhance the overall system's energy conversion efficiency

View Article Online
DOI: 10.1039/D4EE00482E

and reliability, as well as standardization and normalization of key performance parameters.

3.6 Press

In addition to harvesting the continuous natural wind energy in the environment, another branch of gas-TENG involves converting the mechanical energy of a compressed elastic porous structure into electricity through the gas-solid interface CE process.[65] Huang *et al.*[60] have developed a compressible ultralight and elastic aerogel for gas-solid contact electrification. As illustrated in Fig. 4f, when this aerogel is compressed, the inner surface comes into contact with the air within its pores, leading to the transfer of charges from the air to the aerogel, resulting in the accumulation of positive and negative charges within the aerogel and air pores. Upon the aerogel's deformation recovery, the potential difference drives the flow of electric current from the top electrode to the bottom electrode, converting the cyclically compressed mechanical energy into electrical energy. Under a linear motor frequency of 1 Hz and a velocity of 2 m s^{-1}, the maximum output voltage and current can reach 98.4 V and 2.89 μA, respectively. Currently, the majority of gas-TENG structures focus on harnessing wind as a power source, with only a limited portion dedicated to researching gas-solid contact electrification. Currently, the press-TENG is still immature, with limited corresponding research. In-depth research is still required in porous structure design, material selection, and even the triboelectric principle. Unlike structures dominated by other solid materials, perhaps what has a greater impact on the output performance of press-TENG is the choice of gas and the magnitude of the gas pressure. In conclusion, the press-TENG structure still requires more mature and systematic design.

4. Factors affecting the efficiency of F-TENG

Focusing on advancing the large-scale application and industrialization of TENG, efforts have been directed towards augmenting its working power. Typical strategies involve increasing the surface charge density of materials,[89] enhancing the vacuum, and refining the structure to enhance power output.[90] The selection of materials plays a crucial role in TENG performance. Theoretical analysis reveals that the surface charge density of materials is closely linked to intrinsic properties such as electronegativity, work function, permittivity, and surface morphology. Substantial efforts in material optimization are still needed to enhance TENG performance. Operating the TENG in a higher vacuum is an effective means of augmenting the surface charge density to its maximum potential, as there is an inherent limit to the surface charge density due to the presence of air breakdown.

4.1 Factors influencing liquid materials based TENGs

In the realm of solid materials, CE manifests as a surface phenomenon at the interface of two materials, intricately influenced by factors like humidity, surface roughness, temperature, and applied force or strain. The interplay of these complexities is crucial for the manifestation of the phenomenon. The enclosed nature of liquid materials in containers and tubes makes F-TENG less susceptible to external disturbances (eg. temperature, humidity, etc.), establishing a stronger

View Article Online
DOI: 10.1039/D4EE00482E

correlation with internal factors.

To delve into methods for improving the operational efficiency of F-TENG, the subsequent section systematically categorizes influencing factors, specifically in the context of liquid TENG, encompassing environmental aspects, fluid properties, friction materials, and geometric optimization. The following list outlines these factors that play a crucial role in influencing the performance of F-TENG.

4.1.1 Environmental factors

The CE process at the liquid-solid interface, a critical mechanism in F-TENG, is influenced by environmental factors such as substrate and environmental temperature, pH, and light intensity. In Fig. 5a, Chen *et al.*[91] presented a dielectric elastomer generator (DEG) based on patterned superhydrophobic fluorine-doped graphene, overcome the problems that TENGs show significantly compromised performance in a humid environment. Their findings indicate that the DEG, relying on a superhydrophobic dielectric layer, where charge induction and transfer are less affected by environmental temperature and humidity (as illustrated in Fig. 5b and c), can maintain high output voltage and current even in high humidity conditions.

However, considerable variations in output voltage and current are evident under different pH values (as illustrated in Fig. 5d). This phenomenon may be attributed to the concentration of negative ions in the water,[92] specifically the hydroxyl ion concentration.[91] In a specific concentration range, the density of negative ions captured by DEG increases with increasing pH because of the higher hydroxyl ion concentration in alkaline environments compared to acidic ones. When the pH exceeds 9, the output current and voltage start to decrease because of the hindrance of positive charges by an excess of negative ions on the droplet surface.

Ma *et al.*[93] observed that increasing temperature has a negative impact and the extreme acidity or alkalinity has a positive impact on the overall output. A self-powered multiphase flow sensor was proposed that accurately reflects the wetting state inside a pipeline, capable of distinguishing between static water and air phases. As depicted in Figure 5e, the experimental setup consists of a vertical linear motor, needle-type receiver, and plate-type transmitter immersed in water. Through the periodic movement of the motor, the receiver alternately contacts water and ambient air, and the collected signals are analyzed using an electrometer to assess performance under different environmental conditions. Under alternating wetting at a immersion frequency of 2 Hz, the received signals for different temperatures (25–80 °C) and pH values (2–12) are illustrated in Figure 5f and g.

For a more in-depth understanding of the impact of environmental factors on F-TENG, it is essential to thoroughly examine the CE mechanism on liquid-solid surfaces. Fig. 5h illustrates the CE process between the oil droplet and the TENG.[94] The TENG is constructed using a Kapton film surface coated with fluorinated SiO_2, imparting oil-repellent properties to ensure the smooth descent of oil droplets. As shown in Fig. 5i and j, researchers conducted thermally stimulated discharge

View Article Online
DOI: 10.1039/D4EE00482E

experiments to measure the surface potential and the decay of surface potential during the sliding process of the oil droplet. The surface potential gradually decreases as the temperature rises from room temperature to 423 K, and at 423 K, the potential decay is at its fastest. This phenomenon is observed on both oil droplets and the tribo-electrification surface. The rapid decrease in surface potential with an increase in the substrate temperature is attributed to the fact that oil droplets contain only electrons, and the decay of surface charge is primarily caused by thermionic emission, which is proportional to the substrate temperature.

Additionally, the surface charge density also decreases with increasing temperature for SiO_2 surfaces (substrate temperatures), but notably, a minimum value or sticky charges persists (as shown in Fig. 5k). This phenomenon arises from the presence of ions and electrons in water molecules, where electrons can gain more energy at higher temperatures, leading to faster electron density decay and lower surface charge density. After cyclic tests of charging and heating water droplets with SiO_2 surfaces as shown in Fig. 5i and m, it becomes evident that the sticky charge density reaches a stable value. This phenomenon can be elucidated by the double electron layer.[30,31] With an increasing number of cycles, electrons are continually emitted due to thermal motion, and fewer positions on the SiO_2 surface are available for electron movement. This discrepancy arises from the presence of ions and electrons in water molecules, where electrons can gain more energy at higher temperatures, leading to faster electron density decay and lower surface charge density. While only O^{2-} ions are accumulated on the surface, forming the so-called sticky charges. These experiments substantiate the notion that both electron transfer and ion transfer play roles in liquid-solid CE.[31]

View Article Online
DOI: 10.1039/D4EE00482E

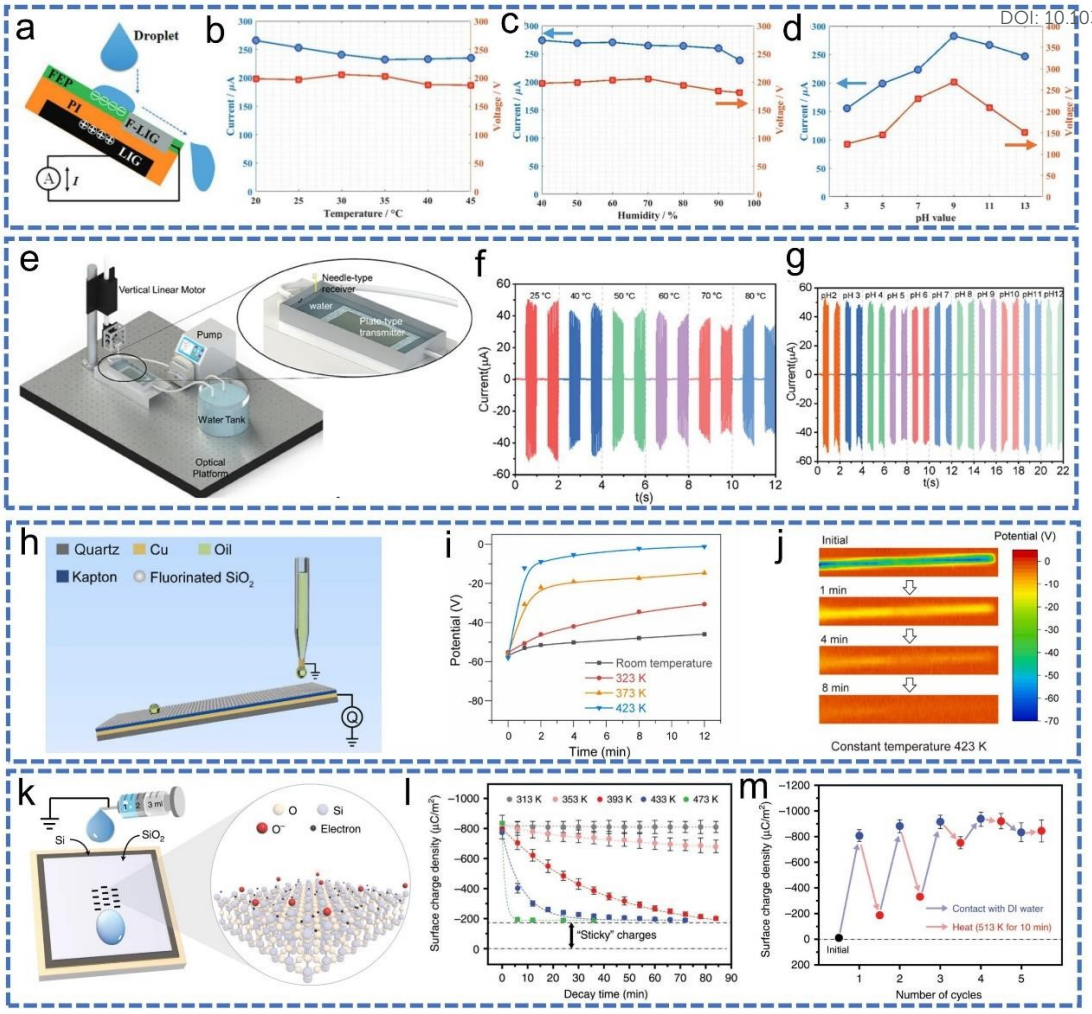

Fig. 5 Influence of the surrounding environment. (a) Droplet-based electricity generator with a laser-induced graphene-coated surface. (b to d) Effects of environmental temperature, humidity and pH on a droplet-based electricity generator.[91] (e) Experimental setup designed to simulate alternating wetting states between air and water.[93] The typical signals measured during alternating wetting periods at different temperatures (f) and pH levels (g). (h) Schematic diagram of the electrification experiments between glycerol oil droplet and solid oleophobic surface.[94] (i and j) Effect of substrate temperature and potential decay images of the motion trace with isothermal heating at 423 K. (k) The structure for the charging experiments involved the production of negative charges on the SiO_2 surface, potentially comprising electrons and O^- ions generated through surface ionization reactions.[31] (l and m) Effect of substrate temperature on the CE process between deionized water and SiO_2.

4.1.2 Liquid properties

Functioning as a fluid-driven triboelectric nanogenerator, it harnesses energy from the fluid's movement, intricately linked to ionic concentration, flow velocity, and viscosity.[95,96] Vu *et al.*[97] fabricated a poly(vinylidene fluoride-co-hexafluoropropylene) (PVDF-HFP) and ionic liquid (PIL) membrane. They subsequently formed PIL-TENG by placing this membrane in contact with water

and investigated its output performance at various concentrations of ionic liquid. Fig. 6a depicts the principle that PIL-TENG forms the EDL model at the liquid-solid contact interface. In this model, the EDL model is divided into a compact layer and a diffuse layer. The former is composed of ions adsorbed on the PIL membrane owing to chemical interactions, while the latter consists of ions attracted to surface charges based on thermal motion and electric attraction. Based on the EDL mechanism and the transfer of water flow, PIL-TENG can generate alternating current output from unsteady flows. In Fig. 6b, the impact of ionic liquid concentration on PIL-TENG output characteristics is investigated. As the ionic liquid concentration increases from 2.5 wt.% to 10 wt.%, the output current gradually rises to a maximum of 2.08 μA. However, with a further increase in ionic liquid concentration to 15 wt.%, the output performance of PIL-TENG begins to significantly decline. Zhang *et al.*[95] also conducted a study on the CE of the liquid-solid interface, reaching a similar conclusion regarding the impact of ionic concentration: as the ionic concentration increases, the CE at the solid-liquid interface peaks and then starts to decrease.

In specific ranges, the output power of the F-TENG is directly proportional to the flow rate of the liquid. Kim *et al.*[98] proposed a TENG aimed at improving the sustainability of nanogenerators. This TENG generates DC output through water electrification based on phase control. As illustrated in Fig. 6c, half of the disk was intruded into the water. While the disk rotated, the fluid velocity varied with the speed of rotation. The fluid was drawn out of the liquid pool to form a liquid film, the thickness and height of which were determined by the equilibrium among the centrifugal force produced by the rotation, the viscous force of the fluid, mass, and density (gravity force).[99] The liquid film formed by the rotation of the disk is proportional to the height of the liquid film below the speed of 200 rpm and remains stable above 200 rpm, as illustrated in Fig. 6c. This can be attributed to the fact that at 200 rpm, the liquid film has covered the entire surface of the disk, and the thickness of the water has reached the convergence value. Consequently, the output performance of this TENG demonstrates a tendency to be proportional to the rotational speed up to 200 rpm and essentially constant above 200 rpm, as depicted in Fig. 6d.

Moreover, research on the effect of viscosity on the output power of TENG is also important. In Fig. 6e, Kim *et al.*[100] reported a non-Newtonian fluid-based triboelectric nanogenerator (NNFT), in which the non-Newtonian fluid (NNF) was synchronized by cornstarch and DI water in the composition of 6:4, and the robustness increased with the application of external force on NNF.[101] In general, the shear thickening phenomenon (STP) does not occur when the shear rate does not exceed the critical shear rate. If STP occurs, the viscosity will increase dramatically. Displayed in Fig. 6f and g, as the shear rate increased, different degrees of STP were observed in different mass fractions of the corn solution, and agglomeration of the corn starch also occurred, resulting in an increase in the viscosity of the mixture. With the increase in viscosity, the output current and voltage of the NNFT gradually increase. This is explained by the fact that full contact between the electrode surface and NNF easily occurs, whereas STP takes place in the area where the external force is applied, and NNF increases the effective contact area when an external force is applied to the TENG. The arrows with orange in Fig. 6h and i clearly indicate the increase in electrical outputs caused by

NNFT.

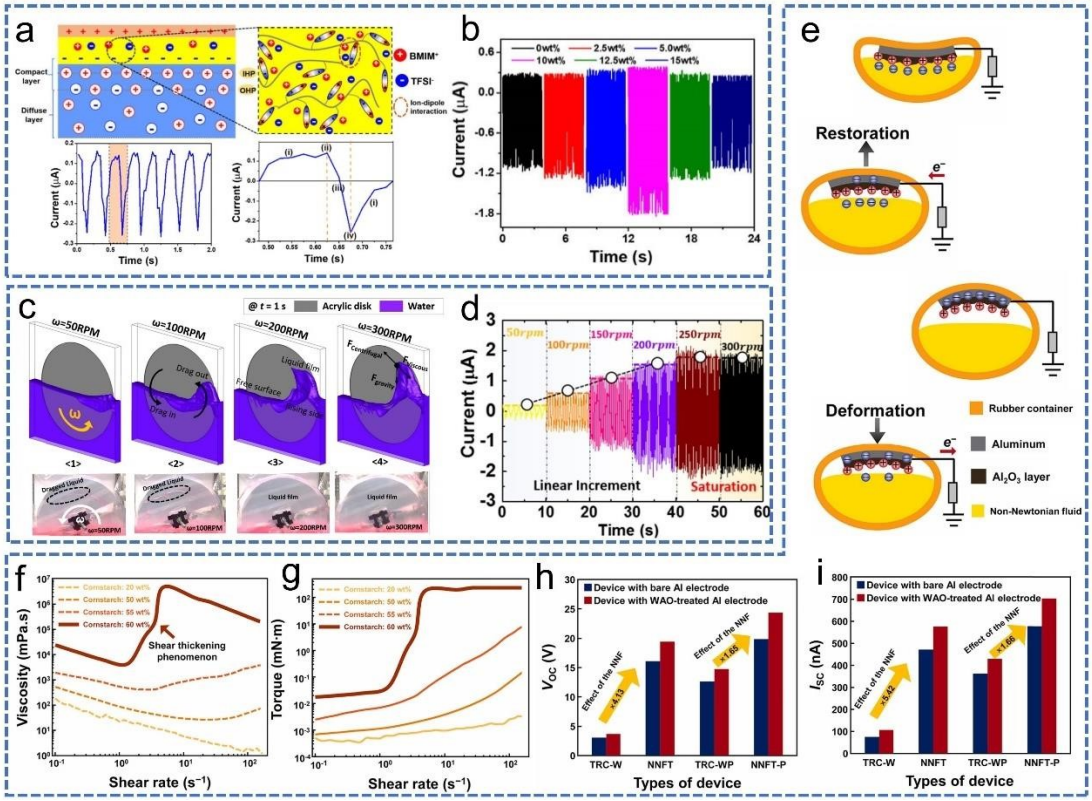

Fig. 6 Influence of the fluid properties. (a) Schematic of the PIL-TENG at the solid-liquid interface based on EDL mechanism and output current of the PIL-TENG under a water flow of 195 mL min^{-1}.[97] (b) Effect on current of different ionic liquid concentrations. (c) Experimental results of liquid film produced by different rotating speeds.[98] (d) The effect of disk speed on output performance. The liquid flow rate is limited by the rotational speed of the disk. (e) The working mechanism of the non-Newtonian fluid-based triboelectric nanogenerator.[101] (f and g) The rheological behavior caused by different weight ratios of raw materials. (h and i) The electrical outputs increase caused due to NNF.

4.1.3 Surface charge density

The selection of liquid is of significant importance in liquid-TENG, as different liquids possess distinct physical properties, including conductivity, dielectric constant, viscosity, and polarity. Ye *et al.*[47] developed a raindrop TENG designed for harvesting energy from irregular raindrops and investigated the impact of varying water quality on the output current of the raindrop TENG. As shown in Fig. 7a, a hydrophobic FEP film with strong electronegativity served as the starter layer, ITO was chosen as the electrode at both the top and bottom, and tap water, deionized (DI) water, rainwater, and seawater were employed as the liquid contact materials, respectively.[47] It can be observed that DI water has the lowest output current, while tap water has the highest output current in Fig. 7b. This is because DI water has the lowest ionic concentration and conductivity, acting as a high resistor when the raindrop TENG is operating, leading to a lower output current. In contrast,

View Article Online
DOI: 10.1039/D4EE00482E

rainwater and seawater have high impurity and ionic concentrations, respectively, affecting the CE process at the liquid-solid interface. Researchers developed a liquid-based TENG for wave energy harvesting and measured the open-circuit voltages in different liquid environments: DI water, tap water, 0.1M NaCl, and seawater, in descending order, and they believed that this phenomenon was caused by the different Debye lengths of the different liquids, and the output voltage shows an inverse relationship with the Debye length. [102,103]

It is also important to study the effect of the counterpart of solid materials for F-TENG based on the liquid-solid interface. Dong *et al.*[104] developed gas-liquid two-phase flow-based TENG (GL-TENG) by utilizing the rheological properties of gas-liquid two-phase flow and investigated the short-circuit currents of DI water and CE of different solid materials. As shown in Fig. 7c, when the external high-velocity gas enters the connection of the pipeline, the liquid at the bottom is sucked out to form a gas-liquid two-phase flow due to the pressure difference, and the rheological properties of the fluid increasing liquid-solid CE area are utilized.[104] Since the friction signal output is dependent on the polarity of the solid material,[27] PTFE, which has a high electron-acquiring capacity(as shown in Fig. 7d), was chosen as the external friction solid.

For the characterization of friction electrical signals of different liquids during liquid-solid CE, Wei *et al.*[105] have done a very comprehensive work. As shown in Fig. 7e and f, a self-powered droplet-tasting sensor system with two single-electrode modes was developed and the friction electrical signals of 14 liquids were measured. In Fig. 7g, the magnitude of the current in white vinegar is significantly smaller than that in drinking water, because the number of free ions in white vinegar is greater than that in drinking water, which inhibits the transfer of charge.[33,106] Besides, liquids also have an effect on the affinity of the solids they come into contact with. Monosodium glutamate (MSG) and sugar water have a poor affinity for FEP, while coffee and liquor are more viscous and adsorb more readily to the FEP surface, resulting in their lower output current. For liquids of different pH values, it can be seen that: the current signal is significantly lower in acidic solutions than in alkaline solutions. This is related to the screen effect of free ions.[107] The friction electrical signal characteristics can be combined with machine recognition to provide ideal sensing capabilities for use in environmental sensing and the food industry.

During the process of contact between liquid and gas, due to the low density of gas, it is difficult for the liquid to fully contact the gas and also difficult to separate. Hence, further research is required on the liquid-gas interface's CE process. Wang *et al.*[66] proposed using the acoustic levitation technique to suspend droplets in different gases. The droplets rotate at very high speeds in the sound waves, maintaining stable friction, causing the charge on the suspended droplets to gradually increase until saturation, and then the charge is discharged through the bottom Faraday cup. Researchers conducted experiments on droplets suspended in N_2, O_2, and Ar with varying levitation times to measure the transferred charge. Friction between air and the levitated DI water droplet results in the droplet becoming negatively charged.[46] The transferred charge in Ar is lower than in N_2 and O_2. Further research is needed on the relevant mechanisms, but this phenomenon suggests that Ar inhibits the CE process of liquid-gas.

View Article Online
DOI: 10.1039/D4EE00482E

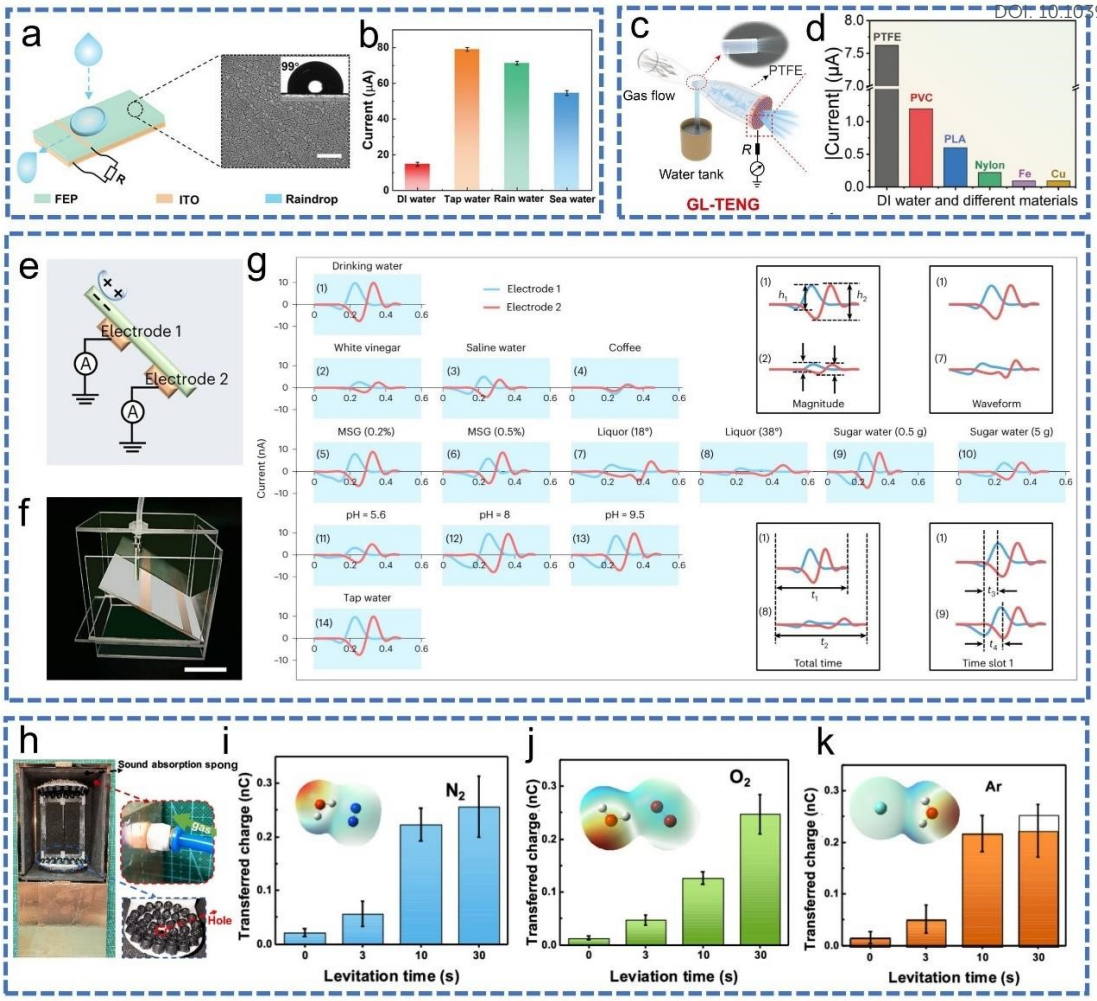

Fig. 7 Effect of different friction materials on output performance. (a and b) Structure of raindrop TENG and output current of different liquid materials in solid-liquid contact.[47] (c and d) Structure of gas-liquid two-phase flow-based TENG and output current of different solid materials in solid-liquid contact.[104] (e and f) Working principle and structure of a droplet-tasting sensor. (g) Characterizations of tribo-electrical signals.[105] (h) The experimental setup of liquid-gas contact electrification.[66] The transferred charge of DI water droplet with different levitation time in a N_2 atmosphere (i), in an O_2 atmosphere (j), in an Ar atmosphere (k).

4.2 Factors influencing gas materials based TENGs

In the field of gas-solid TENGs, it is common to design TENGs that utilize gas flow as a power source, with few utilizing the gas-solid CE process to generate electricity due to the low charge transfer of gas materials resulting from their low densities. In this section, we briefly summarize several factors affecting the efficiency of gas-TENG, including environmental factors, fluid properties, and gas atmosphere, among others.

4.2.1 Environmental factors

In the realm of gas-TENG, the study focuses on the effects of environmental parameters such

as temperature, relative humidity, and air pressure on output performance. As depicted in Fig. 8a, Zhao *et al.*[108] introduced the woven triboelectric nanogenerator flag (WTENG-flag), woven with conductive belts of Ni-coated polyester textiles (Ni belts) and Kapton film-sandwiched Cu belts (KSC belts). This design aims to harness wind energy from all directions using weaving techniques. It is evident that the output current shows a slight reduction as temperature decreases but experiences a significant decrease as humidity levels rise (as shown in Fig. 8b and c). The adsorption of water vapor onto the hydrophobic Kapton surface inhibits the occurrence of surface contact electrification.[108] In addition, Phan *et al.*[109] investigated the influence of air humidity on the output circuit and vibration frequency of a pipeline-type gas-TENG. The external structure consists of a straight, circular transparent polymerizing vinyl chloride (PVC) pipe, with two conductive copper foil electrodes deposited inside the pipe. A thin film is fixed at one end, while the other end can be driven by the wind, causing the electrodes to flap up and down (as shown in Fig. 8d). As depicted in Fig. 8e, as air humidity increases, there is a significant reduction in the output current, while the fluttering frequency remains unchanged. This phenomenon may be attributed to the increased likelihood of charge accumulation with rising humidity levels, leading to enhanced conductivity of moist air and a decrease in surface charge.

To mitigate the adverse effects of humidity on the flag-type TENG and enhance its applicability across various environmental conditions, Wang *et al.*[110] conducted a study on a humidity-resistant flag-type TENG. As illustrated in Fig. 8f, this flag-type TENG consists of two layers of carbon-coated PET sandwiching an intermediate layer of PTFE, with its edges hermetically sealed to isolate the frictional charge layer from the surrounding air, thereby reducing the impact of humidity on its electrical performance. Fig. 8g indicates that under varying humidity levels, this TENG exhibited no discernible variations in output current. This is because the triboelectric layers are isolated from the air, and the flag-type TENG's electricity generation performance is unaffected by the relative humidity of the air. Furthermore, through adjusting the gap distance,[111] the contact area between PTFE and the flagpole electrode was increased, consequently enhancing the output current.[110]

The impact of air pressure on the triboelectric nanogenerator output during the CE process is a crucial factor that demands attention. Zhang *et al.*[112] proposed a rotating TENG with a needle-like ionization structure for CO_2 gas detection. Fig. 8h illustrates the selection of PTFE as the negative tribological material, with printed circuit board (PCB) and copper chosen as positive tribological materials. The TENG's output terminals were connected in series with a pair of needle tips, facilitating gas ionization through TENG rotation. To delve deeper into the influence of air pressure on TENG output performance, gas ionization tests were conducted at pressures ranging from -10 kPa to -60 kPa, as depicted in Fig. 8i. The decreasing air pressure correlated with a gradual increase in output voltage. This phenomenon arises due to the reduction in the number of gas molecules with decreasing pressure, resulting in lower air density and longer molecular free paths. Consequently, electrons accumulate more energy before collisions, rendering free electrons more active and enhancing the TENG's output. This observation is consistent with the findings of Xia *et al.*[113] In their study, metallic glass with a disordered atomic structure, exhibiting excellent wear and

corrosion resistance, was chosen as one triboelectric interface, while FEP served as another tribo-layer, and silver acted as the electrode. Experimental trials conducted in a high-pressure CO_2 environment resulted in a notable 35.2% improvement in charge density.

Environmental factors significantly influence the output performance of gas-TENG. In addition to previously mentioned factors such as temperature, relative humidity, and air pressure, researchers investigated the impact of light intensity and wavelength on CE process between metals and insulators in the past study.[36] When the wavelength is 240 nm, the charge decay rate is highest, and the decay rate decreases with an increase in wavelength. Given that natural environments are pervaded with light, studying the impact of light intensity and wavelength on gas-solid CE is imperative.

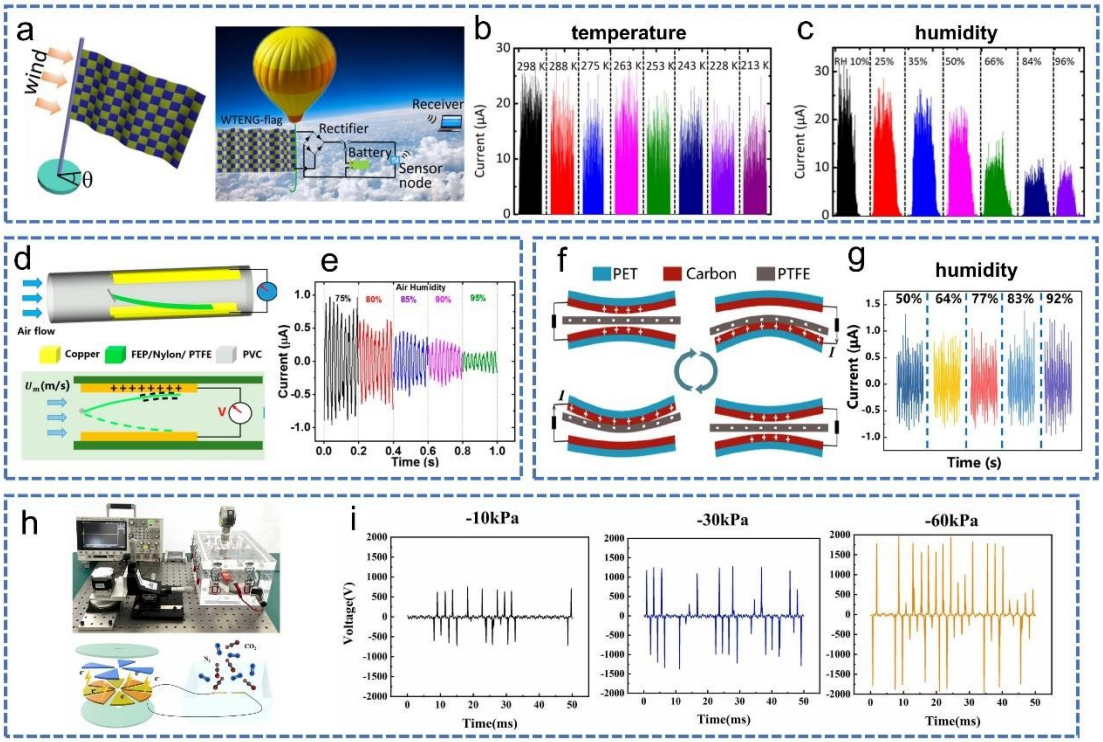

Fig. 8 The effect of environmental factors on output performance. (a) Schematic illustration of the WTENG-flag.[108] (b and c) Effect of temperature and humidity. (d) Schematic diagram of the triboelectric nanogenerator flowmeter and principle.[109] (e) Effect of humidity on the TENG flowmeter output current and flutter frequency. (f) Schematic diagram of the flag-type TENG.[110] (g) Effect of the relative humidity on the power generation performance of the flag-type TENG. (h) Structure and schematic diagram of a self-powered CO_2 gas detection system.[112] (i) Voltage output characteristics after ionization at different air pressures.

4.2.2 Gas properties

In the natural environment, gas molecules undergo irregular motion at high speeds in three-dimensional space, with their motion velocity being directly proportional to temperature. This

View Article Online
DOI: 10.1039/D4EE00482E

thermal motion imparts energy to gas molecules, enabling them to overcome mutual attractions and freely diffuse and flow within a container. Therefore, the velocity and direction of gas motion are crucial factors influencing the output power of F-TENG. As illustrated in Fig. 9a, Zhang *et al.*[114] have reported a flow-induced vibration effect based TENG designed for harnessing breeze energy, continuously monitoring and collecting breezes from various directions. It is evident from Fig. 9b that the output performance is directly proportional to wind speed, with an output voltage and current of 199 V and 10 μA, respectively, observed at a wind speed of 4.3 m s^{-1}. Furthermore, when controlling the wind to blow from a specific direction, this device exhibits voltage generation in every direction, albeit with the single F-TENG unit in direction 3 displaying the highest electrical output(as shown in Fig. 9c). This phenomenon arises from variations in effective contact areas between the wind and units in other directions. Thanks to this exceptional directional capability, a device indicating wind direction even at night can be developed.

The data obtained from the wind barrier designed by Wang *et al.* and the full-packed TENG reported by Zeng *et al.* also support the proportionality of output performance to wind speed.[115,116] As depicted in Fig. 9d and g, both of these structures leverage the flow-induced vibration effect between gas and solid. The primary distinction lies in their respective usage scenarios, with Wang's structure primarily applied to windshield protection for high-speed vehicles and Zeng's structure primarily employed for collecting breeze energy. These differences in application scenarios result in variations in the captured wind speeds. Nevertheless, as shown in Fig. 9e and h, both structures exhibit an increase in output voltage with higher wind speeds, eventually reaching a plateau. This trend has also been confirmed by the works of Xu[117], Liu[118], Wang,[119] Cui,[120] etc. Moreover, the impact of wind turbulence intensity on the power generation performance of the TENG unit is investigated, as shown in Fig. 9f. The open-circuit voltage of the TENG unit gradually increases as turbulence intensity rises from 0.5% to 10%. This is because higher turbulence intensity may disrupt the membrane vibration mode, increasing the local contact area to enhance output performance.

In addition to harnessing electrical energy through the flow-induced vibration effect, alternative methods involve utilizing high-speed gas as a power source to propel tiny liquid droplets or impact gravel against a friction layer[121] in TENGs. As illustrated in Fig. 9i, Xu *et al.*[104] have presented a gas-solid two-phase flow-based triboelectric nanogenerator, with observed output performance initially increasing and then decreasing with velocity in Fig. 9j. The underlying cause of this phenomenon can be attributed to two factors: firstly, within a certain range, the impact force of the gravel on the friction layer surface increases with an increase in velocity; secondly, when the velocity becomes excessively high, the gravel particles tend to overlap, hindering their full contact and separation.[121]

In summary, current research predominantly employs gas as a power source to drive TENGs, with a minimal exploration of harnessing electrical energy generated from the friction between gas and device surfaces. This preference is influenced by several factors, including the challenges associated with gas separation, limited characterization signals, and others, which constitute issues that researchers will need to delve deeper into in future investigations.

View Article Online
DOI: 10.1039/D4EE00482E

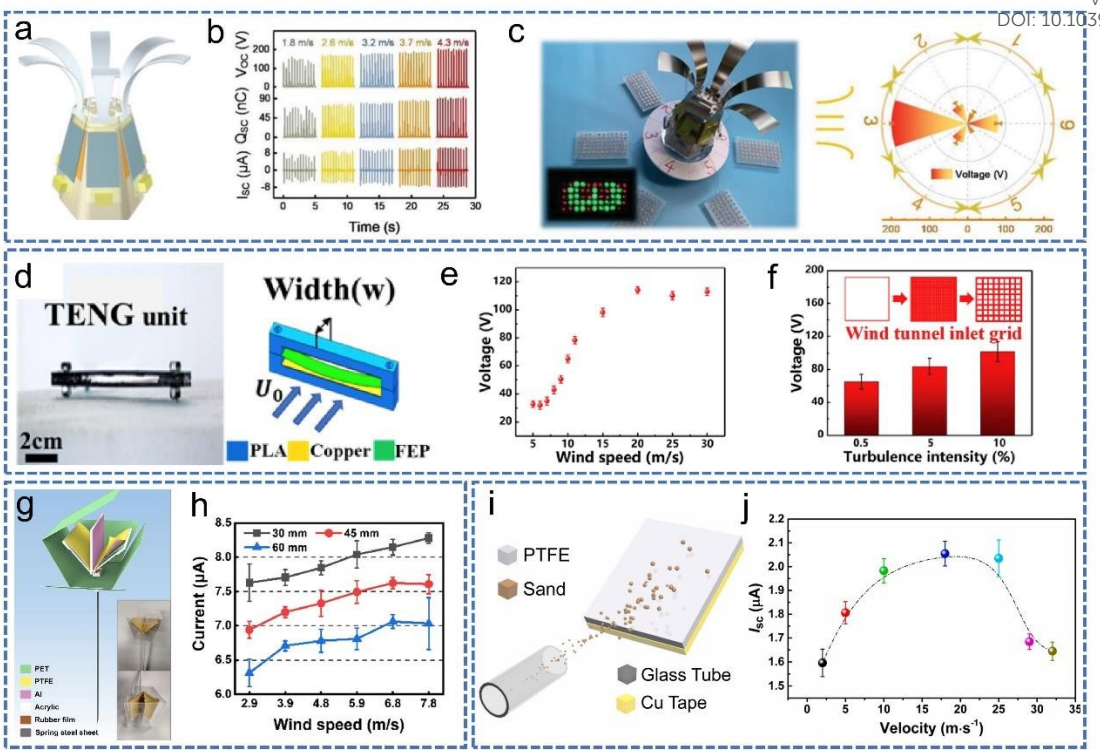

Fig. 9 Effect of velocity and direction on F-TENG. (a) TENG for harvesting multidirectional breeze energy based on fluid-dynamic modeling.[114] (b) The output performance when the unit is perpendicular to the wind direction. (c) A wind direction visual sensor and the V_{OC} of six units when the wind flows in the given direction. (d) The structure of multi-functional wind barrier. (e and h) The correlation between output performance and wind speed.[115] (f) The nexus of V_{OC} and turbulence intensity. (g) Detailed structure of the TENG based on flow-induced vibration.[116] (i) TENG for collecting triboelectric energy in wind-blown sand environment.[121] (j) Plot of I_{SC} versus the flow velocity.

4.2.3 Surface charge density

The surface charge density plays a crucial role in enhancing the performance of high-efficiency triboelectric nanogenerators.[27] However, the increase in surface charge density is consistently associated with a reduction in the thickness of the dielectric layer, an elevation in the dielectric constant, and a decrease in atmospheric pressure.[122] Regarding TENG, the diverse gas atmospheres surrounding triboelectric nanogenerators, especially in the context of gas-TENG, can significantly impact output performance. As illustrated in Fig. 10a, Xiong *et al.*[65] introduced a sticky porous elastomer designed for gas-solid interacted power generation. This elastomer is capable of capturing gases within voids under periodic compression and interacting with the solid matrix. From Fig. 10b, it is evident that output performance diminishes with decreasing air pressure, and the output performance under 10% air surpasses that under inert gases O_2 and Ar.[65] This finding indicates that gases containing more active components promote more effective electron transfer, resulting in increased electrical output. Lv *et al.*[123] presented a fully-enclosed structure for gas-enhanced TENG,

View Article Online
DOI: 10.1039/D4EE00482E

offering a systematic exploration of the impact of different gases on output performance. As displayed in Fig. 10c, the output current is significantly higher when filled with CHF_2Cl and SF_6 compared to when filled with He, Ar, and air. This phenomenon may be attributed to gas collisions with the friction layer, causing the gas to carry some of the opposite charges and thereby reducing surface charge density.[123]

Besides considering the effects of different gases, it is also valuable to investigate the impact of vacuum conditions. The most significant impact of vacuum lies in surface charge density.[124,125] Due to the high voltage output characteristics of TENGs, when the electric field strength exceeds the breakdown field strength of air, molecules in the air become ionized by the electric field, rendering the air conductive. This results in the partial removal of electrons from the material surface, reducing the surface charge density, and causing triboelectric charges to be released through air breakdown before being fully induced into the external circuit. However, under sufficient vacuum conditions, air breakdown is limited and the retention of surface charge density is improved. Wang *et al.*[126] examined the disparities in output performance between vacuum and gas environments. In an equivalent operational mode, the triboelectric charge density of TENG was first improved to 660 μCm−2 in vacuum where the limitation of air breakdown was eliminated, and further to 1003 μCm−2 via coupling of surface and dielectric polarization, which was markedly superior in a vacuum compared to that in air. As shown in Figure 10ef, a vacuum environment enables the illumination of a sequence of 32 light bulbs, whereas, in an air environment, only two can be illuminated.

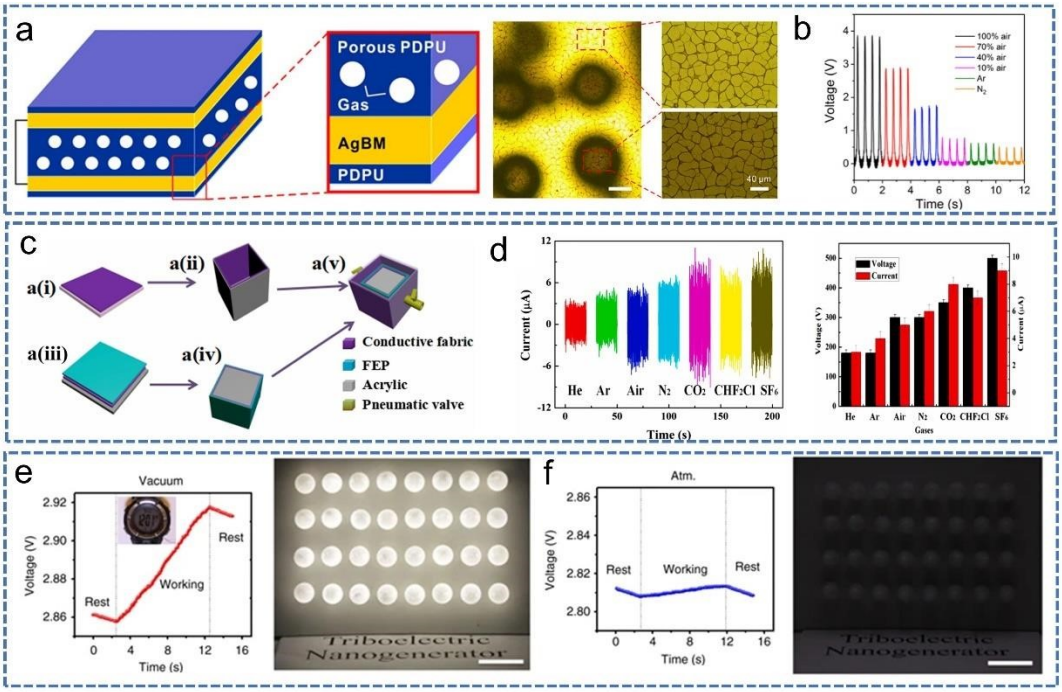

Fig. 10 Effects of different air atmospheres. (a) The structure and microscope image of porous elastomer interacts with the trapped air to generate power.[65] (b and d) Output performance under different gas atmospheres. (c) The structure of a gas-enhanced enclosed cubic-TENG.[123] (e and f)

Comparison of output performance between high vacuum and atmosphere conditions, where the device can fully illuminate under high vacuum but not under atmosphere.[126]

4.3 Surface charge-releasing mechanisms

In theory, triboelectric charges on the solid surface after the CE process should be retained. However, in reality, these charges on the surface are influenced by environmental factors such as humidity, temperature, and light intensity, leading to their disappearance. Firstly, an increase in environmental humidity reduces triboelectric charges. In high-humidity conditions, water molecules in the air adsorb onto the solid surface, forming a water film. The ions and molecules in this water film can conduct electricity, neutralizing the triboelectric charges on the surface and causing them to disappear. Secondly, an elevation in temperature also diminishes triboelectric charges. Researchers have found that triboelectric charges vanish at high temperatures through TENG operation.[25] This is generally attributed to the thermionic emission effect,[127] where, as the temperature rises, electrons gain sufficient energy to overcome the surface barrier and leave the solid. Thirdly, in cases where the energy is sufficient to induce photon excitation, higher photon energy with shorter wavelength leads to a faster decay rate of surface triboelectric charges.[36] Finally, air breakdown has been verified to exist in any operating mode of TENGs.[125] Avoiding the loss of surface charge density caused by air breakdown is a crucial direction for enhancing F-TENGs.[128]

However, there is less research on the surface charge-releasing mechanisms in fluids, with a relatively weak theoretical foundation. Nevertheless, the decay and retention of surface triboelectric charges in fluids are likely still associated with the factors of humidity, temperature, vacuum level and light intensity. Due to the looser molecular arrangement and lack of fixed shape and volume in fluids compared to solids, and the strong energy transfer generated by fluid movement, researchers need to continually explore specific research methods to reveal surface charge-releasing mechanisms in fluids.

5. Application of F-TENG

The F-TENG exhibits considerable potential in the domains of renewable energy and self-powering, characterized by attributes such as high efficiency, cost-effectiveness, environmental sustainability, and adaptability in miniaturization and flexibility. This section provides a concise overview of F-TENG applications in pivotal areas, specifically focusing on energy harvesting and sensor applications.

5.1 Agriculture

Agriculture is a crucial, time-honored, and essential industry in contemporary society.[129] In order to address the continuously growing global food demand, minimize resource wastage, and elevate the precision of farmland management and agricultural decision-making, the amalgamation of contemporary technology with conventional farming methods has led to the emergence of the "smart agriculture" concept. Due to advances in sensor technology, the Internet of Things, and 5G

View Article Online
DOI: 10.1039/D4EE00482E

technology, there has been a consistent growth in the need for a wide array of sensors and the customization of energy sources for microdevices within the domain of smart agriculture.[130] TENG exhibits exceptional efficiency in collecting energy within the micro-nano energy domain. They enable the effective harnessing of dispersed low-frequency mechanical energy from the environment, encompassing sources such as wind energy, river flows, and rainwater. As a result, TENGs serve as a viable solution for meeting the energy requirements of smart agriculture. Furthermore, recent studies suggest that low-frequency high-voltage electric fields have a stimulating effect on plant growth.[131] TENGs possess the capability to transform mechanical energy into electricity through the mechanisms of contact electrification and electrostatic coupling.[25,27] Moreover, they can generate high-voltage electric fields, which have a profound impact on enhancing plant growth. Li *et al.*[132] introduced an all-weather triboelectric nanogenerator specifically designed to generate self-sustained high-voltage electric fields. They conducted a comprehensive study to investigate the influence of these self-generated electric fields on the germination rate of pea seeds and subsequently proposed the development of a self-powered electrical stimulation system (SESS) aimed at optimizing crop growth. As illustrated in Fig. 11a, SESS consists of a bearing-and-hair structured TENG and a raindrop-driven TENG, specifically designed for efficient energy harvesting from wind and raindrop sources. Notably, the bearing-and-hair structured TENG (BH-TENG), featuring a rotating-disk structure, stands out for its high voltage output and remarkable stability, often serving as a preferred choice for high-voltage power sources.[58,133–135] To overcome the traditional issue of friction layer wear in rotating-disk TENGs, researchers adopted improvements, including the integration of rabbit fur and bearing structures, resulting in a reduction of the starting torque to -8.33% while maintaining commendable output performance. BH-TENG consistently delivers stable outputs across wind speeds ranging from 0.5 m s^{-1} to 6 m s^{-1}, achieving peak voltages of up to 3 kV. In the case of R-TENG, it demonstrates consistent output performance under various raindrop frequencies and pH values, achieving a maximum charge transfer of 20 nC and an instantaneous output power density of -1 W m^{-2}. Furthermore, as depicted in Fig. 11a, seeds subjected to electrical field treatment exhibited significant enhancements in germination potential and yield, approximately 26.3% and 17.9%, respectively. This further underscores the positive impact of self-powered electrical stimulation on crop growth.

Smart agriculture is a farming practice that leverages information and communication technologies (ICT) to enhance agricultural productivity, sustainability, and the quality of agricultural products.[136] Its development relies on the utilization of sensors, automated equipment, and the Internet of Things, in addition to the necessity for robust infrastructure and accompanying Internet connectivity. Modern farms are typically situated in expansive regions such as plains, plateaus, and coastal areas, which often boast abundant wind energy reserves. This natural renewable energy source can be harnessed to provide power for microsensors and displays. Han *et al.*[134] have engineered a rabbit fur-based rotary triboelectric nanogenerator for wind energy harvesting, which finds application in self-powered devices within the realm of smart agriculture. As depicted in Fig. 11b, placing the soft-contact rotary TENG (SCR-TENG) in wind-rich areas, such as rooftops and

slopes, enables it to supply power to LED bulbs for nighttime directional indicators and ultraviolet lamps. Under normal circumstances, the SCR-TENG achieves its peak power output at a wind speed of 6 m s^{-1} and can charge a 1000 μF capacitor to 1.3 V in 120 seconds, attaining a mechanical-to-electrical conversion efficiency of 15.4%.

Greenhouses serve as controlled environments conducive to the implementation of a diverse array of technologies and practices in smart agriculture. In the conventional sense, greenhouses refer to agricultural plastic greenhouses (APGs), which are arch-shaped structures covered with plastic film designed for the regulation of internal climate conditions.[137] The efficient collection of energy on a large scale is integral to the operation of modern greenhouses. In the context of smart agriculture, a central focus is on the efficient capture of low-frequency and irregular mechanical energy from the surrounding environment. In certain regions, extensive integration of photovoltaic systems is utilized to harness solar energy for the electrification of greenhouses.[138–140] Nevertheless, due to reduced sunlight duration and heightened precipitation in specific areas, the photovoltaic industry cannot fully meet the electricity demands of smart agriculture. Therefore, the harvesting of mechanical energy from raindrops in these regions emerges as a promising solution for powering greenhouses and a variety of sensors. As shown in Fig. 11c, Zhang *et al.*[141] proposed the utilization of a fluorinated superhydrophobic film for the structural elements of greenhouses, serving as a negative frictional electric layer material in the design of a raindrop energy harvesting triboelectric nanogenerator (RDE-TENG). This film exhibits remarkable superhydrophobic properties, negative electrical charge characteristics, and high levels of transparency. It includes dual electrodes to maximize the efficient collection of energy generated by the descent of raindrops.[55] The RDE-TENG consistently maintains a stable output even when subjected to varying raindrop frequencies, acidity levels, and impact heights, displaying impressive performance in diverse rainy conditions. Upon connecting the RDE-TENG to a supercapacitor and a rectifier bridge, raindrops continue to fall onto the thin film surface. The resulting alternating current is subsequently rectified and utilized to charge the supercapacitor, effectively powering timers, temperature sensors, and humidity sensors. The successful application of the RDE-TENG plays a pivotal role in facilitating the construction of smart greenhouses and advancing the field of agriculture through the deployment of various self-powered sensors.

Efficient, precise, and controlled pesticide release is a critical component of the smart agriculture framework. Precise pesticide management contributes to the reduction of pesticide overuse, cost savings, improved resource utilization, and the mitigation of environmental pollution issues. As illustrated in Fig. 11d, Zhang *et al.*[142] introduced an inverted pendulum-typed multilayer triboelectric nanogenerator (IPM-TENG) designed to harness energy from water wave motion, particularly in environments with weak wave conditions. They also developed a controllable pesticide release system. By connecting the IPM-TENG between the two plates of a capacitor, the resulting alternating current generates an electrostatic field that propels a carrier containing glyphosate forward. Remarkably, the concentration of glyphosate is directly proportional to the distance traveled. This phenomenon underscores the effectiveness of the controllable pesticide

View Article Online
DOI: 10.1039/D4EE00482E

release system in minimizing the loss of pesticide concentration and ensuring precise control of pesticide concentration at the desired location.

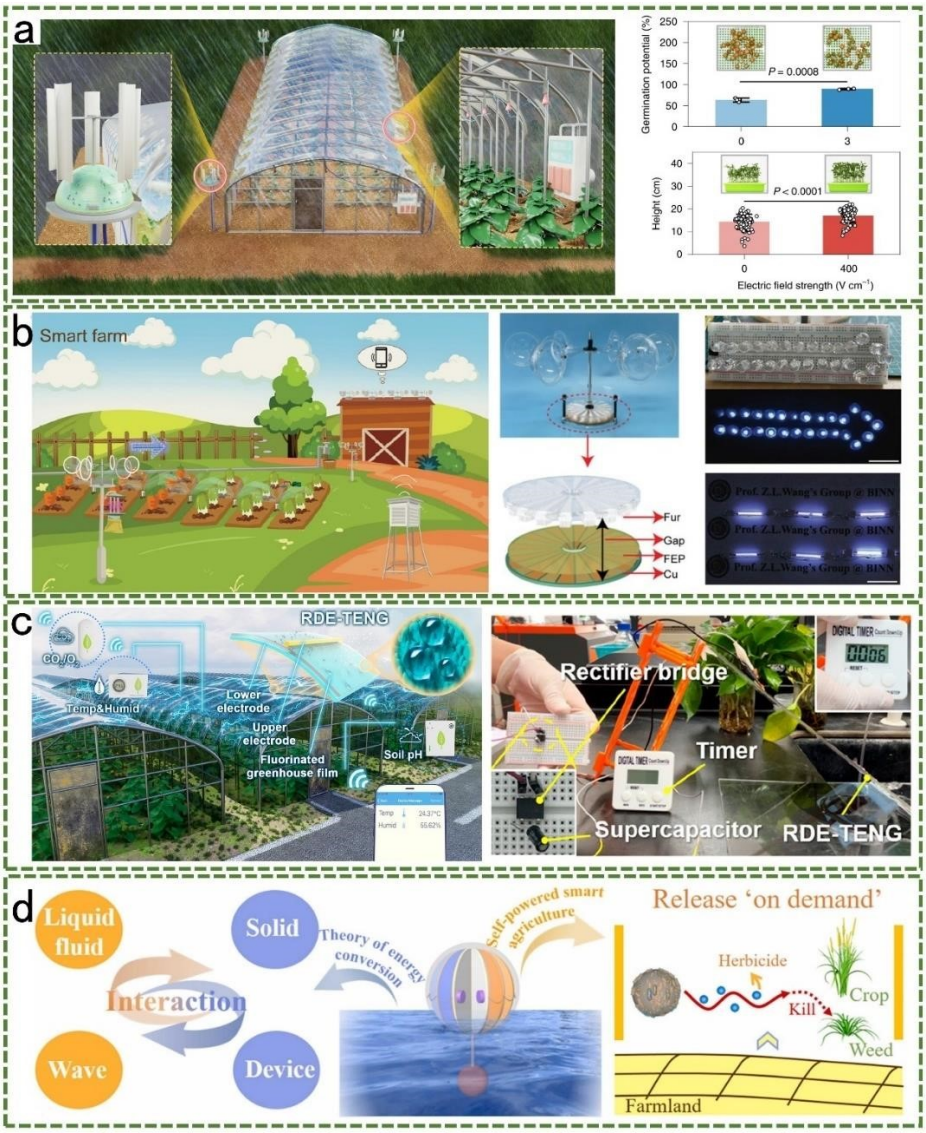

Fig. 11 The application of F-TENG in agriculture. (a) A self-powered electrical stimulation system (SESS) for enhancing agricultural production.[132] (b) Smart farm based on SCR-TENG for harvesting low-speed wind energy.[134] (c) A self-powered intelligent greenhouse.[141] (d) a console for releasing pesticides based on IPM-TENG.[142]

5.2 Internet of Things

The Internet of Things represents a technological concept that connects various physical entities in the real world, such as wearable electronics,[143,144] electronic skin,[143] environmental safety, and wireless transmission,[145,146] through the Internet and electronic communication technologies to enable interaction.[147] TENGs have proven to be promising in low-frequency energy harvesting, suitable for everyday low-frequency motions.[148] Furthermore, TENG-based sensors exhibit self-

powered characteristics, making them highly prospective in the field of the Internet of Things.[149,150] In circumstances involving adverse environments or unreliable energy supplies, electronic devices deployed within such environments necessitate an energy supply method that is more adaptable to their surroundings. Xu *et al.*[151] have presented a groundbreaking solution in the form of a hybrid all-in-one power source (AoPS). The AoPS seamlessly integrates a spherical TENG with solar cells, enabling the stable collection of energy from environmental sources, including wind, raindrops, and sunlight. Illustrated in Fig. 12a, TENG units are symmetrically positioned at the tips of four arms. Each TENG unit consists of a spherical Polypropylene(PP) shell, FEP friction particles, and a copper electrode disk. Commercial-grade solar cells are strategically placed on both sides of the framework structure. Under challenging natural conditions characterized by strong winds or heavy rainfall, the AoPS consistently rotates along the same direction around the flexible shaft, facilitating the frictional interaction between the FEP particles and the electrode disk. This innovative structural configuration yields nearly continuous direct currents and achieves an impressive average power output of 5.63 mW. Notably, a single unit is capable of illuminating up to 1160 LEDs. The adaptability of this all-in-one energy collection system to diverse natural environments establishes a solid energy foundation for the growth and development of the Internet of Things.

In the era of the Internet of Things, wearable electronic devices play a pivotal role as essential components within the IoT ecosystem. These devices, integrated with TENG, offer users the ability to monitor vital signs and power small electronic appliances. Heo *et al.*[152] have introduced a charge-accumulating-flutter-based triboelectric nanogenerator (CAF-TENG) that can be seamlessly integrated into a mask valve, providing power to electronic devices and more. As illustrated in Fig. 12b, the operating principle of the CAF-TENG relies on structural flutter induced by the flow of gas, making it adaptable to a wide range of gas flow scenarios, and the CAF-TENG has been successfully integrated into a mask valve, allowing its passive utilization in everyday respiration. Researchers have categorized breathing frequencies into two distinct modes: normal breathing (characterized by slow respiration) and abnormal breathing (characterized by rapid respiration). In these two distinct modes, the CAF-TENG achieved peak voltages of 508 V and 238 V, delivering continuous power to eight commercial LED arrays throughout the breathing process and supplying power to Bluetooth sensors. This integrated mask valve additionally boasts the capability to accurately monitor the user's respiratory condition, thereby functioning as a respiratory monitoring tool and a portable energy source for daily life. Furthermore, Park *et al.*[153] have developed a multi-layered composite thin-film triboelectric nanogenerator (M-TENG) that combines TENG with biomimetic synapse transistors, serving as a low-power artificial synapse device. Through mechanical memory training, they have successfully demonstrated the plasticity of artificial synapses. In contrast to traditional TENG, which generates two distinct peaks during a single contact—occurring during both the contact and separation processes—M-TENG utilizes spacers to separate the friction layers, delaying the separation process. This innovative approach enables the generation of multiple peaks, rendering it well-suited for use as an artificial neural synapse.

In high-altitude environments, the slightest air turbulence can trigger vibrations in overhead

View Article Online
DOI: 10.1039/D4EE00482E

power transmission lines. These vibrations have the potential to induce fatigue in the line towers, thereby posing significant threats to both transmission performance and safety. To proactively address the long-term effects of mild winds, an extensive array of sensors distributed widely along transmission lines is essential for monitoring natural wind patterns.[154] To tackle this challenge, Tang *et al.*[155] have introduced a self-powered system based on TENG designed to detect ambient wind conditions. As illustrated in Fig. 12c, this innovative system not only records but also analyzes the duration of wind-induced vibrations experienced on the transmission lines. This rotation-based TENG functions by meticulously analyzing electrical signals over time and identifying the positions of peak voltage and intermediate voltage values. These insights allow it to precisely determine the direction of the prevailing wind. Within the wind speed range of 1.7 m s^{-1} to 6.7 m s^{-1}, the system exhibits an initial increase in output performance followed by stabilization. At a wind speed of 6.7 m s^{-1}, the short-circuit current attains its peak value at 168 nA.

Rainfall detection plays a crucial role in providing timely weather information, and facilitating proactive measures and decision-making. As such, the prompt and reliable transmission of information is paramount.[156] Traditional battery-based power sources are vulnerable to failure in natural rainy conditions. An apparatus capable of consistently harnessing energy from the environment and supporting sensing functions should not be underestimated. Xu *et al.*[49] have introduced an autonomous rainfall monitoring and wireless transmission system (R-RMS) based on raindrop-TENG. Under rainfall intensity conditions of 71 mm min^{-1}, the R-TENG demonstrates the ability to generate a maximum output power of 325 μW and an average short-circuit current of 15 μA. After rectification, the system provides a stable 2.5 V DC output.[49] As depicted in Fig. 12d, the researchers have attached a PTFE film to the surface of the copper electrode and improved the material's hydrophobicity through surface modification. The raindrop-TENG operates in a single-electrode mode and quantifies rainfall by measuring voltage. This system amalgamates raindrop energy harvesting and sensing, resulting in autonomous and sustainable rainfall sensing and detection. It holds great promise for outdoor monitoring and applications in the IoT.

View Article Online
DOI: 10.1039/D4EE00482E

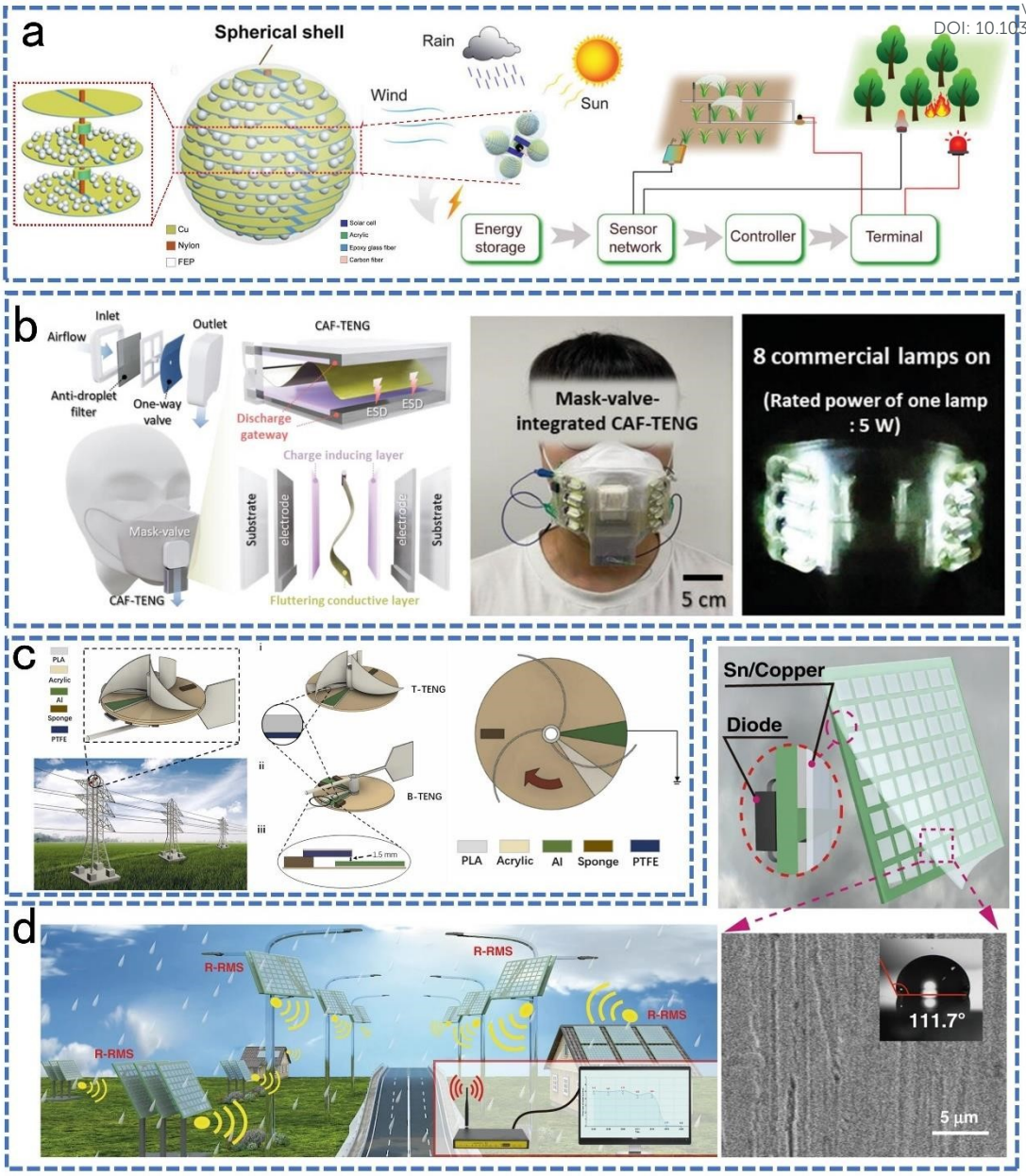

Fig. 12 The application of F-TENG in Internet of Things. (a) A hybrid all-in-one power source based on TENG.[151] (b) Portable self-powered mask valve based on TENG.[152] (c) Monitoring ambient wind conditions over long distances.[155] (d) Arrayed rows of raindrop energy harvesters and sensors.[49]

5.3 Transportation

In recent years, there has been an increasing fascination with smart transportation systems for their capacity to optimize traffic flow and improve traffic management.[157,158] Smart transportation systems leverage an array of sensors in conjunction with communication technologies, automation, and data analytics to intelligently address traffic-related challenges. Their objective is to enhance the efficiency, sustainability, and safety of urban transportation and residents' mobility.[159] He *et al.*[83] have introduced a liquid suspension triboelectric nanogenerator (LS-TENG) based on a horizontal sliding mode lubricated with dielectric liquid, featuring an impressive charge density of 704 μC m^{-2}.

View Article Online
DOI: 10.1039/D4EE00482E

Their innovative non-contact design avoids direct friction on the friction layer, which, although it reduces certain aspects of power generation efficiency,[4] significantly extends the durability of TENG operation. Thanks to the remarkable output stability and durability achieved through this dielectric liquid lubrication, this TENG finds wide application in outdoor environments. For example, when equipped with a rotor for collecting environmental wind energy, as depicted in Fig. 13a, it can be employed as a crash detector or to power safety indicators.

During the high-speed travel of trains, a substantial amount of wind energy is typically generated. To address the energy requirements of the numerous sensors along high-speed train routes, Zhang *et al.*[160] have reported the development of an elastic rotation triboelectric nanogenerator (ER-TENG) designed to harness wind energy generated during high-speed train travel. As depicted in Fig. 13b, the ER-TENG is typically positioned on both sides of the railway tracks. When a train passes by, the generated wind energy propels the rotators, inducing friction with the friction layer and generating electrical power that can be used to power sensors or traffic indicators. Under simulated wind speeds of up to 20 m s^{-1}, the double-layer ER-TENG has demonstrated output capabilities of 0.9 μC, 120 μA, and 600 V, respectively. The ER-TENG has the potential to simplify electrical distribution in specific railway sections by continuously harnessing wind energy instead of relying on depleting fossil fuels, providing power to large-scale railway sensor networks[161] and potentially traffic indicators. In severe weather conditions with strong winds, simultaneously collecting wind energy and monitoring wind speed on a single device without external power support becomes a challenging task. He *et al.*[162] have addressed this challenge by introducing a dual-mode TENG composed of alternating current output and direct-current output sections, which exhibits remarkable durability and real-time sensing capabilities. This mode of TENG only experiences a 13% attenuation after 1,200,000 cycles, and it can achieve a peak average power output of 267.3 mW. Even in adverse conditions with wind speeds of up to 16 m s^{-1}, it can reliably deliver severe weather warnings. The dual-mode triboelectric nanogenerator presents a promising strategy for the development of self-powered sensors in smart transportation.

In the present era, as the number of automobiles continues to grow, road traffic density is increasing accordingly. Previous research has unequivocally demonstrated that fatigue while driving can result in drivers losing control and mastery over their vehicles.[163] In order to prevent fatigue-related accidents and bolster road traffic safety, real-time monitoring of driver fatigue status, coupled with timely warnings, is of paramount importance. Lu *et al.*[164] have introduced a stretchable polyacrylamide (PAAM)-LiCl-based triboelectric nanogenerator (PL-TENG) that is strategically positioned on a driver's face and neck, facilitating precise monitoring of facial and neck movements with remarkable accuracy. As depicted in Fig. 13c, the research team has harnessed parameters such as eye blink duration (BD), blink interval duration (BID), percentage of eyelid closure over time (PERCLOS), and yawn frequency (YF) to gauge the extent of driver fatigue. Distinct actions generate unique characteristic signals, and an algorithm is employed to analyze the driver's fatigue level based on the collected data, determining the necessity for a timely warning. The PL-TENG boasts high voltage output and exceptional biocompatibility, surpassing the performance of methods

relying on camera-based facial feature capture as demonstrated by Liu et al[165] and Divjak *et al.*[166] This advantage is particularly pronounced in conditions characterized by rapid changes in lighting. Lu *et al.*'s PL-TENG represents a pivotal contribution to the ongoing developments in sensing and bionics within the realm of smart transportation.

During maritime navigation, maintaining the proper orientation of a vessel is of paramount significance. The correct alignment of a vessel significantly impacts its stability, safety, and navigational efficiency. Stability, in particular, plays a pivotal role in ensuring that vessels remain resistant to capsizing or tilting in diverse sea conditions, as an incorrect vessel orientation can lead to adverse consequences such as capsizing, unstable navigation, cargo displacement, and passenger injuries.[167] Therefore, real-time monitoring of a vessel's orientation is of utmost importance in maritime and offshore operations. Wang *et al.*[168] introduced a vessel orientation monitoring device based on the triboelectric nanogenerator with a ring-shaped liquid-solid interface. This device distinguishes itself from traditional mechanical tilt sensors and electronic tilt sensors due to its structural simplicity, maintenance-free operation, high durability, and resilience to adverse maritime conditions.[168] As depicted in Fig. 13d, the ring-shaped TENG is securely affixed to a horizontal plane and can adjust its position in response to the vessel's rolling motion. The annular tube is constructed from PTFE material, and it is equipped with external copper metal electrodes. A liquid is uniformly distributed at the base of the circular tube. The tilt angle is determined by assessing the arc length of the internal liquid flow. The real-time vessel tilt angle can be activated through the electric signals generated by the friction between water and PTFE tube. Simultaneously, an LED indicator reflects the tilt angle. Furthermore, in cases where the vessel's tilt exceeds a hazardous threshold, the alarm system is triggered to alert the crew for necessary evacuation procedures. Given the unique nature of the maritime environment and vessel movements, harnessing oceanic energy from a vessel platform offers distinctive advantages. Wei *et al.*[169] introduced a nonpackaged all-weather triboelectric nanogenerator that relies on the vessel's stable and sufficiently spacious structure, as well as the electrostatic shielding properties of the ship's hull. When driven solely by a 1.5 mL droplet, the open-circuit voltage, short-circuit current, and surface charge density can reach 77.0 V, 52.0 nA, and 153.5 μC m^{-2}, respectively.

View Article Online
DOI: 10.1039/D4EE00482E

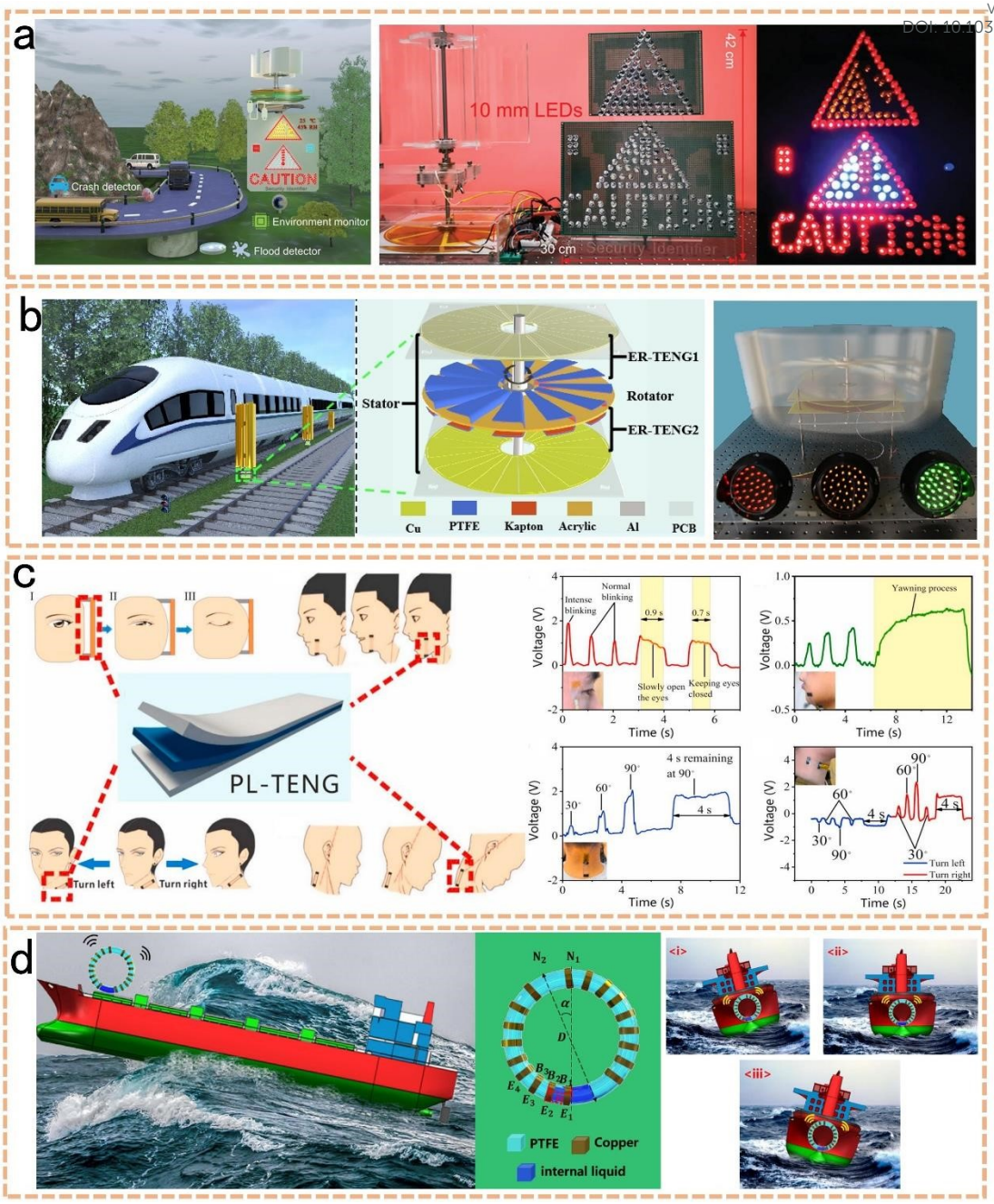

Fig. 13 The application of F-TENG in Transportation. (a) LS-TENG can capture the wind or water energy in the environment to power the surrounding sensors such as accident sensor.[83] (b) Recovery of wind energy generated by high-speed trains based on ER-TENG.[160] (c) Driver fatigue detection based on TENG.[164] (d) A self-powered tilt for ship attitude sensing.[168]

5.4 Environment protection

The natural environment and climate changes have recently exerted a significant impact on biodiversity,[170] industry,[112] agriculture[171] and human health.[53,119] To maintain ecological balance and biodiversity, protect human health and safety, ensure a stable food supply, and promote sustainable development, environmental protection and monitoring are considered effective solutions. Flexible

TENGs are characterized by their low cost, compact size, and diverse material options.[172] They are highly suitable for outdoor environmental monitoring and early warning systems, with promising prospects for application. Among all air pollutants, the complete elimination of nitrogen oxides (NO_x) is relatively challenging. Furthermore, as NO_x is a primary component of acid rain,[173] employing suitable methods for NO_x degradation can contribute to air quality improvement, climate change mitigation, and the protection of cardiovascular health, among other benefits.[174] Han *et al.*[175] reported a wind-driven triboelectric nanogenerator for the degradation of NO_x, designed for outdoor environmental applications. As shown in Fig. 14a, the device operates primarily by harnessing wind energy from outdoor environments through TENG and converting it into electricity. When integrated with wind cups and placed at elevated positions on roadside lampposts, the generated electricity can be directed for NO_x degradation through a Ni-Pt electrocatalytic system or absorbed into a liquid using an air pump. Five TENGs were stacked together, with alternating operation. At a rotation frequency of 3 Hz, the short-circuit current reached 20 μA, which is 4.76 times the output of a single TENG. Compared to traditional pressurized catalysis, this self-powered catalytic system offers the advantages of low cost and high efficiency. It is particularly well-suited for the treatment of small quantities of NO_x in outdoor environments and serves as a complementary approach to conventional degradation methods, thereby offering valuable insights into achieving sustainable environmental and health outcomes.

In natural forest environments, various factors, such as fire ignition due to lightning, hot and dry weather conditions, and vegetation drought, can easily lead to forest fires, resulting in widespread impacts on the natural environment, wildlife, and the physical and mental health of individuals.[176] To address the issue of remote forest fire warnings, as illustrated in Fig. 14b, Fu *et al.*[177] proposed a triboelectric nanogenerator that relies on charge excitation and automatic mode switching, transitioning between contact mode at low speed and non-contact mode at high speed. This device is designed for the collection of water flow energy and intelligent forest sensing. The device is divided into two parts: the upper part, which serves as the generator for rotational power generation, and the lower part, which functions as a waterwheel for collecting water flow energy to drive rotation. During the operation of the device, the alternating current (AC) electrical signals generated by the E-TENG are rectified to direct current (DC) signals using a rectifier, which are then used to charge the storage electrodes of the M-TENG. Ultimately, under the high-speed rotation of the M-TENG, alternating current signals are generated through electrostatic induction. These signals are capable of charging 470 μF and 1000 μF capacitors to 3.5 V within 26 and 85 seconds, respectively. Additionally, they can drive commercial water temperature sensors or fire alarm devices. This device exhibits high durability and stable large current output, making it suitable for self-powered fire monitoring in remote areas such as unattended forests.

A long-term and wide-area environmental monitoring network can provide a variety of information by monitoring extensive climate changes, including long-term climate trends and early climate anomaly warnings.[178] However, the widespread use of satellite imaging is costly, energy-intensive, and demands substantial equipment support.[179] In response to this challenge, Liu *et al.*[180]

proposed a low-cost and long-range self-powered wireless monitoring node network capable of detecting environmental temperature, humidity, and atmospheric pressure. This overcomes the drawbacks of traditional monitoring systems that rely on grid power or batteries. As shown in Fig. 14c, this device consists of a vertical wind turbine and an independent wind turbine TENG, with the stator positioned above the rotor. This arrangement resolves the issue of reduced operational efficiency caused by electrostatic adhesion between the stator and rotor. The output of the TENG increases with the wind speed, with a maximum stable output wind speed of approximately 4 m s^{-1}. The peak open-circuit voltage reaches 6 kV, and the maximum transferred charge is approximately 0.38 μC. Through the power management circuit, it is capable of charging a 3.3 mF capacitor to 5 V in 280 seconds. Regional monitoring can be achieved by placing multiple wireless nodes at different distances from the receiver.

To achieve goals such as reducing greenhouse gas emissions, electric vehicles are becoming increasingly popular.[181] However, the disposal of lithium-ion batteries from scrapped cars poses a severe environmental challenge. Proper post-processing of waste lithium-ion batteries is essential to prevent environmental pollution and resource wastage.[182,183] To address this issue, Zhang *et al.*[177] reported a material and energy dual-cycle approach based on R-TENG (TENG made from recycled parts) for the continuous recycling of components from discarded lithium batteries or lithium iron phosphate batteries.[184] This efficient energy utilization approach involves two key processes: firstly, recycling positive electrode materials and creating new batteries from the recovered materials; secondly, utilizing discarded components such as PVDF, Cu/Al foils to construct R-TENG, which harnesses wind energy to enhance the continuous power of the batteries for reuse. As shown in Fig. 14d, the R-TENG fabricated from recycled materials converts wind energy into electricity with the assistance of a wind turbine. Through a transformer, the electricity is rectified into high current and low voltage suitable for the dual-electrode recycling system, enabling the recycling of positive electrode materials. This entire process is environmentally friendly, cost-effective, and straightforward, addressing the environmental hazards associated with traditional recycling processes,[185] and holds significant promise in the field of environmental protection.

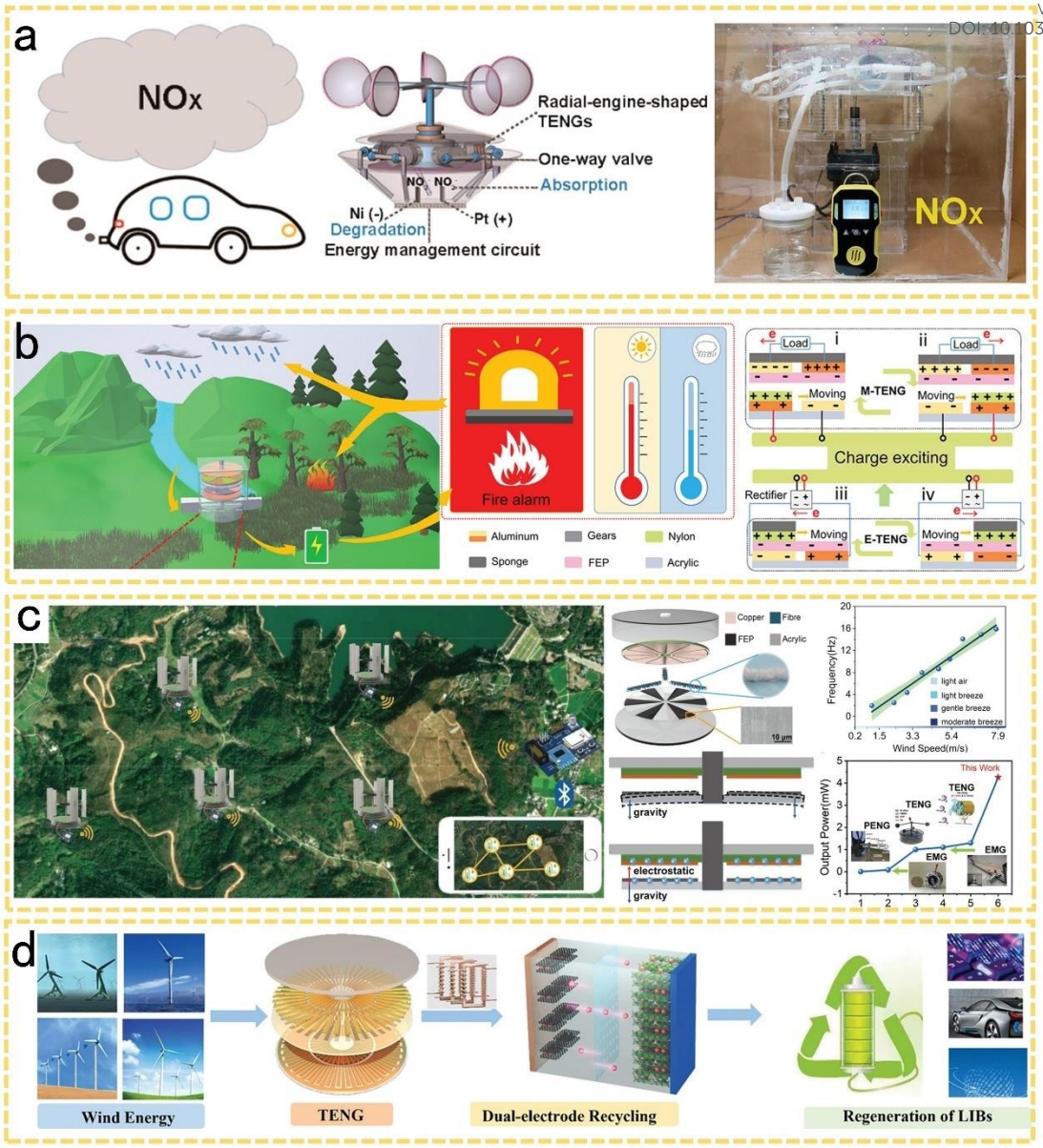

Fig. 14 The application of F-TENG in Environment Protection. (a) NO_X absorption and degradation system based on TENG.[175] (b) Water-flow energy harvesting and intelligent forest monitoring by the CEMA-TENG.[177] (c) A self-powered wireless sensing network to achieve long-term and wide-area local temperature, humidity, and atmospheric pressure monitoring.[180] (d) Self-powered system for recycling used LFP batteries by capturing wind energy through TENG.[186]

5.5 Manufacturing and industry

A significant characteristic of the F-TENG is its choice of liquid as the contact medium. Liquids exhibit a diverse range of properties, including fluidity and viscosity. These characteristics aid in reducing losses caused by friction in F-TENG, enabling the collection of a broader spectrum of environmental energy. In the industrial sector, the extensive involvement of liquids in processes such as cooling, heating, and chemical reactions contributes to the maintenance of production efficiency, quality, and sustainability, playing an indispensable role. Particularly in chemical

View Article Online
DOI: 10.1039/D4EE00482E

reaction processes, precise control of liquid droplet motion, separation, and the combination is essential to facilitate their role.[187] Sun *et al.*[80] proposed a novel method involving the use of tribo-electrophoresis (TEP) to move liquid within an oil medium, enhancing the efficiency of human-liquid interactions. As illustrated in Fig. 15a, liquid droplets are suspended in dimethyl-silicone oil, with an electrostatic tweezer directly connected to the TENG positioned above them.[188] The TENG can be directly manipulated by human hands, providing the freedom to control both the distance and the position of movement. Once the TENG is set in motion, the liquid droplets can move either vertically or horizontally under the electric field generated by the TENG. To achieve more precise control over liquid droplet motion, Sun *et al.*[80] systematically investigated the forces governing droplet behavior within the oil medium, as well as the impact of the voltage generated by TENG sliding on droplet motion height, velocity, and related factors. 45 mm TENG sliding results in a charge of 0.04 nC being carried by a 5 μL liquid droplet, achieving a maximum control speed of 15 mm s^{-1}. In addition to the TEP approach, Sun *et al.* also proposed a method involving the transfer of charges through TENG and the provision of an electric field to inject a substantial quantity of charges into liquid droplets via contact with electrodes, thereby driving liquid droplet motion, achieving control.

In the industrial production domain, lubricating oil serves as a lubricant,[189] and hydraulic oil plays a vital role in transmitting force, facilitating operations, and monitoring machine faults.[190] However, oils often give rise to issues like impurity adsorption and oxidation, which can have implications for machinery and industrial monitoring. As depicted in Fig. 15b, Zhao *et al.*[191] developed a high-performance coating for controlled surface wettability in oil-solid contacts. This coating exhibits enhanced electron affinity and improved oil resistance, enabling the fabrication of oil–solid TENG (O-TENG) with high output and durability. The O-TENG achieves open-circuit voltage and short-circuit current values of 22.5 V and 50 nA, respectively. It can charge a 33 μF capacitor to a voltage of approximately 2.5 V within 220 seconds. Building upon their previous work, Zhao *et al.* introduced a superoleophobic surface, endowing the FO-TENG with excellent self-cleaning properties in oily environments. As the water content in the oil increases, the output voltage also increases, enabling high-sensitivity real-time monitoring of lubricating oil quality. In industrial and laboratory settings, fluid control often requires the monitoring of liquid characteristics, such as ion concentration in water. However, most existing sensors currently face issues such as the need for external power sources, complex sensing processes, and challenges in real-time monitoring. To address the challenges associated with current ion detection sensors in water, Chen *et al.*[192] proposed a self-powered online ion concentration monitoring device based on a triboelectric nanogenerator. It comprises a rotary disc-shaped TENG (RD-TENG) and an ion concentration sensor. Both the RD-TENG and the ion concentration sensor are fabricated using printed circuit board technology, allowing for process simplification through integration. As shown in Fig. 15c, the RD-TENG is mounted on a turbine, converting the mechanical energy from water flow into electrical energy, which directly powers the ion concentration sensor connected in the circuit. When there is a slight increase in ion concentration within the water pipe, the LED alarm system responds in real-time. This response is due to the fact that as ion concentration in the water increases, the

water's electrical conductivity rises, resulting in a reduction in resistance between the sensor electrodes. Even a minor change in ion concentration, as low as 1×10^{-5} mol L^{-1}, can trigger the LED alarm. These sensors exhibit high sensitivity and low power consumption, offering significant prospects for applications in monitoring ion concentration in pure water.

To efficiently and non-intrusively monitor the movement of liquid droplets without affecting the flow inside the pipeline, nonintrusion monitoring is commonly employed.[193] Unlike traditional intrusion monitoring, which involves inserting probes into the pipeline for measurements, nonintrusion monitoring avoids the impact of sensor components on accuracy.[194] Song *et al.*[195] proposed a method for nonintrusion monitoring of charged liquid droplets based on liquid-solid contact. As shown in Fig. 15d, the triboelectric droplet motion state sensor (TDMSS) is composed of a T-junction, a PTFE tube, and three copper electrodes, along with a pneumatic system used for droplet cutting and driving. In the flow range of 2 to 22 mL min^{-1}, TDMSS can accurately detect the quantity and motion state of deionized water, demonstrating excellent stability and responsiveness. This nonintrusive monitoring method based on liquid-solid contact triboelectric sensors can enhance reference and guidance in areas such as hospital bed monitoring, drug transport, and industrial control.

View Article Online
DOI: 10.1039/D4EE00482E

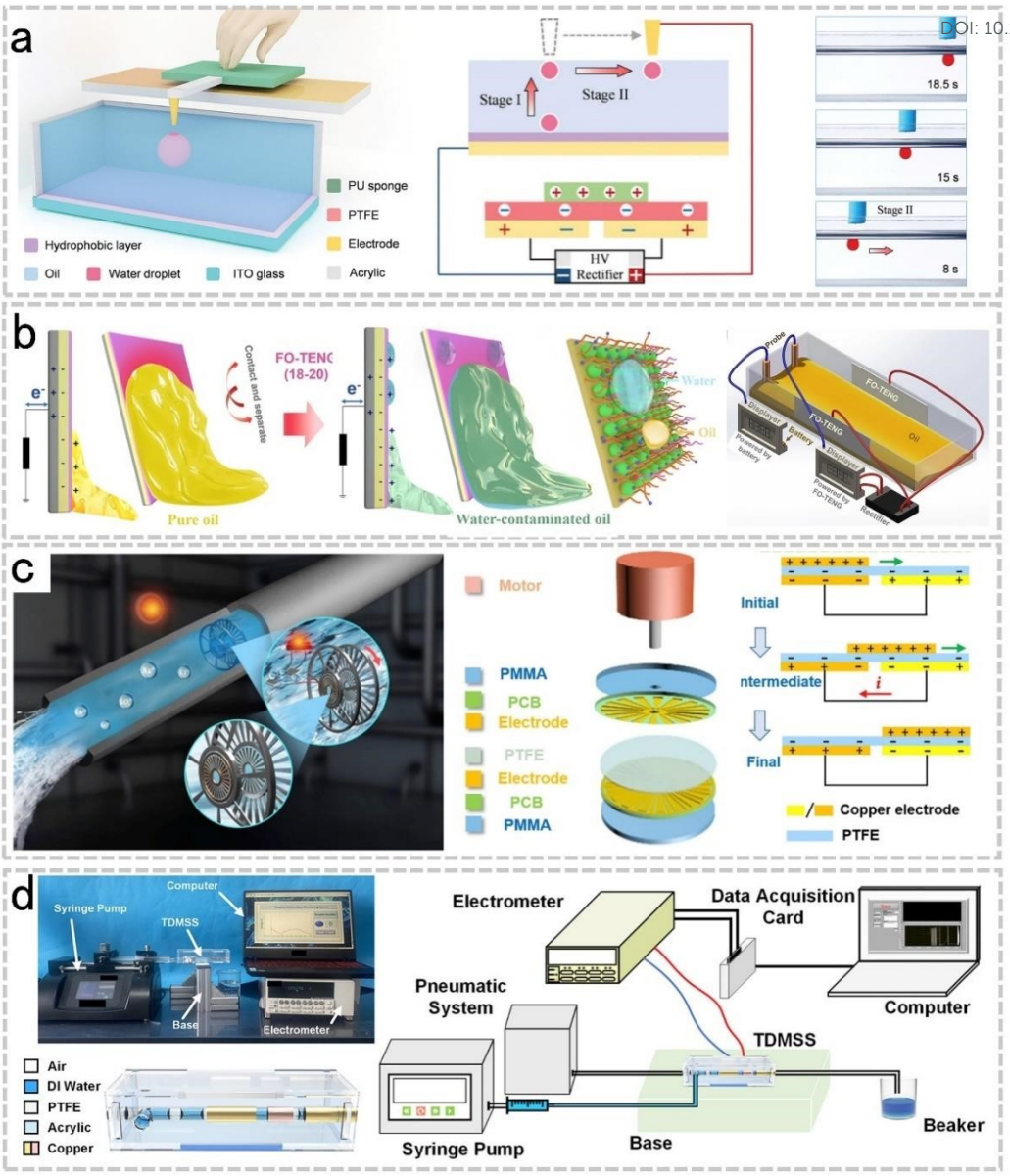

Fig. 15 The application of F-TENG in manufacturing fluid and industry. (a) A highly efficient droplet manipulation system via human-motion-induced direct charge injection.[188] (b) Detection of worn debris and water contamination in oils based on TENG.[191] (c) A self-powered on-line ion concentration monitor in water transportation based on TENG.[192] (d) A system for nonintrusion monitoring of droplet motion state.[195]

5.6 Microfluidics

Microfluidics is a technology that utilizes channels at the micrometer scale to control minute liquid volumes, commonly employed in areas such as chemical reactions, microanalysis, and microelectronics. It is characterized by high sensitivity, low cost, and short analysis times, making it a highly promising technology.[196] Within a microfluidics chip, numerous small-scale microfluidic channels enable small-volume, selective, rapid, and environmentally friendly microfluidic interactions and chemical reactions.[197] Due to the self-powering, high voltage, and low current

characteristics of TENG, which meet the requirements of electrowetting-on-dielectric (EWOD) devices, researchers commonly use TENG and EWOD as a basis for developing wearable microfluidic systems. Li *et al.*[198] presented an innovative approach for fabricating a self-powered and accurate microfluidic manipulation system, enhancing the manipulation capacity of microfluidics from 20 nL to 1.4 mL. As illustrated in Fig. 16a, the TENG-MF (triboelectric nanogenerator-based microfluidics) system comprises two parts: the TENG serving as an external power source and the MF device for manipulating liquids. To avoid breakdown discharge between the electrodes, Li placed Kapton film on the electrode array, utilized hydrophobic PTFE as the friction layer in contact with the liquid, and selected PC and FEP as the friction layers for the TENG to ensure stable voltage output. The TENG-MF system proposed by Li *et al.* can precisely control the movement of microfluidics along arbitrary trajectories in two-dimensional space. This manipulation is achieved based on the electrostatic force generated by TENG and is influenced by surface hydrophobicity, electrode area, microfluidic dimensions, and TENG operational parameters. Compared to traditional devices, TENG-MF can perform more complex microfluidic operations, demonstrating broad prospects. Wang *et al.*[199] investigated the physical behavior during TENG-driven EWOD processes, demonstrating a strategy for manipulating liquid wetting through mechanically stimulating EWOD with high-pressure output. By discussing the adaptability of different liquids, contact angles, and the impact of output voltage, Wang suggests that TENG-driven EWOD processes possess characteristics of portability, safety, and low cost. They can simplify the manipulation of liquid-solid interface wetting properties and exhibit universal applicability across various liquid systems, including deionized water and ionic liquids, providing valuable insights for many self-powered microfluidic applications.

Due to various factors currently causing interference in TENG output within practical application environments and issues such as impedance mismatch between devices and testing instruments,[200–202] researchers have begun utilizing the number of peaks to quantify the stability of triboelectric sensor performance.[203] Ge *et al.*[204] proposed the idea of utilizing liquid flow in microfluidic channels to generate output signals. They introduced a flexible microfluidic triboelectric sensor (FMTS) and used the number of peaks to quantify functions such as angle sensing. As illustrated in Fig. 16b, the FMTS system, based on the quantified voltage peaks generated by frictional triboelectric and induced charges between liquid flow, microchannels, and interdigitated ITO electrodes, can also be applied to gesture recognition and information encoding. The FMTS structure consists of a flexible PDMS substrate with microfluidic channels, two chambers, interdigitated ITO electrodes, and a thin PDMS film serving as the friction layer. This structure can precisely sense the force above the fluid chamber, where varying degrees of force lead to corresponding liquid-solid contacts, generating matched electrical signals. Through machine learning and a convolutional neural networks (CNN) training model, data sets can be classified and recognized with an accuracy of 98.8%. As shown in Fig. 16c, Kanik *et al.*[205] reported a method based on the integration of hollow fibers with microfluidics for triboelectric power generation, employing the iterative thermal size reduction (TSR) technique. This method can be widely applied in biochemical experiments that require repeated measurements and statistical analysis. The F-

View Article Online
DOI: 10.1039/D4EE00482E

TENG system designed by Kanik *et al.* can generate up to 1 V open-circuit voltage and 120 μA short-circuit current, with a maximum instantaneous power output of 47 μW. It can be applied in areas such as on-chip cancer diagnoses[206] and chemically modified,[207] showcasing significant potential.

Microfluidic sensors, as widely deployed analytical components in many industrial and commercial fields, have the capability to monitor and control flow rates.[208] Chen *et al.*[209] reported a triboelectric nanosensor capable of detecting friction-induced charges at the liquid-solid interface, specifically designed for microfluidics. This sensor can be employed for monitoring fluid flow rates and characterizing chemical synthesis. As shown in Fig. 16d, researchers selected PTFE with hydrophobic and electret properties as the tribo-layer to enhance the PE substrate. In liquid-TMS and gas-TMS, charging occurs through contact with the surface using liquid droplets and bubbles, respectively. Specifically, in the case of gas-TMS, internally filled water shields the electrodes from electrostatic induction by forming a stable electric double layer (EDL) on the water-PTFE interface until the appearance of bubbles disrupts the screen effect. When the bubble leaves the PTFE layer, the EDL is reorganized, and electrons move from the ground to the electrode to counterbalance the positive charge on the electrode. Different fluid flow rates result in distinct signal output frequencies. The quantity of fluid can be calculated based on the intervals or the number of peaks generated by liquid droplets. Therefore, this sensor has applications in medical and industrial fields, such as monitoring intravenous fluid delivery and gas flow rates, enabling precise control in microfluidics.

View Article Online
DOI: 10.1039/D4EE00482E

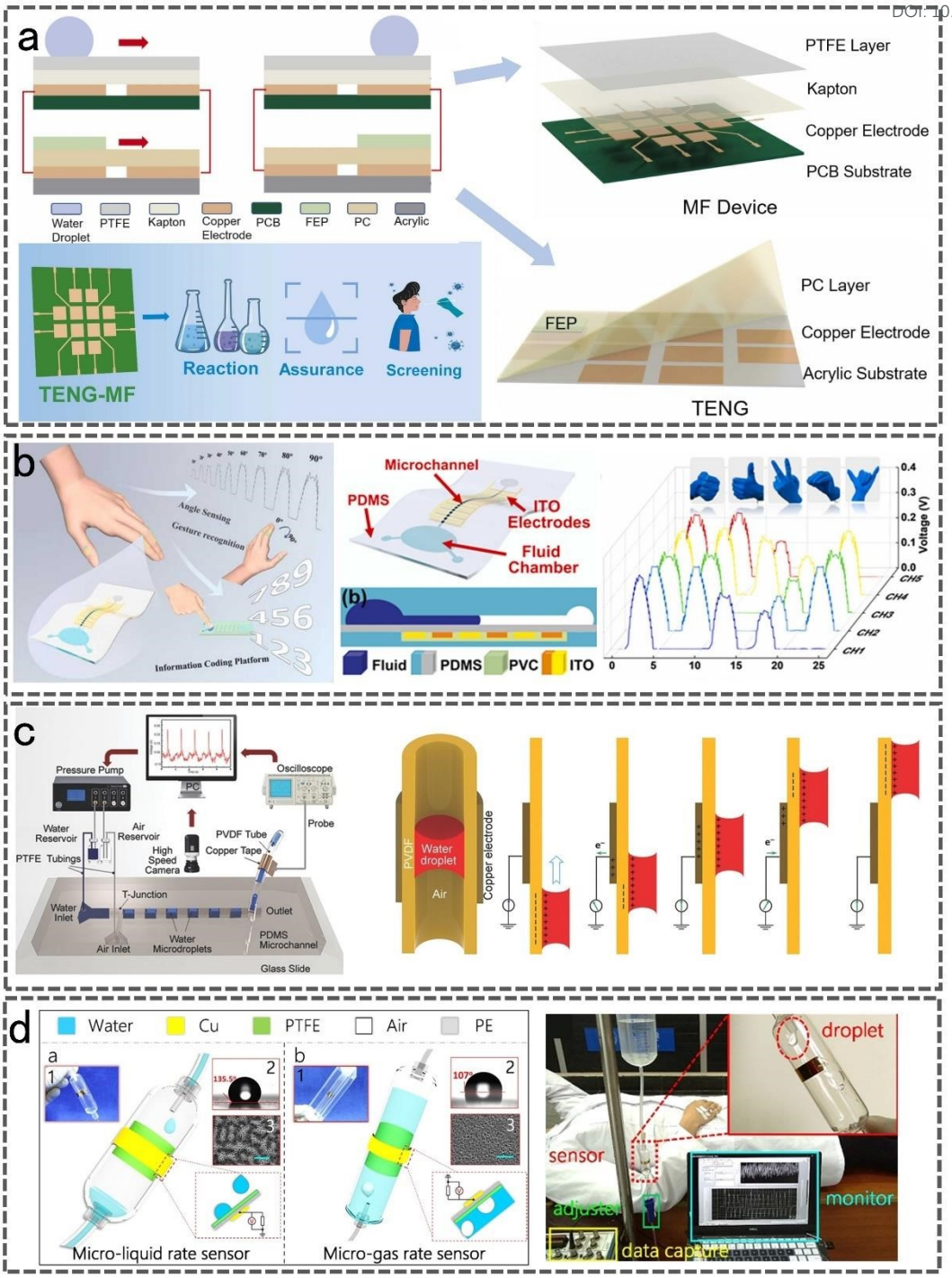

Fig. 16 The application of F-TENG in microfluidics. (a) A self-powered and precise microfluidic manipulation system.[198] (b) A flexible microfluidic triboelectric sensor can be used for gesture recognition and information encoding.[204] (c) An integrated system of microfluidics chip and triboelectric device based on PVDF hollow fibers.[205] (d) A self-powered triboelectric fluidic sensor for microfluidics.[209]

View Article Online
DOI: 10.1039/D4EE00482E

5.7 Medical and life science

With the advancement of medical and life sciences, there is a continuous need to improve treatment methods, drug delivery, and sterilization to enhance the efficacy of drugs and reduce side effects.[210,211] Drug delivery is a scientific and technological discipline focused on effectively delivering drugs at ideal concentrations into the body to achieve therapeutic goals. To precisely target cells causing diseases with drugs, microfluidics systems can be considered as a means to achieve this goal.[212] Due to the portability and flexibility of microfluidics systems, with the capability for high throughput, TENG can be employed as a power source and driving force for microfluidics-based drug delivery.[210] As shown in Fig. 17a, Nie *et al.*[213] designed a self-powered microfluidic transport system employing the electrowetting technique and TENG. Four droplets were utilized plus a tray to compose a mini vehicle, driven by the Coulomb force provided by the electrostatic field generated by TENG. The maximum payload reaches 500 mg, with a controllable speed of up to 1 m s^{-1}, and the minimum volume of liquid droplets can reach 70–80 nL. This microfluidic transport system can achieve manual control without the need for any detectors or control circuits, enabling human-machine interaction. It finds applications in areas such as inkjet printing and drug delivery. In the biomedical field, the innovation in drug delivery technology not only drives advancements in therapeutic methods but also provides crucial support for the development of droplet sensors, expanding the frontiers of biological monitoring and treatment. Hu *et al.*[79] fabricated a superhydrophobic liquid–solid contact TENG with flexibility, self-cleaning properties, self-adhesiveness, and high sensitivity. Due to the highly hydrophobic nature of the friction layer, liquid droplets can fully contact and separate from the friction layer, and the peak currents generated by different droplets vary.[214] If the superhydrophobic TENG is installed on a drainage bottle, it can realize the monitoring of drainage operations using a drainage bottle droplet sensor. Additionally, when biological fluids such as tissue fluid, pus, or blood pass through the drainage bottle droplet sensor, they can also be monitored.

Achieving precise, harmless, and efficient delivery of biomolecules into cells and sterilization has always been a challenge.[215] Due to its high voltage output and the ability to harvest mechanical energy from human activities and the surrounding environment, TENGs can enhance energy for treatment without the need for external power sources. Electroporation, a mature application in multiple biomedical fields, can be used for electrotransformation, inactivation of microorganisms, and extracellular drug delivery.[215,216] To efficiently achieve immediate and sustainable sterilization of microorganisms in natural river water, Tian *et al.*[217] proposed a highly efficient water sterilization system driven by wave energy. The system consists of a TENG and electrodes integrated with Ag-nanoparticles and ZnO-nanowires. As shown in Fig. 17b, when driven by waves, the TENG provides an electrical field (EF) to induce electroporation and charging of the electrodes. Electroporation causes reversible structural changes on the outer surface, leading to the formation of pores and ruptures in the bacterial membrane, directly causing bacterial death.[216] When the wave stops driving, the electrical field (EF) disappears. At this point, sustained intracellular reactive oxygen species (ROS) are induced for additional sterilization. As seen in Fig. 17b, the antibacterial capability is

maintained even after the withdrawal of the electrical field (EF). Chen *et al.*[218] proposed a system that harnesses wind energy for self-powered plasma sterilization. They quantitatively studied the generation of active substances with different sterilization capabilities. As shown in Fig. 17c, the high-voltage characteristics of TENG were utilized as the excitation power source for a bubble-based plasma generator. This setup is used to stimulate plasma discharge, and argon gas is chosen to provide the gas conditions for plasma discharge. Before and after sterilization, observable damage to the cell membrane, leakage of cellular contents, uneven cytoplasm, and noticeable gaps within cells can be observed, reducing the survival rate of bacterial strains. In addition, Ding *et al.*[219] proposed a low-cost manual water disinfection system based on disk-TENG, and Huo *et al.*[220] established a novel oxidation-assisted electroporation mechanism propelled by supercoiling-mediated rotational-TENG. These various methods for achieving sterilization contribute to the development of medical and life sciences, providing new solutions for electroporation-based sterilization.

With the rapid expansion of the industrial sector, air pollution resulting from excessive emissions from factories has become an escalating concern.[221] A significant proportion of suspended particulate matter (PM) constitutes a primary cause of air pollution.[222] Conventional N95 masks filter particles through electrostatic interactions, offering protective functions.[223] However, this type of mask exhibits poor stability in humid environments. To address this issue, Yang *et al.*[224] developed a straightforward, self-powered air filtration face mask based on TENG. The mask incorporates high filtration efficiency and long-term stable charges with polyacrylonitrile (PAN) nanofiber/polystyrene (PS) microfiber. As illustrated in Fig. 17d, exhaled airflow promotes repeated contact and separation of fibers, creating a fluttering model that continuously supplies electric charges for electrostatic particulate matter captured by the mask, resulting in excellent filtration performance. At airflow rates of 32 L min^{-1} and 85 L min^{-1}, the fiber membrane achieved particle filtration efficiencies for $PM_{0.3}$ particles of 99.98% and 97.53%, respectively, while maintaining relatively low-pressure differentials of 35 Pa and 85 Pa, respectively. The research integrates TENG with wearable devices, enabling long-term air filtration and control over fluids, offering significant potential in industrial production and environmental protection, among other fields.

View Article Online
DOI: 10.1039/D4EE00482E

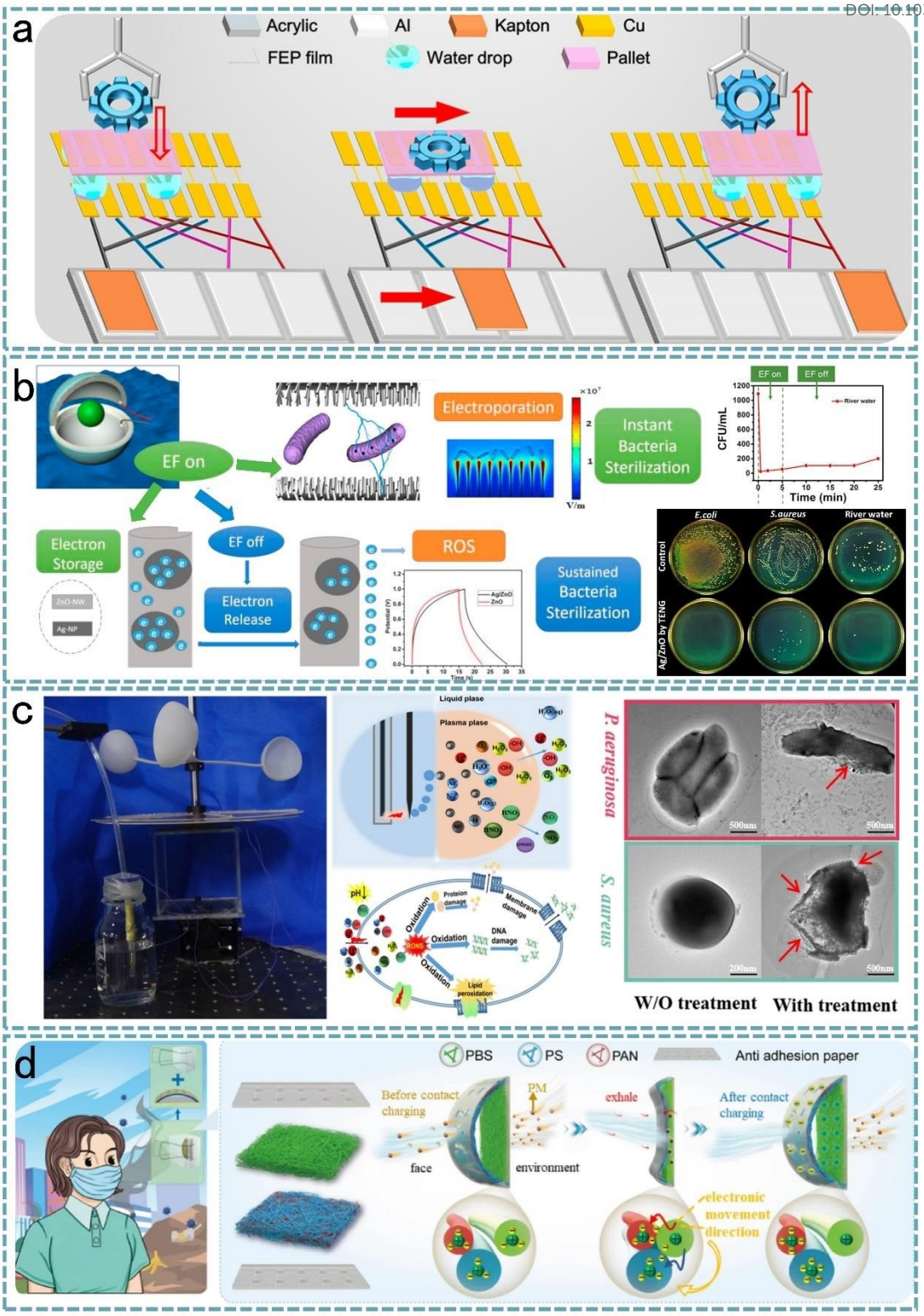

Fig. 17 The application of F-TENG in medical and life science includes. (a) A self-powered microfluidic transport system suitable for drug delivery.[213] (b) A self-powered sterilization system driven by wave energy collected by TENG.[217] (c) A self-powered plasma sterilization system

driven by wind energy collected by TENG.[218] (d) Achieving high filtration efficiency for particles: a self-powered $PM_{0.3}$ filter utilizes electrostatic capturing.[224]

6. Summary and perspectives

Leveraging the five key characteristics of F-TENG, namely energetical independence, shape adaptability, fluid properties, environmental extensiveness, and mechanical durability, F-TENG have the capability to opt for a broader range of materials and more diverse structural designs. This enables its application in a more diverse array of environments, such as alongside high-speed roads, unmanned forests, factory pipelines, and more. It can serve multiple functions, including energy harvesting, environmental monitoring, industrial sensing, microfluidics and drug delivery, etc. In the era of the 5G and Internet of Things, it holds immense potential.

This paper systematically summarizes the fundamental working principles and operational modes of current F-TENG. It discusses the impacts of environmental factors, fluid properties, contact materials, and atmospheres on the output performance of F-TENG. It also analyzes the output performance and structural characteristics of several typical F-TENG structures. Finally, it concludes by summarizing the progress in the applications of F-TENG in the fields of agriculture, the Internet of Things, transportation, environmental protection, and fluid control, providing insights into the development and utilization of F-TENG.

With the advancement of communications technology and the Internet of Things, people's lifestyles are poised for transformation. F-TENG, as a nascent technology for energy harvesting and self-powered sensors, has demonstrated significant long-term potential. Nevertheless, researchers need to undertake more comprehensive investigations in numerous domains. The further development of F-TENG necessitates consideration of the following aspects：

1. While there have been initial strides in comprehending the charge transfer mechanisms at the liquid-solid interface, exemplified by models like the spin-selected electron transfer model[32] and EDL model,[30] the surface charging-releasing mechanisms of gases still pose a challenge, demanding additional research. Additionally, the developments of the triboelectric series[24] of liquid and gas materials by standard measurement are pivotal for advancing the F-TENG field, warranting further investigation.

2. To surmount the inherent material and structural constraints of F-TENG, such as the necessity for hydrophobic materials in liquid-TENG, flexibility requirements for flutter-TENG, and considerations of aerodynamics for gas-TENG, the development of structures with enhanced triboelectric capabilities becomes imperative. Simultaneously, there is a pressing need to devise device structures that not only maximize energy conversion efficiency but also enhance the lifespan of these technologies. Addressing these critical aspects will undoubtedly make substantial contributions to elevating the overall performance and versatility of F-TENG in real-world applications.

3. Currently, the primary means of enhancing output in the TENGs field involve surface modification to increase surface charge density, charge excitation, or power management circuits. Due to the unique mechanical durability and shape adaptability characteristics of F-TENG, it can operate for a longer duration compared to S-TENG, but its output efficiency is lower than that of S-TENG. Therefore, additional measures in materials and structures are imperative to boost the efficiency of F-TENG, ensuring it becomes more competitive and applicable across various domains.

4. Due to the self-powered nature and extensive energy sources of F-TENG, it holds significant importance in the foundational applications of the Internet of Things blueprint for the future world. Moreover, as TENGs are widely employed for harvesting low-frequency mechanical energy in the environment, the generated signals exhibit strong characteristics that can be statistically analyzed through means such as machine learning and artificial intelligence,[225] enabling predictions about the environmental conditions. Additionally, some F-TENG units utilized on pipe walls or within structures are isolated from external environmental conditions to some extent. This isolation makes them advantageous in applications that require stable, autonomous energy collection, such as gas flow sensors and in-body monitoring.

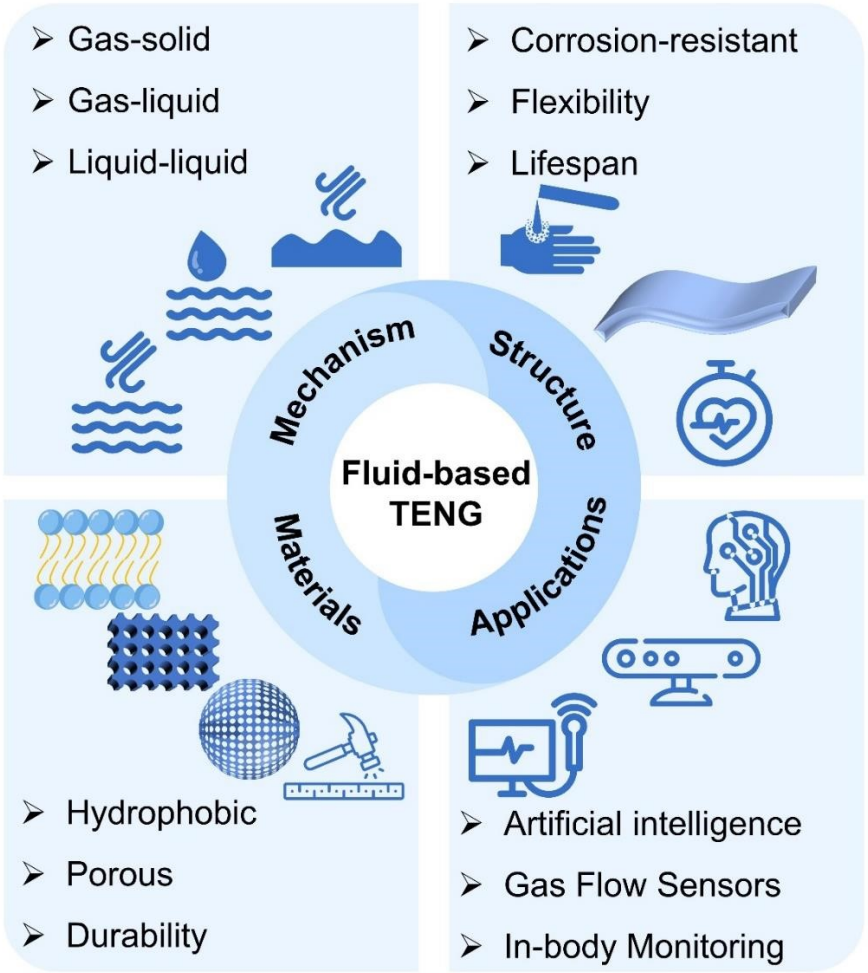

Fig. 18 Summary and perspectives of F-TENG.

In summary, F-TENG proves to be highly adaptable to fluid environments, capable of generating electricity in liquid flow, offering infinite possibilities for energy harvesting in liquids such as water flow. Additionally, F-TENG exhibits greater flexibility in material selection because the fluidic nature allows the TENG to adapt to minor changes in surface shape during operation. Finally, F-TENG holds potential for application in large-scale fluid environments such as fluid pipelines and rivers, showcasing its ability to play a role in large-scale energy harvesting applications. Fluid, as a perpetually moving substance with inherent energy, emerges as an immensely promising energy source. With the ongoing progress in nanomaterials and technologies, coupled with the evolving understanding of gas-solid, liquid-solid, liquid-liquid and even gas-liquid contact electrification, the practical application of F-TENG holds a bright future.

Conflicts of interest

There are no conflicts of interest to declare.

Acknowledgements

We thank the support from the Fundamental Research Funds for the Central Universities (YJ202293), and the National Natural Science Foundation of China-Outstanding Yourth Overseas Project (0000007401064).

Reference

1 Z. L. Wang, *Nano Energy*, 2019, **58**, 669–672.

2 Z. L. Wang, *Nano Energy*, 2018, **54**, 477–483.

3 Z. L. Wang, T. Jiang and L. Xu, *Nano Energy*, 2017, **39**, 9–23.

4 T. Jiang, H. Pang, J. An, P. Lu, Y. Feng, X. Liang, W. Zhong and Z. L. Wang, *Adv. Energy Mater.*, 2020, **10**, 2000064.

5 Z.-H. Lin, G. Cheng, S. Lee, K. C. Pradel and Z. L. Wang, *Adv. Mater.*, 2014, **26**, 4690–4696.

6 Z.-H. Lin, G. Cheng, L. Lin, S. Lee and Z. L. Wang, *Angew. Chem. Int. Ed.*, 2013, **52**, 12545–12549.

7 Z. L. Wang, *Nature*, 2017, **542**, 159–160.

8 G. Zhu, Y. Su, P. Bai, J. Chen, Q. Jing, W. Yang and Z. L. Wang, *ACS Nano*, 2014, **8**, 6031–6037.

9 J. Chen, Y. Huang, N. Zhang, H. Zou, R. Liu, C. Tao, X. Fan and Z. L. Wang, *Nat. Energy*, 2016, **1**, 16138.

10 B. Chen, Y. Yang and Z. L. Wang, *Adv. Energy Mater.*, 2018, **8**, 1702649.

11 Y. Yang, G. Zhu, H. Zhang, J. Chen, X. Zhong, Z.-H. Lin, Y. Su, P. Bai, X. Wen and Z. L. Wang, *ACS Nano*, 2013, **7**, 9461–9468.

12 Y. Xie, S. Wang, L. Lin, Q. Jing, Z.-H. Lin, S. Niu, Z. Wu and Z. L. Wang, *ACS Nano*, 2013, **7**, 7119–7125.

13 R. Xia, R. Zhang, Y. Jie, W. Zhao, X. Cao and Z. Wang, *Nano Energy*, 2022, **92**, 106685.

14 B. Dai, G. M. Biesold, M. Zhang, H. Zou, Y. Ding, Z. L. Wang and Z. Lin, *Chem. Soc. Rev.*, 2021, **50**, 13646–13691.

15 Z. Qu, M. Huang, C. Chen, Y. An, H. Liu, Q. Zhang, X. Wang, Y. Liu, W. Yin and X. Li, *Adv. Funct. Mater.*, 2022, **32**, 2202048.

16 B. Chai, K. Shi, H. Zou, P. Jiang, Z. Wu and X. Huang, *Nano Energy*, 2022, **91**, 106668.

17 Z. Wu, B. Zhang, H. Zou, Z. Lin, G. Liu and Z. L. Wang, *Adv. Energy Mater.*, 2019, **9**, 1901124.

18 F.-R. Fan, Z.-Q. Tian and Z. Lin Wang, *Nano Energy*, 2012, **1**, 328–334.

19 P. A. Østergaard, N. Duic, Y. Noorollahi, H. Mikulcic and S. Kalogirou, *Renew. Energy*, 2020, **146**, 2430–2437.

20 P. Wang, L. Pan, J. Wang, M. Xu, G. Dai, H. Zou, K. Dong and Z. L. Wang, *ACS Nano*, 2018, **12**, 9433–9440.

21 Z. Lin, B. Zhang, H. Guo, Z. Wu, H. Zou, J. Yang and Z. L. Wang, *Nano Energy*, 2019, **64**, 103908.

22 P. Wang, R. Liu, W. Ding, P. Zhang, L. Pan, G. Dai, H. Zou, K. Dong, C. Xu and Z. L. Wang, *Adv. Funct. Mater.*, 2018, **28**, 1705808.

23 Q.-T. Nguyen and K.-K. K. Ahn, *Int. J. Precis. Eng. Manuf.-Green Technol.*, 2021, **8**, 1043–1060.

24 H. Zou, Y. Zhang, L. Guo, P. Wang, X. He, G. Dai, H. Zheng, C. Chen, A. C. Wang, C. Xu and Z. L. Wang, *Nat. Commun.*, 2019, **10**, 1427.

25 C. Xu, Y. Zi, A. C. Wang, H. Zou, Y. Dai, X. He, P. Wang, Y.-C. Wang, P. Feng, D. Li and Z. L. Wang, *Adv. Mater.*, 2018, **30**, 1706790.

26 C. Xu, A. C. Wang, H. Zou, B. Zhang, C. Zhang, Y. Zi, L. Pan, P. Wang, P. Feng, Z. Lin and Z. L. Wang, *Adv. Mater.*, 2018, **30**, 1803968.

27 Z. L. Wang and A. C. Wang, *Mater. Today*, 2019, **30**, 34–51.

28 H. Zou, L. Guo, H. Xue, Y. Zhang, X. Shen, X. Liu, P. Wang, X. He, G. Dai, P. Jiang, H. Zheng, B. Zhang, C. Xu and Z. L. Wang, *Nat. Commun.*, 2020, **11**, 2093.

29 Z. L. Wang, *Rep. Prog. Phys.*, 2021, **84**, 096502.

30 S. Lin, X. Chen and Z. L. Wang, *Chem. Rev.*, 2022, **122**, 5209–5232.

31 S. Lin, L. Xu, A. Chi Wang and Z. L. Wang, *Nat. Commun.*, 2020, **11**, 399.

32 S. Lin, L. Zhu, Z. Tang and Z. L. Wang, *Nat. Commun.*, 2022, **13**, 5230.

33 J. Nie, Z. Ren, L. Xu, S. Lin, F. Zhan, X. Chen and Z. L. Wang, *Adv. Mater.*, 2020, **32**, 1905696.

34 C. Xu, B. Zhang, A. C. Wang, H. Zou, G. Liu, W. Ding, C. Wu, M. Ma, P. Feng, Z. Lin and Z. L. Wang, *ACS Nano*, 2019, **13**, 2034–2041.

35 C. Xu, B. Zhang, A. C. Wang, W. Cai, Y. Zi, P. Feng and Z. L. Wang, *Adv. Funct. Mater.*, 2019, **29**, 1903142.

36 S. Lin, L. Xu, L. Zhu, X. Chen and Z. L. Wang, *Adv. Mater.*, 2019, **31**, 1901418.

37 S. Lin, L. Xu, C. Xu, X. Chen, A. C. Wang, B. Zhang, P. Lin, Y. Yang, H. Zhao and Z. L. Wang, *Adv. Mater.*, 2019, **31**, 1808197.

38 Z. L. Wang, *Adv. Energy Mater.*, 2020, **10**, 2000137.

39 R. Fu, X. Shen and D. J. Lacks, *J. Phys. Chem. C*, 2017, **121**, 12345–12349.

40 Osc. Knoblauch, 1902, **39U**, 225–244.

41 L. S. McCarty, A. Winkleman and G. M. Whitesides, *Angew. Chem. Int. Ed.*, 2007, **46**, 206–209.

42 Z. Stojek, in *Electroanalytical Methods: Guide to Experiments and Applications*, eds. F. Scholz, A. M. Bond, R. G. Compton, D. A. Fiedler, G. Inzelt, H. Kahlert, Š. Komorsky-Lovrić, H. Lohse, M. Lovrić, F. Marken, A. Neudeck, U. Retter, F. Scholz and Z. Stojek, Springer, Berlin, Heidelberg, 2010, pp. 3–9.

43 L. Sun, Z. Wang, C. Li, W. Tang and Z. Wang, *Nanoenergy Adv.*, 2023, **3**, 1–11.

44 K. Shi, B. Chai, H. Zou, Z. Wen, M. He, J. Chen, P. Jiang and X. Huang, *Adv. Funct. Mater.*, 2023, **n/a**, 2307678.

45 Z.-H. Lin, G. Cheng, L. Lin, S. Lee and Z. L. Wang, *Angew. Chem. Int. Ed.*, 2013, **52**, 12545–12549.

46 J. Nie, Z. Wang, Z. Ren, S. Li, X. Chen and Z. Lin Wang, *Nat. Commun.*, 2019, **10**, 2264.

47 C. Ye, D. Liu, P. Chen, L. N. Y. Cao, X. Li, T. Jiang and Z. L. Wang, *Adv. Mater.*, 2023, **35**, 2209713.

48 J.-W. Lee and W. Hwang, *Nano Energy*, 2018, **52**, 315–322.

49 C. Xu, X. Fu, C. Li, G. Liu, Y. Gao, Y. Qi, T. Bu, Y. Chen, Z. L. Wang and C. Zhang, *Microsyst. Nanoeng.*, 2022, **8**, 30.

50 D. Yoo, S.-C. Park, S. Lee, J.-Y. Sim, I. Song, D. Choi, H. Lim and D. S. Kim, *Nano Energy*, 2019, **57**, 424–431.

51 A. C. Wang, B. Zhang, C. Xu, H. Zou, Z. Lin and Z. L. Wang, *Adv. Funct. Mater.*, 2020, **30**, 1909384.

52 Y. S. Zhou, S. Li, S. Niu and Z. L. Wang, *Nano Res.*, 2016, **9**, 3705–3713.

53 D. Wang, D. Zhang, J. Guo, Y. Hu, Y. Yang, T. Sun, H. Zhang and X. Liu, *Nano Energy*, 2021, **89**, 106410.

54 L. Yang, J. Yu, Y. Guo, S. Chen, K. Tan and S. Li, *Adv. Funct. Mater.*, **n/a**, 2302147.

55 W. Xu, H. Zheng, Y. Liu, X. Zhou, C. Zhang, Y. Song, X. Deng, M. Leung, Z. Yang, R. X. Xu, Z. L. Wang, X. C. Zeng and Z. Wang, *Nature*, 2020, **578**, 392–396.

56 X. Li, L. Xu, P. Lin, X. Yang, H. Wang, H. Qin and Z. L. Wang, *Energy Environ. Sci.*, 2023, **16**, 3040–3052.

57 T. Zhan, H. Zou, H. Zhang, P. He, Z. Liu, J. Chen, M. He, Y. Zhang and Z. L. Wang, *Nano Energy*, 2023, **111**, 108419.

58 S. Yong, J. Wang, L. Yang, H. Wang, H. Luo, R. Liao and Z. L. Wang, *Adv. Energy Mater.*, 2021, **11**, 2101194.

59 S.-H. Chung, J. Son, K. Cha, M. Choi, H. Jung, M.-K. Kim, J. Hong and S. Lee, *Nano Energy*, 2023, **111**, 108389.

60 T. Huang, Y. Long, Z. Dong, Q. Hua, J. Niu, X. Dai, J. Wang, J. Xiao, J. Zhai and W. Hu, *Adv. Sci.*, 2022, **9**, 2204519.

61 I. Gonçalves, C. Rodrigues and J. Ventura, *Adv. Energy Mater.*, **n/a**, 2302627.

62 Y. Dong, M. Feng, J. Cheng, S. Chang, D. Wang and W. Lu, *Nano Energy*,

View Article Online
DOI: 10.1039/D4EE00482E

2024, **119**, 109083.

63 Y. Li, H. Deng, H. Wu, Y. Luo, Y. Deng, H. Yuan, Z. Cui, J. Tang, J. Xiong, X. Zhang and S. Xiao, *Adv. Sci.*, **n/a**, 2307382.

64 T. Mudgal, M. Tiwari and D. Bharti, *Nano Energy*, 2024, **123**, 109388.

65 J. Xiong, G. Thangavel, J. Wang, X. Zhou and P. S. Lee, *Sci. Adv.*, 2020, **6**, eabb4246.

66 F. Wang, P. Yang, X. Tao, Y. Shi, S. Li, Z. Liu, X. Chen and Z. L. Wang, *ACS Nano*, 2021, **15**, 18206–18213.

67 Y. Lu, L. Jiang, Y. Yu, D. Wang, W. Sun, Y. Liu, J. Yu, J. Zhang, K. Wang, H. Hu, X. Wang, Q. Ma and X. Wang, *Nat. Commun.*, 2022, **13**, 5316.

68 Y. Liu, W. Liu, Z. Wang, W. He, Q. Tang, Y. Xi, X. Wang, H. Guo and C. Hu, *Nat. Commun.*, 2020, **11**, 1599.

69 J. Falnes, *Mar. Struct.*, 2007, **20**, 185–201.

70 S. L. Zhang, M. Xu, C. Zhang, Y.-C. Wang, H. Zou, X. He, Z. Wang and Z. L. Wang, *Nano Energy*, 2018, **48**, 421–429.

71 C. Zhang, W. Yuan, B. Zhang, J. Yang, Y. Hu, L. He, X. Zhao, X. Li, Z. L. Wang and J. Wang, *Small*, **n/a**, 2304412.

72 S. Wang, P. Xu, X. Wang, J. Zheng, X. Liu, J. Liu, T. Chen, H. Wang, G. Xie, J. Tao and M. Xu, *Nano Energy*, 2022, **97**, 107210.

73 X. Cui, H. Zhang, S. Cao, Z. Yuan, J. Ding and S. Sang, *Nano Energy*, 2018, **52**, 71–77.

74 J. Wang, Z. Wu, L. Pan, R. Gao, B. Zhang, L. Yang, H. Guo, R. Liao and Z. L. Wang, *ACS Nano*, 2019, **13**, 2587–2598.

75 J. Wang, Z. Wu, L. Pan, R. Gao, B. Zhang, L. Yang, H. Guo, R. Liao and Z. L. Wang, *ACS Nano*, 2019, acsnano.8b09642.

76 R. Gross, M. Leach and A. Bauen, *Environ. Int.*, 2003, **29**, 105–122.

77 Y. Zhong, H. Zhao, Y. Guo, P. Rui, S. Shi, W. Zhang, Y. Liao, P. Wang and Z. L. Wang, *Adv. Mater. Technol.*, 2019, **4**, 1900741.

78 Y. Liu, M. Zhu, D. Nan, X. Li, Y. Wang, W. Su, Z. L. Wang and T. Cheng, *Adv. Sustain. Syst.*, 2023, **7**, 2200367.

79 S. Hu, Z. Shi, R. Zheng, W. Ye, X. Gao, W. Zhao and G. Yang, *ACS Appl. Mater. Interfaces*, 2020, **12**, 40021–40030.

80 J. Sun, L. Zhang, Y. Zhou, Z. Li, A. Libanori, Q. Tang, Y. Huang, C. Hu, H. Guo, Y. Peng and J. Chen, *Mater. Today*, 2022, **58**, 41–47.

81 X. Yu, S. Fu, X. Zuo, J. Zeng, C. Shan, W. He, W. Li and C. Hu, *Adv. Funct. Mater.*, 2022, **32**, 2207498.

82 Z. Lin, B. Zhang, H. Zou, Z. Wu, H. Guo, Y. Zhang, J. Yang and Z. L. Wang, *Nano Energy*, 2020, **68**, 104378.

83 W. He, C. Shan, S. Fu, H. Wu, J. Wang, Q. Mu, G. Li and C. Hu, *Adv. Mater.*, 2023, **35**, 2209657.

84 S. Fu, H. Wu, C. Shan, K. Li, W. He, Q. Li, X. Yu, S. Du, G. Li and C. Hu, *Nano Energy*, 2023, **116**, 108850.

85 L. Long, W. Liu, Z. Wang, W. He, G. Li, Q. Tang, H. Guo, X. Pu, Y. Liu and C. Hu, *Nat. Commun.*, 2021, **12**, 4689.

86 R. D. Blevins, *Flow-induced vibration*, Van Nostrand Reinhold Co, New York, 1977.

87 M. Wu, C. Zhu, X. Liu, H. Wang, J. Si, M. Xu and J. Mi, *Mater. Today Energy*, 2024, **41**, 101529.

88 J. Son, S.-H. Chung, K. Cha, S. Kim, Z.-H. Lin, J. Hong, J. Chung and S. Lee, *Adv. Mater.*, 2023, **35**, 2300283.

89 K. Shi, B. Chai, H. Zou, D. Min, S. Li, P. Jiang and X. Huang, *Research*, , DOI:10.34133/2022/9862980.

90 Y. Zi, S. Niu, J. Wang, Z. Wen, W. Tang and Z. L. Wang, *Nat. Commun.*, 2015, **6**, 8376.

91 Y. Chen, B. Xie, J. Long, Y. Kuang, X. Chen, M. Hou, J. Gao, S. Zhou, B. Fan, Y. He, Y.-T. Zhang, C.-P. Wong, Z. Wang and N. Zhao, *Adv. Mater.*, 2021, **33**, 2104290.

92 H. Wu, N. Mendel, S. van der Ham, L. Shui, G. Zhou and F. Mugele, *Adv. Mater.*, 2020, **32**, 2001699.

93 W. Ma, P. Wang, B. Zhang, X. Li, Y. Gao, Z. Zhao, D. Liu, C. Li and J. Wang, *Adv. Energy Mater.*, **n/a**, 2304331.

94 H. Qin, L. Xu, F. Zhan and Z. L. Wang, *Nano Energy*, 2023, **116**, 108762.

95 L. Zhang, X. Li, Y. Zhang, Y. Feng, F. Zhou and D. Wang, *Nano Energy*, 2020, **78**, 105370.

96 L. Zhang, X. Li, Y. Zhang, Y. Feng, F. Zhou and D. Wang, *Nano Energy*, 2020, **78**, 105370.

97 D. L. Vu, C. P. Vo, C. D. Le and K. K. Ahn, *Int. J. Energy Res.*, 2021, **45**, 8960–8970.

98 T. Kim, D. Y. Kim, J. Yun, B. Kim, S. H. Lee, D. Kim and S. Lee, *Nano Energy*, 2018, **52**, 95–104.

99 M. S. Miah, S. Al-Assaf, X. Yang and A. McMillan, *Chem. Eng. Sci.*, 2016, **143**, 226–239.

100 F. J. Galindo-Rosales, F. J. Rubio-Hernández and A. Sevilla, *J. Non-Newton. Fluid Mech.*, 2011, **166**, 321–325.

101 Y. Kim, J. Yun and D. Kim, *Nano Energy*, 2022, **98**, 107246.

102 D. Wang, D. Zhang, M. Tang, H. Zhang, T. Sun, C. Yang, R. Mao, K. Li and J. Wang, *Nano Energy*, 2022, **100**, 107509.

103 J. Chung, S.-H. Chung, Z.-H. Lin, Y. Jin, J. Hong and S. Lee, *Nano Energy*, 2021, **88**, 106292.

104 Y. Dong, S. Xu, C. Zhang, L. Zhang, D. Wang, Y. Xie, N. Luo, Y. Feng, N. Wang, M. Feng, X. Zhang, F. Zhou and Z. L. Wang, *Sci. Adv.*, 2022, **8**, eadd0464.

105 X. Wei, B. Wang, X. Cao, H. Zhou, Z. Wu and Z. L. Wang, *Nat. Food*, 2023, **4**, 721–732.

106 X. Wei, Z. Zhao, C. Zhang, W. Yuan, Z. Wu, J. Wang and Z. L. Wang, *ACS Nano*, 2021, **15**, 13200–13208.

107 J. Nie, Z. Ren, L. Xu, S. Lin, F. Zhan, X. Chen and Z. L. Wang, *Adv. Mater.*, 2020, **32**, 1905696.

108 Z. Zhao, X. Pu, C. Du, L. Li, C. Jiang, W. Hu and Z. L. Wang, *ACS Nano*, 2016, **10**, 1780–1787.

109 T. K. Phan, S. Wang, Y. Wang, H. Wang, X. Xiao, X. Pan, M. Xu and J. Mi, *Sensors*, 2020, **20**, 729.

110 Y. Wang, E. Yang, T. Chen, J. Wang, Z. Hu, J. Mi, X. Pan and M. Xu, *Nano Energy*, 2020, **78**, 105279.

111 W. Sun, Z. Ding, Z. Qin, F. Chu and Q. Han, *Nano Energy*, 2020, **70**, 104526.

112 Y. Zheng, T. Liu, J. Cui, Z. Zhang, C. Du, X. Gao, C. Chu and C. Xue,

View Article Online
DOI: 10.1039/D4EE00482E

Sens. Actuators Phys., 2023, **362**, 114613.

113 X. Xia, Z. Zhou, Y. Shang, Y. Yang and Y. Zi, *Nat. Commun.*, 2023, **14**, 1023.

114 X. Zhang, J. Hu, Q. Yang, H. Yang, H. Yang, Q. Li, X. Li, C. Hu, Y. Xi and Z. L. Wang, *Adv. Funct. Mater.*, 2021, **31**, 2106527.

115 Y. Wang, J. Wang, X. Xiao, S. Wang, P. T. Kien, J. Dong, J. Mi, X. Pan, H. Wang and M. Xu, *Nano Energy*, 2020, **73**, 104736.

116 Q. Zeng, Y. Wu, Q. Tang, W. Liu, J. Wu, Y. Zhang, G. Yin, H. Yang, S. Yuan, D. Tan, C. Hu and X. Wang, *Nano Energy*, 2020, **70**, 104524.

117 Q. Xu, Y. Lu, S. Zhao, N. Hu, Y. Jiang, H. Li, Y. Wang, H. Gao, Y. Li, M. Yuan, L. Chu, J. Li and Y. Xie, *Nano Energy*, 2021, **89**, 106382.

118 Y. Liu, J. Liu and L. Che, *Sensors*, 2021, **21**, 2951.

119 D. Wang, D. Zhang, X. Chen, H. Zhang, M. Tang and J. Wang, *Nano Energy*, 2022, **102**, 107711.

120 J. Cui, T. Liu, Y. Zheng, S. Bai, X. Li and C. Xue, *Energy Convers. Manag.*, 2023, **293**, 117456.

121 S. Xu, Y. Feng, Y. Liu, Z. Wu, Z. Zhang, M. Feng, S. Zhang, G. Sun and D. Wang, *Nano Energy*, 2021, **85**, 106023.

122 Y. Liu, W. Liu, Z. Wang, W. He, Q. Tang, Y. Xi, X. Wang, H. Guo and C. Hu, *Nat. Commun.*, 2020, **11**, 1599.

123 S. Lv, B. Yu, T. Huang, H. Yu, H. Wang, Q. Zhang and M. Zhu, *Nano Energy*, 2019, **55**, 463–469.

124 D. Liu, L. Zhou, S. Cui, Y. Gao, S. Li, Z. Zhao, Z. Yi, H. Zou, Y. Fan, J. Wang and Z. L. Wang, *Nat. Commun.*, 2022, **13**, 1–10.

125 Y. Zi, C. Wu, W. Ding and Z. L. Wang, *Adv. Funct. Mater.*, 2017, **27**, 1700049.

126 J. Wang, C. Wu, Y. Dai, Z. Zhao, A. Wang, T. Zhang and Z. L. Wang, *Nat. Commun.*, 2017, **8**, 88.

127 C. Xu, A. C. Wang, H. Zou, B. Zhang, C. Zhang, Y. Zi, L. Pan, P. Wang, P. Feng, Z. Lin and Z. L. Wang, *Adv. Mater.*, 2018, **30**, 1803968.

128 J. Zhang, Y. Gao, D. Liu, J.-S. Zhao and J. Wang, *Nat. Commun.*, 2023, **14**, 3218.

129 F. K. Shaikh, S. Karim, S. Zeadally and J. Nebhen, *IEEE Internet Things J.*, 2022, **9**, 23583–23598.

130 S. Dai, X. Li, C. Jiang, J. Ping and Y. Ying, *InfoMat*, 2023, **5**, e12391.

131 E. Costanzo, *J. Electrost.*, 2008, **66**, 417–420.

132 X. Li, J. Luo, K. Han, X. Shi, Z. Ren, Y. Xi, Y. Ying, J. Ping and Z. L. Wang, *Nat. Food*, 2022, **3**, 133–142.

133 Y. Zhong, Y. Guo, X. Wei, P. Rui, H. Du and P. Wang, *Nano Energy*, 2021, **89**, 106467.

134 J. Han, Y. Feng, P. Chen, X. Liang, H. Pang, T. Jiang and Z. L. Wang, *Adv. Funct. Mater.*, 2022, **32**, 2108580.

135 H. Guo, J. Chen, L. Wang, A. C. Wang, Y. Li, C. An, J.-H. He, C. Hu, V. K. S. Hsiao and Z. L. Wang, *Nat. Sustain.*, 2020, **4**, 147–153.

136 C. Yoon, D. Lim and C. Park, *Comput. Hum. Behav.*, 2020, **108**, 106309.

137 X. Liu and L. Xin, *Sci. Total Environ.*, 2023, **863**, 160810.

138 J. Xue, *Renew. Sustain. Energy Rev.*, 2017, **73**, 1–9.

139 R. Liu, J. Wang, T. Sun, M. Wang, C. Wu, H. Zou, T. Song, X. Zhang, S.-T. Lee, Z. L. Wang and B. Sun, *Nano Lett.*, 2017, **17**, 4240–4247.

140 R. Liu, Y. Liu, H. Zou, T. Song and B. Sun, *Nano Res.*, 2017, **10**, 1545–1559.

141 Q. Zhang, C. Jiang, X. Li, S. Dai, Y. Ying and J. Ping, *ACS Nano*, 2021, **15**, 12314–12323.

142 X. Zhang, Q. Yang, P. Ji, Z. Wu, Q. Li, H. Yang, X. Li, G. Zheng, Y. Xi and Z. L. Wang, *Nano Energy*, 2022, **99**, 107362.

143 K. Dong, Y.-C. Wang, J. Deng, Y. Dai, S. L. Zhang, H. Zou, B. Gu, B. Sun and Z. L. Wang, *ACS Nano*, 2017, **11**, 9490–9499.

144 K. Dong, J. Deng, Y. Zi, Y.-C. Wang, C. Xu, H. Zou, W. Ding, Y. Dai, B. Gu, B. Sun and Z. L. Wang, *Adv. Mater.*, 2017, **29**, 1702648.

145 K. Shi, H. Zou, B. Sun, P. Jiang, J. He and X. Huang, *Adv. Funct. Mater.*, 2020, **30**, 1904536.

146 K. Lu, C. Liu, H. Zou, Y. Wang, G. Wang, D. Li, K. Fan, W. Yang, L. Dong, R. Sha and D. Li, *PLOS ONE*, 2022, **17**, e0272632.

147 L. Atzori, A. Iera and G. Morabito, *Comput. Netw.*, 2010, **54**, 2787–2805.

View Article Online
DOI: 10.1039/D4EE00482E

148 X. Zhao, H. Askari and J. Chen, *Joule*, 2021, **5**, 1391–1431.

149 L. Zhou, D. Liu, J. Wang and Z. L. Wang, *Friction*, 2020, **8**, 481–506.

150 C. Liu, L. Fang, H. Zou, Y. Wang, J. Chi, L. Che, X. Zhou, Z. Wang, T. Wang, L. Dong, G. Wang and Z. L. Wang, *Extreme Mech. Lett.*, 2021, **42**, 101021.

151 L. Xu, L. Xu, J. Luo, Y. Yan, B.-E. Jia, X. Yang, Y. Gao and Z. L. Wang, *Adv. Energy Mater.*, 2020, **10**, 2001669.

152 D. Heo, J. Son, D. Kim, M. Song, H. Ryu, S. Kim, K. Choi, Z.-H. Lin, D. Kim, J. Hong and S. Lee, *Adv. Energy Mater.*, 2023, **13**, 2204239.

153 Y.-J. Park, Y. G. Ro, Y.-E. Shin, C. Park, S. Na, Y. Chang and H. Ko, *Adv. Sci.*, **n/a**, 2304598.

154 L. Zhao, X. Huang, Y. Zhang, Y. Zhu, J. Jia and C. Zhu, *Struct. Control Health Monit.*, 2020, **27**, e2538.

155 X. Tang, W. Hou, Q. Zheng, L. Fang, R. Zhu and L. Zheng, *Nano Energy*, 2022, **99**, 107412.

156 C. Han, J. Huo, Q. Gao, G. Su and H. Wang, *Remote Sens.*, 2020, **12**, 1045.

157 H. (Harrison) Jeong, Y. (Chris) Shen, J. (Paul) Jeong and T. (Tom) Oh, *Veh. Commun.*, 2021, **31**, 100349.

158 Y. Li, Z. Tian, X.-Z. Gao, H.-Y. Zhao, X. Li, Z. L. Wang, Z.-Z. Yu and D. Yang, *Adv. Funct. Mater.*, **n/a**, 2308845.

159 D. Oladimeji, K. Gupta, N. A. Kose, K. Gundogan, L. Ge and F. Liang, *Sensors*, 2023, **23**, 3880.

160 C. Zhang, Y. Liu, B. Zhang, O. Yang, W. Yuan, L. He, X. Wei, J. Wang and Z. L. Wang, *ACS Energy Lett.*, 2021, 1490–1499.

161 X. He, Y. Zi, H. Yu, S. L. Zhang, J. Wang, W. Ding, H. Zou, W. Zhang, C. Lu and Z. L. Wang, *Nano Energy*, 2017, **39**, 328–336.

162 L. He, C. Zhang, B. Zhang, O. Yang, W. Yuan, L. Zhou, Z. Zhao, Z. Wu, J. Wang and Z. L. Wang, *ACS Nano*, 2022, **16**, 6244–6254.

163 M.-H. Sigari, M. Fathy and M. Soryani, *Int. J. Veh. Technol.*, 2013, **2013**, 1–11.

164 X. Lu, L. Zheng, H. Zhang, W. Wang, Z. L. Wang and C. Sun, *Nano Energy*, 2020, **78**, 105359.

165 M. Divjak and H. Bischof, 2009, pp. 350–353.

166 W. Liu, X. Zhai, W. Wang, B. Zheng, Z. Zhang, X. Fan, J. Wang and Y. Chen, *J. Mol. Cell. Cardiol.*, 2019, **127**, 115.

167 B.-G. Paik, S.-R. Cho, B.-J. Park, D. Lee, B.-D. Bae and J.-H. Yun, *J. Mar. Sci. Technol.*, 2009, **14**, 115–126.

168 S. Wang, Y. Wang, D. Liu, Z. Zhang, W. Li, C. Liu, T. Du, X. Xiao, L. Song, H. Pang and M. Xu, *Sens. Actuators Phys.*, 2021, **317**, 112459.

169 C. Zhang, L. Zhou, P. Cheng, D. Liu, C. Zhang, X. Li, S. Li, J. Wang and Z. L. Wang, *Adv. Energy Mater.*, 2021, **11**, 2003616.

170 S. C. Elmendorf, G. H. R. Henry, R. D. Hollister, R. G. Björk, N. Boulanger-Lapointe, E. J. Cooper, J. H. C. Cornelissen, T. A. Day, E. Dorrepaal, T. G. Elumeeva, M. Gill, W. A. Gould, J. Harte, D. S. Hik, A. Hofgaard, D. R. Johnson, J. F. Johnstone, I. S. Jónsdóttir, J. C. Jorgenson, K. Klanderud, J. A. Klein, S. Koh, G. Kudo, M. Lara, E. Lévesque, B. Magnússon, J. L. May, J. A. Mercado-Dı´az, A. Michelsen, U. Molau, I. H. Myers-Smith, S. F. Oberbauer, V. G. Onipchenko, C. Rixen, N. Martin Schmidt, G. R. Shaver, M. J. Spasojevic, Þ. E. Þórhallsdóttir, A. Tolvanen, T. Troxler, C. E. Tweedie, S. Villareal, C.-H. Wahren, X. Walker, P. J. Webber, J. M. Welker and S. Wipf, *Nat. Clim. Change*, 2012, **2**, 453–457.

171 S. Fu, H. Wu, C. Shan, K. Li, W. He, Q. Li, X. Yu, S. Du, G. Li and C. Hu, *Nano Energy*, 2023, **116**, 108850.

172 M.-L. Seol, S.-B. Jeon, J.-W. Han and Y.-K. Choi, *Nano Energy*, 2017, **31**, 233–238.

173 K. Skalska, J. S. Miller and S. Ledakowicz, *Sci. Total Environ.*, 2010, **408**, 3976–3989.

174 D. Shindell and C. J. Smith, *Nature*, 2019, **573**, 408–411.

175 K. Han, J. Luo, Y. Feng, Q. Lai, Y. Bai, W. Tang and Z. L. Wang, *ACS Nano*, 2020, **14**, 2751–2759.

176 L. Soontha and M. Y. Bhat, *Sustain. Dev.*, , DOI:10.1002/sd.2764.

177 S. Fu, W. He, Q. Tang, Z. Wang, W. Liu, Q. Li, C. Shan, L. Long, C. Hu and H. Liu, *Adv. Mater.*, 2022, **34**, 2105882.

178 T. M. Lenton, *Nat. Clim. Change*, 2011, **1**, 201–209.

179 S. Sippel, N. Meinshausen, E. M. Fischer, E. Székely and R. Knutti, *Nat. Clim. Change*, 2020, **10**, 35–41.

180 D. Liu, C. Li, P. Chen, X. Zhao, W. Tang and Z. L. Wang, *Adv. Energy*

View Article Online
DOI: 10.1039/D4EE00482E

Mater., 2023, **13**, 2202691.

181 H. Zou, E. Gratz, D. Apelian and Y. Wang, *Green Chem.*, 2013, **15**, 1183–1191.

182 B. Huang, Z. Pan, X. Su and L. An, *J. Power Sources*, 2018, **399**, 274–286.

183 G. Harper, R. Sommerville, E. Kendrick, L. Driscoll, P. Slater, R. Stolkin, A. Walton, P. Christensen, O. Heidrich, S. Lambert, A. Abbott, K. Ryder, L. Gaines and P. Anderson, *Nature*, 2019, **575**, 75–86.

184 B. Zhang, L. He, J. Wang, Y. Liu, X. Xue, S. He, C. Zhang, Z. Zhao, L. Zhou, J. Wang and Z. L. Wang, *Energy Environ. Sci.*, 2023, **16**, 3873–3884.

185 T. Li, Y. Xiong, X. Yan, T. Hu, S. Jing, Z. Wang and X. Ge, *J. Energy Chem.*, 2022, **72**, 532–538.

186 B. Zhang, L. He, R. Zhang, W. Yuan, J. Wang, Y. Hu, Z. Zhao, L. Zhou, J. Wang and Z. L. Wang, *Adv. Energy Mater.*, 2023, **13**, 2301353.

187 D. Zwicker, R. Seyboldt, C. A. Weber, A. A. Hyman and F. Jülicher, *Nat. Phys.*, 2017, **13**, 408–413.

188 J. Sun, L. Zhang, S. Gong, J. Chen and H. Guo, *Adv. Mater.*, **n/a**, 2305578.

189 A. Erdemir, G. Ramirez, O. L. Eryilmaz, B. Narayanan, Y. Liao, G. Kamath and S. K. R. S. Sankaranarayanan, *Nature*, 2016, **536**, 67–71.

190 G. Wu, J. Yang, J. Shang and D. Fang, *Energy*, 2020, **195**, 116957.

191 J. Zhao, D. Wang, F. Zhang, J. Pan, P. Claesson, R. Larsson and Y. Shi, *Nano-Micro Lett.*, 2022, **14**, 160.

192 C. Chen, Z. Wen, A. Wei, X. Xie, N. Zhai, X. Wei, M. Peng, Y. Liu, X. Sun and J. T. W. Yeow, *Nano Energy*, 2019, **62**, 442–448.

193 K. Doufène, C. Tourné-Péteilh, P. Etienne and A. Aubert-Pouëssel, *Langmuir*, 2019, **35**, 12597–12612.

194 P. B. Dehkordi, L. P. M. Colombo, E. Mohammadian, D. Arnone, A. Azdarpour and G. Sotgia, *J. Pet. Sci. Eng.*, 2019, **178**, 1–13.

195 Z. Song, X. Zhang, Z. Wang, T. Ren, W. Long, T. Cheng and Z. L. Wang, *ACS Nano*, 2021, **15**, 18557–18565.

196 G. M. Whitesides, *Nature*, 2006, **442**, 368–373.

197 K. S. Elvira, X. C. i Solvas, R. C. R. Wootton and A. J. deMello, *Nat.*

View Article Online
DOI: 10.1039/D4EE00482E

Chem., 2013, **5**, 905–915.

198 J. Li, Y. Zheng, J. Qiu, W. Niu, J. Wu, H. Cui, Y. Zi and X. Li, *Nano Energy*, 2023, 109061.

199 C. Wang, X. Li, Y. Qiu, L. Wang, C. Li, G. Liu, G. Liu, Q. Zheng, X. Chen, H. Tian, C. Wang and J. Shao, *Nano Energy*, 2022, **98**, 107310.

200 L. Zhang, X. Li, Y. Zhang, Y. Feng, F. Zhou and D. Wang, *Nano Energy*, 2020, **78**, 105370.

201 H. Wu, W. He, C. Shan, Z. Wang, S. Fu, Q. Tang, H. Guo, Y. Du, W. Liu and C. Hu, *Adv. Mater.*, 2022, **34**, 2109918.

202 A. C. Wang, B. Zhang, C. Xu, H. Zou, Z. Lin and Z. L. Wang, *Adv. Funct. Mater.*, 2020, **30**, 1909384.

203 J. Jang, D. W. Kim, J. H. Lee, C. Choi, M. Go, J. K. Kim and U. Jeong, *Nano Energy*, 2022, **98**, 107320.

204 X. Ge, Z. Gao, L. Zhang, H. Ji, J. Yi, P. Jiang, Z. Li, L. Shen, X. Sun and Z. Wen, *Nano Energy*, 2023, **113**, 108541.

205 M. Kanik, M. Marcali, M. Yunusa, C. Elbuken and M. Bayindir, *Adv. Mater. Technol.*, 2016, **1**, 1600190.

206 A. A. Marino, I. G. Iliev, M. A. Schwalke, E. Gonzalez, K. C. Marler and C. A. Flanagan, *Tumor Biol.*, 2009, **15**, 82–89.

207 M. Kanik, M. G. Say, B. Daglar, A. F. Yavuz, M. H. Dolas, M. M. El-Ashry and M. Bayindir, *Adv. Mater.*, 2015, **27**, 2367–2376.

208 R. G. Johnson and R. E. Higashi, *Sens. Actuators*, 1987, **11**, 63–72.

209 J. Chen, H. Guo, J. Zheng, Y. Huang, G. Liu, C. Hu and Z. L. Wang, *ACS Nano*, 2016, **10**, 8104–8112.

210 X. Li, T. Tat and J. Chen, *Trends Chem.*, 2021, **3**, 765–778.

211 X. He, H. Zou, Z. Geng, X. Wang, W. Ding, F. Hu, Y. Zi, C. Xu, S. L. Zhang, H. Yu, M. Xu, W. Zhang, C. Lu and Z. L. Wang, *Adv. Funct. Mater.*, 2018, **28**, 1805540.

212 M. W. Tibbitt, J. E. Dahlman and R. Langer, *J. Am. Chem. Soc.*, 2016, **138**, 704–717.

213 J. Nie, Z. Ren, J. Shao, C. Deng, L. Xu, X. Chen, M. Li and Z. L. Wang, *ACS Nano*, 2018, **12**, 1491–1499.

214 H. Li, W. Fang, Y. Li, Q. Yang, M. Li, Q. Li, X.-Q. Feng and Y. Song, *Nat. Commun.*, 2019, **10**, 950.

215 Z. Liu, J. Nie, B. Miao, J. Li, Y. Cui, S. Wang, X. Zhang, G. Zhao, Y. Deng, Y. Wu, Z. Li, L. Li and Z. L. Wang, *Adv. Mater.*, 2019, **31**, 1807795.

216 T. Kotnik, W. Frey, M. Sack, S. Haberl Meglič, M. Peterka and D. Miklavčič, *Trends Biotechnol.*, 2015, **33**, 480–488.

217 J. Tian, H. Feng, L. Yan, M. Yu, H. Ouyang, H. Li, W. Jiang, Y. Jin, G. Zhu, Z. Li and Z. L. Wang, *Nano Energy*, 2017, **36**, 241–249.

218 Y. Chen, P. Wang, C. Wang, J. Li, M. Tan and M. Zhao, *Mater. Today Sustain.*, 2023, 100606.

219 W. Ding, J. Zhou, J. Cheng, Z. Wang, H. Guo, C. Wu, S. Xu, Z. Wu, X. Xie and Z. L. Wang, *Adv. Energy Mater.*, 2019, **9**, 1901320.

220 Z.-Y. Huo, D.-M. Lee, J.-M. Jeong, Y.-J. Kim, J. Kim, I.-Y. Suh, P. Xiong and S.-W. Kim, *Adv. Energy Mater.*, 2022, **12**, 2103680.

221 Y. Li, C. Liu, H. Zou, L. Che, P. Sun, J. Yan, W. Liu, Z. Xu, W. Yang, L. Dong, L. Zhao, X. Wang, G. Wang and Z. L. Wang, *Cell Rep. Phys. Sci.*, 2023, **4**, 101191.

222 H. Liu, J. Huang, J. Mao, Z. Chen, G. Chen and Y. Lai, *iScience*, 2019, **19**, 214–223.

223 L. Liao, W. Xiao, M. Zhao, X. Yu, H. Wang, Q. Wang, S. Chu and Y. Cui, *ACS Nano*, 2020, **14**, 6348–6356.

224 Y. Yang, Y. Yang, J. Huang, S. Li, Z. Meng, W. Cai and Y. Lai, *Adv. Fiber Mater.*, 2023, **5**, 1505–1518.

225 P. Jiao, Z. L. Wang and A. H. Alavi, *Adv. Mater.*, 2023, **n/a**, 2308505.